BIOLOGICAL MIXING AND CHAOS

by

BELINDA ABIGAIL AMANDA ORME

A thesis submitted to
The University of Birmingham
for the degree of
DOCTOR OF PHILOSOPHY

School of Mathematics and Statistics
The University of Birmingham

July, 2001.

Synopsis

We consider a problem from the field of biological fluid mechanics which considers the flow associated with the motion of a flagellum on a sessile micro-organism. Motivation is taken from the movement of fluid around a species of choanoflagellate, *Salpingoeca Amphoridium*. Choanoflagellates are a class of organism in the phylum Protozoa. Because the length scales and velocities are very low, the flow is one dominated by viscous forces and the environment is characterised by a low Reynolds number.

The flow caused by the flagellum is initially modelled via a point force. These micro-organisms operate in more than one location and the motion they create is modelled in a qualitative sense by using two stokeslets (appropriate to Stokes' flow) whose orientation and position is varied with time. The sessile micro-organism resides above a boundary which is modelled, most generally, as an interface between two fluids possessing different properties. Efficiency of feeding currents generated by the flagellum motion is studied. The resulting dynamics are investigated using chaotic measures, which examine the stretching and consequent mixing of elements within the fluid. Different point force locations lead to various eddy structures such that their superposition results in chaotic advection.

The model is developed to examine the flow of particles around a three-dimensional realisation of a micro-organism which involves a flagellum and a cell body attached to a substrate. Green's functions are used to satisfy a number of boundary conditions simultaneously. Particle paths of a tracer introduced into the fully three-dimensional model are investigated. Comparisons with experimental data illustrate good agreement between theoretical and experimental results. Further extensions to the model are suggested.

I dedicate this thesis to my family, friends and Martin,
all of whom have invested so much of their valuable
time, love and support in me.

Acknowledgements

I would like the give many thanks to my supervisors, Professor John Blake and Dr. Stephen Otto, for their encouragement, time, wisdom and a plentiful supply of patience. I am very grateful to Dr. Michala Pettitt for collaborating with me during the course of her Ph.D. and providing me with many explanations, references and ideas relating to the study of microbiology. I acknowledge the supply of photographic material and other experimental data which has been provided by Dr. Michala Pettitt and appears within this thesis.

My deepest gratitude goes to all of my family, friends and colleagues who have supported me throughout my Ph.D.. I acknowledge the support of the E.P.S.R.C. for their funding.

Contents

List of Figures

List of Tables

Chapter 1

INTRODUCTION

1.1 Setting the scene

Biological and physiological fluid dynamics is an interesting and vast area of research due to its huge diversity. Biological systems are abundant in the world around us, for example, from the large scale motion of mammals to the smallest internal structures of our circulatory system (see Lighthill (1976)).

Biological systems encompass far ranging mechanisms, from molecular biology to the mechanics of a system, but in this work we will largely be concerned with fluid flows and the interaction of a fluid with nearby boundaries. The characteristics of flows in biological systems occur in several different régimes. These régimes have at one extreme, slow viscous flows and at the other, high speed inertial flows. Viscosity dominated flows, the area of most interest in this thesis, are classified by small Reynolds numbers. The Reynolds number is defined as

$$Re = \rho \frac{UL}{\mu},$$

where U is a characteristic speed, μ is the dynamic viscosity, ρ is the density and L is a typical length scale. (All of the scales are taken as typical of the systems we are studying.) From this we see that a small Reynolds number would correspond to any combination of small length scales, slow flows or high viscosities (i.e. a very 'sticky' fluid). Typical Reynolds numbers in which we are interested are in the range 10^{-6} for bacteria in water

to 10^{-2} for spermatozoa in semen. At the other end of the scale inertial flows usually have a large Reynolds number. This is due to the longer length scales, greater speeds and smaller viscosity. Typical examples of two systems illustrating the differences are the flow of human blood in capillaries which is viscous flow and the air around a soaring bird in flight which is dominantly inertial flow. In either of these cases modelling the systems and developing solutions for the flow could require very different approaches. Both may use slender body theory in their solution but the fundamental fluid dynamics behind each system would be considerably different.

Much work has been previously covered by mathematicians and biologists in the study of low Reynolds number flows. Many of the cases examined are concerned with considering organisms whose habitat can be characterised as being on a small scale. Motility, feeding and transport within and around these flow domains present a variety of problems. In these type of environments, the fluid mechanics is naturally dominated by viscous flows. In this régime we can neglect the nonlinear convective terms in the Navier-Stokes equations. Hence the governing equations of these viscous flows are the Stokes' flow equations. The reversibility of inertial free systems is exploited by certain organisms who inhabit regions dominated by viscosity. For example, organisms can typically employ the use of features such as a flagellum with a helical beat which can overcome the reversibility of the fluid properties. By not restricting the flagellum to planar motion, a helical motion will ensure that the organism progresses through the fluid. Further details in Ramia, Tullock & Phan-Thien (1993) give a background on similar micro-organisms' locomotion by studying various hydrodynamic interactions of this type of movement. For a system with no inertia, we know that as soon as the force is removed from the particle, its motion will stop instantaneously. This creates a very difficult environment in which organisms need to encourage movement of particles.

The specific flow which motivates our study is in an inertial free régime. The low Reynolds number flow we investigate occurs in the locality of choanoflagellates. The latter part of the word -flagellate comes from the Greek and means 'to whip', indicating

the characteristics of the motion of the flagellum through the fluid. Choanoflagellida, or choanoflagellates, are a single celled organism of the phylum Choanozoa, Sleigh (1973) and Pettitt (2000). They account for a large proportion of the total consumption of bacteria from the environment they live in, such as canals in the case of freshwater choanoflagellates and oceans in the case of marine dwelling choanoflagellates. A typical marine choanoflagellate would be *Biscosta spinifera* found in the Weddell Sea, Antarctica (see Thomsen, Buck, Coale, Garrison & Gowing (1990)). The dimensions of the organisms we observe have length of flagellum approximately $15 - 30\mu$m and radius of flagellum approximately 0.4μm. Holwill (see Sleigh (1974) pp 145) provides a table which indicates the orders of magnitude for a number of flagella dimensions allowing one to calculate the typical Reynolds number. These choanoflagellates are useful organisms because of their ability to consume all types of particulate waste. They are also very easy to study which makes them an ideal organism on which to perform experiments allowing the collation of data concerning their feeding habits. We study both a simple axisymmetric model and then extend this to a more detailed three-dimensional description of the organism.

1.2 *Salpingoeca Amphoridium* (SA)

The choanoflagellate we will be studying is *Salpingoeca Amphoridium* (SA), shown in Figure 5.1 on page 104 as a magnified photograph along side a simplified sketch. SA is a genus of the order Choanoflagellida. This genus is one of the three main Choanoflagellida (the others being *Codosigidae* and *Acanthoecidae*). We note that SA is a sessile organism and so has a surface of attachment which we consider when modelling the flow patterns around it. An organism which has similar structure to SA is a spermatozoon. It possesses the same type of cell body and flagellum interaction but does not possess a collar, unlike SA. Spermatozoon is a motile organism which uses the force created from its flagellum to balance the drag of the cell body and so propel itself through the viscous environment within which it resides. In the case of SA, the force created due to the flagellum interacts

with the boundary leading to eddies which are seen either side of the cell body. These are studied in due course.

SA is a distinctive organism, due in particular to one of its features, a collar, which protrudes from its cell body. This collar, as we view it, is composed of many fine filaments (or micro-villi) which when photographed give the impression of a crown forming around the top of the cell body. The collar is visible in Figure 5.1 as two thin arms which emerge from the top of the cell and point towards the top right hand corner of the photograph. The collar is very important in the action of feeding because of its rôle as a filter for particles which come into contact with it through the movement of the surrounding fluid, Pettitt (2000). It is also thought to provide some means of moving the trapped particles towards the 'mouth' situated at the base of the collar on the cell body. The particle will then be engulfed by processes such as phagocytosis. The fluid is given motility due to the action of the flagellum which protrudes from the cell body and has its base situated in the centre of the collar. This flagellum approximately doubles the total height of SA if we take into consideration the stalk which is attached to the opposite side of the cell body. This stalk is used for attaching SA to a fixed surface and is thought to enable more feeding currents to be generated due to the close proximity of a solid boundary with the forces created by the flagellum. SA also possesses a lorica which surrounds the cell body. The lorica is seen in Figure 5.1 (a) and is the cup-like feature which the cell body rests within. Its purpose is not entirely known because there are certain choanoflagellates who function without it (Thomsen et al. (1990)). It is mostly developed as a protective 'case' for the cell body to reside within. SA can also be found directly attached to the substrate, i.e. it does not possess a stalk. The reason for this type of attachment is not known but the method we use to develop the model of SA will accommodate such a variation by simply altering the parameters of the model.

1.3 Patterns of fluid motion

The motion of the flagellum creates fluid patterns which are the structures that we are interested in during the course of the study. These resulting eddies can carry tracer particles along path lines and the evolution of their trajectories can be followed over time. We want to examine the patterns of filter feeding that can develop for various parameters of the problem, i.e. the type of eddies created for any organism. If a flagellum was to create motion of the fluid with no fixed boundary in close proximity, that is the organism was not a sessile but a motile organism, then we would observe particles which would move close by the body in a direction almost parallel to the direction of motion. In the case of SA, we have a sessile organism where the boundary has a great influence on the patterns of the particles traced out by the stream lines.

An important difference between motile and sessile organisms is related to the location of their food source. Motile organisms can seek out a food source, for example using concentration gradients, and then move to the appropriate location to optimise feeding. However, sessile organisms must create enough motion so that the fluid rich in nutrients moves within close proximity of its capture region. The eddies created by sessile organisms are mostly dependent on how the forces in the fluid act relative to any given boundaries. Interactions between the cell body and forces from the flagellum will also need to be accounted for because these too will affect the overall flow patterns.

Figures 1.1 illustrate the circulation of fluid which could occur around various micro-organisms. In Figure 1.1 (a) the recirculation motion will allow regions of fluid to repeatedly pass through the collar which would be situated within close proximity to the eddies. The stream lines for a motile organism are also shown in Figure 1.1 (b) in a similar figure to that which is presented in Fenchel (1986) and we can see the differences between these first two cases. In both examples, the stream lines will simply show the path of steady fluid flow driven by the forces in the problem. Figure 1.1 (c) shows a case we may study illustrating what happens to the fluid when two organisms are situated adjacent to each other. These figures are similar to those in Blake, Otto & Blake (1998). They show the

various regions of recirculation that can develop around an organism for a number of different force interactions. Notice here we are considering the force acting perpendicular to the substrate because it is pertinent to the biological situation we want to model.

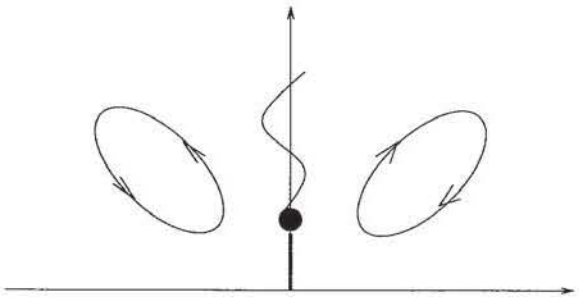

Fig. 1.1 (a) Eddies created by a sessile organism.

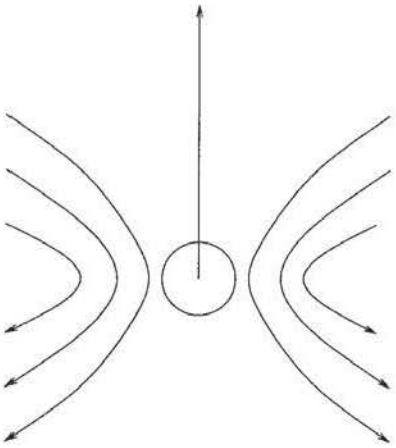

Fig. 1.1 (b) The flow around a spherical cell body representing a motile organism.

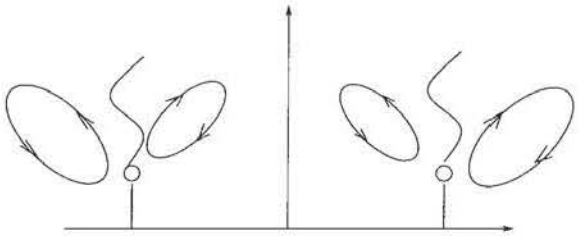

Fig. 1.1 (c) A schematic of eddies for two adjacent organisms.

Figure 1.1: Diagrams to illustrate the eddy patterns which can be created within the fluid due to point forces acting perpendicular to the boundary where appropriate.

1.4 Stirring and mixing

By stirring the fluid in the manner indicated in Figure 1.1 (a), SA is creating a perpetual flow of particles to pass through the collar rather than just waiting for motion of the fluid itself to enable particles to become trapped on the collar. However, this still does not create the most efficient manner of feeding for SA because as long as we are assuming no

diffusion and no alternative fluid motion, then after a certain length of time SA will have exhausted the food supply within its finite domain. This finite domain can be considered to be the area (or volume) over which the eddy can influence particles. We can assume there is no alternative fluid flow in the system because the flow is occurring at a low Reynolds number and hence, over a slow time scale this is very unlikely. This assumption is particularly valid for SA whose environment is stagnant, such as a canal. Also notice that molecular diffusion will be very weak here so that the organism's feeding cannot rely on diffusion to bring the particles to the region of capture. These are not the most ideal circumstances in which to feed and so instead SA and other similar organisms develop a method by which they can encourage more particles to move towards the collar. We later refer to bacteria as particles which are subject to Brownian motion, but in our initial model it is a weak effect which can be neglected.

Blake & Otto (1996) investigate filter feeding in two types of organism. They are particularly interested in *Vorticella* which due to its small length scales inhabits environments characterised by low Reynolds numbers. *Vorticella* is a sessile organism possessing a 'crown' of cilia on top of its cell body. The cell body is attached via a stalk to a solid surface. The cilia drive the motion of the fluid around the cell body by small undulating movements. This enables particles in the fluid to pass between the cilia for capture by the 'mouth' situated at the top of the cell body. It is proposed in Blake et al. (1998) that by altering the position of the cell body by a contraction or stretching of the stalk, *Vorticella* will alter the flow suitably to promote more mixing of particles within the fluid and improve the feeding current. The periodic contraction or stretching of the stalk is thought to enable *Vorticella* to capture particles from nearby the collar once they have been transported there by chaotic advection, rather than only reaching the organism along the continuous stream lines. These continuous stream lines would be the only way particles could reach the cell body of *Vorticella* in the usual steady Stokes' flow. The stream lines are mentioned below in relation to modelling SA in section 1.6.

We will discuss the movement of the point of application of the force that drives the

fluid. By moving the force we have an analogy with either movement of the flagellum or movement of the whole cell body. By creating this type of motion, the position of the eddy structures will be translated which allows regions of fluid which were previously undisturbed to now become more stirred. This new type of motion will also advect particles towards the cell from further away so that a greater region of fluid will become mixed. The greater degree of mixing increases the number of nutrient particles with which SA will come into contact. As a result, this increases its food supply. We note that we are assuming that SA has endless capacity for these nutrients. The experimental methods ensure the organisms studied are 'hungry' so that this assumption is valid over the duration of the experiment. Hence we assume a boundless number of particles can be removed from the region under the influence of the flagellum, plane and cell body interaction.

As well as the theory being applicable to flagellar motion, the pulsing that we are going to develop to represent the oscillating nature of the force will allow us to consider other pulsatile systems that may be similar to *Vorticella* discussed in Blake et al. (1998). The pulsing will be modelled by changing the location where the force of the flagellum acts. We will consider the force to act at a single specific point, although it still has direction. By considering different alignments of these point forces with respect to their boundaries, we can investigate the affect on fluid particles due to forces created by either the flagellum, an adjacent flagellum or the boundary.

1.5 Motion of particles around SA

Whilst developing the mathematical model to provide numerical results which allow the description of the fluid motion, there is also the opportunity to corroborate results with Pettitt (2000) who experimentally investigated the methods used by choanoflagellates (including SA) to feed. This work has been developed after work by Sleigh (1991) and is similar to studies undertaken by Higdon (1979*a*). Sleigh investigated the various clas-

sifications of types of flagellar beat and the patterns of fluid flow this created around the flagellum. The flow patterns created around collared flagella, such as SA, will be investigated using theoretical techniques originally developed by Higdon (1979*a*). Higdon's study models the forces created by a flagellum which generates the feeding currents around sessile organisms. The work however makes many simplifying assumptions, including neglecting the collar which is an important part of SA's filtering mechanism. We would like to augment his model, along with the initial model we introduce, by developing a method investigating the paths taken by various particles within the flow field. This would allow one to examine the efficiency of the feeding mechanism and look at the potential optimum dimensions of SA to create the best mixing régime.

Before we can specifically concentrate on the aspects of SA's features which we deem as most important to modelling the flow fields, it is necessary to understand more details of the physical system including the environment around SA (experimental or other). These organisms are distinctive in the manner with which they feed on bacteria because they catch particulate matter in a filter situated above their mouth region. Research has been previously undertaken by Rubenstein & Koehl (1977) and Fulford & Blake (1995) investigating filtering fluid through arrays of cylinders which could resemble the action of the collar. The cell feeds from the surrounding environment as the flagellum causes fluid to pass through the collar. The long flagellum is anchored to the top of the cell body and is on average one and a half times the length of the collar, dependent on the type of choanoflagellate studied. The stalk, whose presence is again dependent on the type of choanoflagellate, can be of varying degrees of rigidity. In this particular case it attaches SA to a rigid boundary. It would be equally valid to consider a freely moving (i.e. swimming) choanoflagellate as mentioned earlier in this section because it will only be the boundary conditions on the surface of the organism which change. For a more detailed description of SA see Pettitt (2000) and Chapter 4.

The methods used by SA to influence the flow around its body depend greatly on the beating of its flagellum. There has been much research into the motion of cilia and

flagella which will be useful in this study. The model we develop to describe the action of the organism initially concentrates on representing the influence of the flagellum as a single, unidirectional force. Later work will represent the flagellum shape with much greater accuracy than the initial simple model which provides a sound starting point for the investigation. The system which involves a flagellum mixing a fluid has received a great deal of investigation. This has been undertaken by biologists and mathematicians including Sleigh (1973), Lighthill (1976), Higdon (1979*a*), Fenchel (1986) and Fulford & Blake (1995), giving many models which we can exploit. These works also provide a number of experiments which have been carried out to confirm or disprove their findings. We can use these methods in validating our numerics although we mainly concentrate on confirmation of the results via experimental evidence from Pettitt (2000).

Flagella and cilia are similar in their external appearance, structure and shape, although they have differences in function. Following Sleigh (1973) it is reasonable to describe the cilia as a specialised class of flagella. The similarities between their methods of creating motion of fluid allows a larger range of theories to be considered when modelling a flagellum. One type of motion we can explore is helical motion in three dimensions which is commonly exhibited by flagella. Motion of the cilia can also occur in three dimensions when their movement is trying to restrict the amount of fluid that they actually propel in a recovery stroke for example. Rather than just creating the usual cilia 'whip' like motion within a plane, the recovery stroke may move off the plane so that it can move closer to the main body surface. Cilia usually occur in groups or 'fields', and provide movement of the surrounding fluid over and between their tips. Flagella, on the other hand, often appear individually (or possibly in pairs) and occur on the exterior of organisms to aid in their motility and feeding. It is this latter process of feeding we are most interested in, although methods to model the propulsion of an organism could follow similar lines. In particular, work by Higdon (1979*b*) investigates propulsion by a flagellum, and then proceeds to investigate propulsion by helical waves, Higdon (1979*c*). As an example of these entities in the mammalian body, one finds cilia which line the

lungs and create a constant movement of mucus. The mollusc (such as *mytilus edulis*). also uses rows of cilia (or cirri) as a method for particle movement and filter feeding, see Fulford & Blake (1995). In the second case, the cilia are arranged in 'combs', which aids the filtering process for the molluscs.

As mentioned above, the work within Higdon (1979 a, b, c) is concerned with flagellar motion, whether for sessile or motile organisms. Two types of wave forms can be used when modelling the flagellum, either a planar or helical beat, and both can be shown to be in agreement with nature where these two variations can be observed. For sessile organisms, the interactions found between the flagellum, the surface of the substrate and the cell body are taken into account. We choose to expand on the fundamental equations from Higdon (1979c) by applying the theory to SA such that the effect of the force of the flagellum on particles can be followed over time.

The extent to which work in Higdon (1979a) is followed is included in greater detail in Chapter 5. To set the initial model of a stokeslet (or stokeslets) and their various alignments in context, the next section will describe the logical progression from a simple to a more complex model of SA. The case of a single stokeslet or two horizontally displaced stokeslets gives an indication of the flow patterns one witnesses under experimental conditions. Further more, one can use the simple model to great advantage when investigating the degree of stirring or mixing within the region around the organism.

1.6 Modelling the fluid mechanics of the organism

It is appropriate to consider the biharmonic equation and its solutions when modelling this flow field. Some of the solutions are singular and it is these solutions which will give the building blocks for modelling the flagellum and the flow around it. Taking the fundamental singularities of the equation, we can develop the image system for solving the problem of a point force acting above an interface. Singularities, such as stokeslets, Stokes-doublets and dipoles, will create the mathematical Green's functions which allow

the latter work of this thesis to investigate the interaction of the boundaries and the forces within the model. A considerable amount of work was done by Blake (1971) who exploited the idea of an image system near a rigid boundary. To begin with, in this thesis we want to be able to model the flagellum as a single force. The initial method considers the force only acting at one point and having just one orientation. We can then determine the pressure and velocity which are caused by this force within the surrounding fluid. Consequently, we develop the consideration of stream functions which then allow one to follow particle paths within the fluid, see section 2.3. It is convenient if the flow is two dimensional in some sense, such as planar or axisymmetric, because we can then apply stream function techniques. One can gain verification to validate an axisymmetric study of the flow by investigating certain attracting features of the plane of the stokeslets, as pursued in Chapter 4. The stokeslet corresponds to a point force in an infinite medium and by using the idea of an image system we can then satisfy the physical constraints on both the rigid boundary or interface and far-field, Blake (1971) and Aderogba & Blake (1978*a*).

An important consideration is to change the point of application of the force due to the motion of the flagellum. As the flagellum beats we will find that there will be a shift in the region and direction associated with the dominant contribution to the force. This will have to be translated to a change in both the application point and the orientation of the force. The concept of a 'blinking' stokeslet was introduced in Blake & Otto (1996). They considered a periodic change in the position of application of a point force. By modelling the flagellum using a similar technique, its motion can be considered to be pulsatile in nature, see Blake & Otto (1996) and Blake et al. (1998) for further details.

Incorporating this pulsing nature of the beat leads to consideration of work by Aref & Balachandar (1986) who modelled stirring by looking at how particles are advected by an evolving velocity field. They examined the specific case of fluid mixing in the neighbourhood of two rotating infinite cylinders whose axes are not coincident (but parallel) and whose velocities are turned on and off in a prescribed manner. They specifically

introduce three types of time modulation for turning their stirring elements 'on' or 'off'. This modulation is dubbed a stirring protocol. The simplest modulation involves first one and then the other stirring mechanism alternating with each other in a discrete step-like manner. In the case of two cylinders rotating, whose motion would be smooth and continuous, it would not be strictly appropriate to apply a discrete stirring mechanism. However, in the instance of the pulsing force used within our model, a function which acts in a discrete manner (such as the delta function) is appropriate due to the nature of the system investigated. In the work which follows, the discrete pulse-like modulation we use will help to define a map.

We find (from the previous work of Blake & Otto (1996) and Blake et al. (1998)) that using two horizontally displaced stokeslets will provide a good basis from which to begin this study. It is a fairly simple process to then consider either case (horizontally or vertically displaced stokeslets) and to alter their orientation as mentioned above. Chapters 2 and 3 will consider both the horizontally and vertically displaced cases for completeness. We then choose to develop the ideas of chaotic mixing, here developed specifically for flagella, although there are a number of areas where we can apply these theories. The theory may be extended to other flows such as mucociliary transport, ovum transport and peristaltic motion within the gut, see Blake (2001) and Yannacopoulos, Otto & Blake (2001).

The simple representation of the action of the flagellum by point forces can be extended as in Higdon (1979*a*) to give a more accurate description of the flagellum shape and motion. Instead of a single force, a distribution of forces along a helical curve defining the flagellum shape creates a more realistic flow field to study. Similarly, the way these forces interact with the cell body and substrate is of major significance to the organism. Therefore, a particle within this flow field will experience a variation in its velocity at different stages of the flagellar beat. This is in contrast to the simple force field that a particle could feel with only one or two forces acting (for example single stokeslets) who do not change their direction.

In Chapter 4, we address the transition needed to move from a simple representation of the flagellum by a single point force to a distribution of many forces along a realistic flagellum. We refer to the study of Pettitt, Orme, Leadbeater & Blake (2001) where the flow field created due to a line distribution of forces is presented. This configuration illustrates an intermediate stage in the model because the force acts over an elongated region as one would expect of the true flagellum beat. Although it is still not the realistic curved flagellum, it will allow further insight into the flow fields expected from varying the parameters of the model.

The method used to determine how to distribute forces along the flagellum presents significantly more difficulty than with the single point force representation. Another investigation by Johnson (1980) can provide confirmation of the results we present in Chapter 5. The study by Johnson (1980) estimates the forces which have been created by a beating flagellum using methods due to Gray & Hancock (1955) and Lighthill (1976). These force estimations are derived from detailed work investigating resistance coefficients (which are discussed in greater detail in Appendix C). The work in the latter part of this thesis uses a rotating coordinate system to model the organism in three dimensions. This type of coordinate representation will be most appropriate when symmetrical shapes such as a spherical cell body can be rotated with ease. We investigate a model developed from the method contained in Higdon (1979*a*) and which involves both a fixed coordinate system with respect to the plane and a rotating coordinate system with respect to the flagellum.

As well as using stream functions, we also need to investigate methods to illustrate a representation of the fluid as time evolves. We have referred to the degree of mixing within the fluid and so we would like to investigate measures to describe the amount of change to the initial conditions of the system. This allows one to develop chaotic and statistical measures to research this specific biological flow in a quantitative manner.

1.7 Chaotic measures

We use the chaotic measures of Poincaré sections, the Hénon index and Lyapunov exponents to give us insight into how the tracer particles will behave over the long term. They give a mathematical perspective of the amount of particle dispersion we will observe. We present a more detailed summary below for each of these measures. By introducing stochastic measures, we will have some insight into the spreading of particles within a region of fluid. All of the above mentioned measures are important as far as mixing is concerned and they allow one to study the initial development of chaotic advection in the flow. In a filter feeding environment the generation of a well mixed fluid is imperative for the organisms' survival. The process of molecular diffusion is often important in fluid where particles mix, but we assume it to be relatively weak in this case. This assumption can be made because the time scale for diffusion is slower than the time scale of the system and further details can be found in Otto, Yannacopoulos & Blake (2001).

Many of the chaotic measures we are using were discussed in work by Hénon (1969). The measures allowed investigation of area preserving maps and gave an indication of when chaos appears in the system. We use Poincaré sections to visualise the long term action of particles, see section 3.1. They can give us information about the system we are studying, especially when we need to consider a wide range of parameter variation. They give a method which will allow one to create a simulation to follow the path of a particle.

We generate Poincaré sections by integrating a set of particles forward in time and recording their position after each pulse of the stokeslet. The position which these particles are situated at on a Poincaré section correspond to a path line for that particle. Steady flow will show this path line as a stream line, giving a level curve of the stream function. This is called an integrable dynamic system. For unsteady flow this path line depends on the initial position of the particle. Hence, the Poincaré section shows integrability by placing images of the particle on a smooth curve over time. If we see individual dots on the Poincaré section as opposed to continuous curves then we are able to obtain information relating to the periodicity of the system. For example, if we observe only

two dots or points on the section (after a repeated number of applications of the map) then we are observing an orbit of period two in terms of the switching protocol. This is illustrated in Figure 1.2 and shows how the Poincaré section samples the point in the same position every other period of the map. This definition can obviously be extended to any other number of periods as Figure 2.4 on page 35 illustrates. A point of period one is called a fixed point because it returns to the same position every time it passes through the Poincaré section, usually denoted by Σ. For non-integrability, the Poincaré section smears the images of the particle over a region rather than along a single continuous line. Poincaré sections are a good tool to use when considering the stirring of fluid and the long time behaviour of individual tracer particles. However, it is also instructive to look at stirred patches or areas of fluid. This allows one to introduce measures of dispersion such as the variance and covariance of a 'blob' of particles within the fluid.

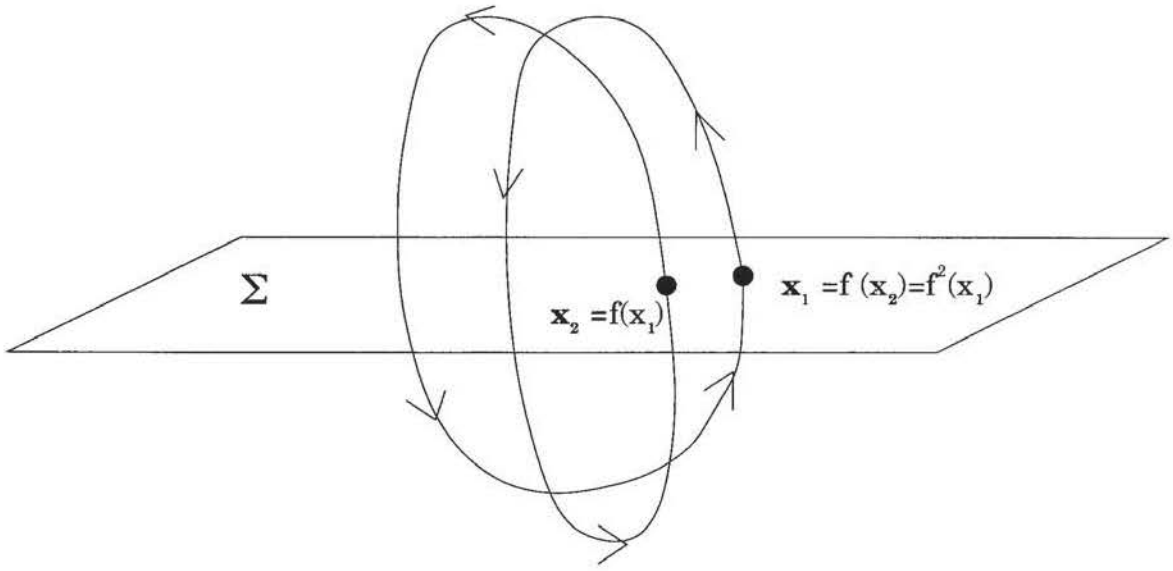

Figure 1.2: An example illustrating a representation of a period two map on a Poincaré section.

Lyapunov exponents are used to determine the stretching properties of a flow as considered previously in Otto et al. (2001), see section 3.2. Whereas the Poincaré sections describe a picture as time evolves, a diagram to illustrate the Lyapunov exponents will give a feeling of the stretching one can observe from a wider region. The stretching may be large after a certain length of time which would indicate a significant amount of mixing

within that region of the system and be characterised by a large Lyapunov exponent. If the exponent is small, the flow in that region shows little divergence from the initial conditions. However, to reach a limit allowing one to determine this measure would require a prohibitively large number of iterations of the map which is often not realistic in physical systems. We ideally want the system to reach a well mixed state within a small number of periods of the system. This is because the physical system will only have a finite time over which to perform mixing.

The Hénon index provides information on the bifurcation of the system for area-preserving maps, see section 3.3. An area-preserving map will be used throughout the following work after the initial map has been introduced in section 2.3. The bifurcation of the system is an important measure because ideally we are interested in determining the types of flow which will create the best mixing. If we have information on when the flow becomes more unstable then we are able to consider how particles will be affected. Along with the other chaotic measures, this gives great insight into the characteristics of the flow.

Examining the dispersion of particles over a certain period in time is the reason behind considering stochastic processes in section 3.4. These measures allow one to consider the 'effective diffusivity' within the system. Although we are assuming the system to have no diffusion due to Brownian motion, the chaotic measures allow consideration of the amount of effective diffusion which could be created by the organism. We obtain a measure for this degree of effective diffusion which can either be equal to, greater than or less than one. The latter two cases are termed superdiffusion and subdiffusion, where the mixing has respectively created a diffusion level above or below that which one would normally expect.

1.8 A three-dimensional model

Our initial approach to the problem concerning the flow fields around SA involves considering the simplified two stokeslet model of the system (as presented in Chapter 2) and analysing the outcomes of the numerical simulation of the flow using various techniques (Chapter 3). The analysis of flow fields is based on visualising the effect the flagellum has on a notional element of fluid over a certain period of time. These techniques convert easily to numerical schemes which provide a method of interpreting the resulting flow. The results for this simplistic model give insight but no specific details about the physical system we would like to study. Therefore, by developing a fully three-dimensional model incorporating some of the physical features of SA, we will progress towards beginning to understand the flow fields around SA.

We validate the axisymmetric case by investigating the attracting and repelling properties of a plane within space, presented in section 4.2. From this sound mathematical basis, one can progress to a more detailed study of a simplistic yet proper representation of a micro-organism. Consideration of the physical structure of the organism studied in Pettitt (2000) allows three-dimensional flow fields to be developed, see section 4.3. We closely follow work from Higdon (1979*a*) who provides a structure to determine the forces created by a flagellum beating in the presence of a sphere and a plane. Although the model still makes assumptions about a number of features of the organism, the inclusion of the most important three-dimensional features alone will greatly enhance the progression of the model. It will allow the paths taken by tracer particles to interact with the fluid, flagellum, plane and sphere simultaneously. Previously, the only effects on a particle and the surrounding viscous fluid requiring consideration were those of the individual point force and infinite plane. The effects of this new model will introduce a number of forces and boundaries into the problem resulting in the complex flow fields being modelled more accurately.

The introduction of Green's functions in Chapter 5 allows many forces acting in three dimensions to represent the flagellum, cell body and plane, and hence create a motion

of particles within the fluid. This interaction between forces will affect how the particles are advected with time because as the beat progresses, a different direction of motion will be evoked dependent on the particles' positions. The beat patterns which have been used previously in work by Higdon (1979*a*), Johnson (1980) and Ramia et al. (1993) vary from a planar to a helical beat and were motivated both by organism motility and feeding patterns. One way to approach such a study involves a rotating coordinate frame, an obvious choice for a system associated with a helical beat pattern. As predicted from results in Blake & Otto (1996) and Blake et al. (1998), different regions around these type of organisms generate various flow fields or particle paths. We will present trajectories of paths for a number of tracers enabling a catalogue of particle motions from different regions of the flow field to be built up.

The results will be comparable with experimental results because the assumptions we choose to make in the model resemble many important physiological features. Figure 5.3 on page 109 shows the typical model we choose which will represent an organism in three dimensions. Recordings made in experiments (from the study of Pettitt (2000)) will be used to allow the comparison of numerically generated particle paths with video images of paths taken by polystyrene microspheres over comparable time scales. The experimental results presented in Pettitt (2000) are believed to replicate the paths taken in the flow by nutrient particles on which these organisms would feed.

1.9 The structure of the thesis

Before the main component of the thesis, the structure is briefly presented.

The two-dimensional study associated with a 'blinking' stokeslet will examine both the vertically and the horizontally displaced cases because it highlights the differences we see in these two alternative types of flow generation. It will also provide a good comparison between previous studies and the work which is to follow. This is presented in the second and third chapters. Within both these chapters we further develop the work of Otto et

al. (2001) by considering the displacement and interaction of two stokeslets. Initially this work is confined to two dimensions where we consider the flows due to each stokeslet to be axisymmetric. The formulation of the work investigating two stokeslets is contained within section 2.2. We examine the mixing effects on an element of fluid within the flow using several stochastic techniques and elements from the theory of chaos to confirm our results. The methods we use give measures for the amount of mixing which has occurred in the system and are described in further detail in Chapter 3. The work within Chapters 2 and 3 is presented in Orme, Otto & Blake (2001*b*) (and certain elements are also published in Orme, Otto & Blake (2001*a*)).

In Chapter 4, the three-dimensional flow around a simple blinking stokeslet model is approached by considering the contours of stream lines around various configurations of stokeslets. The chapter summarises biological details of SA in relation to work undertaken by Pettitt (2000). We investigate particle paths around a typical organism looking at various parameters to alter a number of aspects of the model. Once a greater understanding of the structure of the system is developed, we proceed onto the final three-dimensional study.

Chapter 5 is the culmination of this thesis and presents a fully three-dimensional model of SA. Results which are developed via the use of a rotating reference frame show numerically generated particle paths contrasted with experimental results, Orme, Otto & Blake (2001*c*). Finally, Chapter 6 presents conclusions of the work presented throughout this thesis and indications of any further development which could follow.

Chapter 2

MATHEMATICAL FORMULATION OF THE AXISYMMETRIC MODEL

This chapter will construct the axisymmetric model with which we can begin to investigate the nature of the flow patterns around SA. We consider justification of all the assumptions concerning the equations we utilise. Then, the use of these equations to construct a map allowing the investigation of fluid flows is presented.

2.1 Introduction

In biological fluids one more than often considers very slow flows on small length scales where the fluids may also have a high viscosity (e.g. mucus). All of these factors contribute to making the Reynolds number small and allow the Stokes flow equations to be applied. This indicates to us that the dominant behaviour of the flow exhibits no inertia and we can class this as Stokes flow. We will propose a model to investigate the flow patterns created by a cilia or flagellum under these conditions. We regard the flagellum as a point force acting in the Stokes flow régime. By the use of image systems, as proposed by Blake (1971), we can use stokeslets to model the point force near a boundary so that the no-slip boundary condition is satisfied exactly.

We will investigate how a tracer behaves near the interface between two immiscible fluids. For convenience we consider two semi-infinite fluids where one is situated above an-

other. The interface represents the boundary between the fluids which each have different physical properties (density and viscosity) and may have a surface tension acting between them. The interface between the two fluids is assumed to be flat due to the action of surface tension and gravity although a real interface between two fluids will be anisotropic. The assumption is made that the interface is not surface active, so we characterise the interface by having a constant surface tension. We also assume by this definition that there is no continuous variation occurring at the interface which would normally occur on a molecular level. This assumption creates a discrete jump between the two fluids. The properties of the fluids such as density, ρ, viscosity, μ, and temperature, T, will vary dependent on the fluid. By simplifying the interface in this manner we have not made too much of a gross over approximation. However, we note this artificially sharp interface between the two fluids is not very physically realistic (e.g. a mucus interface) because there will usually be a region of variable properties which our interface does not permit.

We will position the stokeslets in the fluid either above or below the interface and initially take the stokeslets to be horizontally displaced. For our purposes the stokeslets are situated in the lower fluid, below the interface, as in Aderogba & Blake (1978*a*), during the axisymmetric case. Due to the viscous shear acting at the interface the effect of the stokeslets can be felt in both the upper and lower regions of the fluid. We can then look at how passive tracers in either of these regions behave over a certain length of time with varying strengths of stokeslet force. Although horizontally displaced stokeslets are considered here, we note that it takes a trivial manipulation to allow us to consider vertically displaced stokeslets instead. Figure 2.1 illustrates the spatial difference between these two configurations. The case of vertical displacement is considered in Blake & Otto (1996), Blake et al. (1998) and Otto et al. (2001). Note all these papers considered the two-dimensional case rather than the axisymmetric one. It is possible to consider the axisymmetric case for two vertically displaced stokeslets using an approach similar to that contained in the following work. Later sections within the context of the axisymmetric study will show results for both the vertical and the horizontal displacement cases. When

we are examining the three-dimensional case in Chapter 4 to provide justification of the work in this chapter, only horizontally displaced stokeslets are considered.

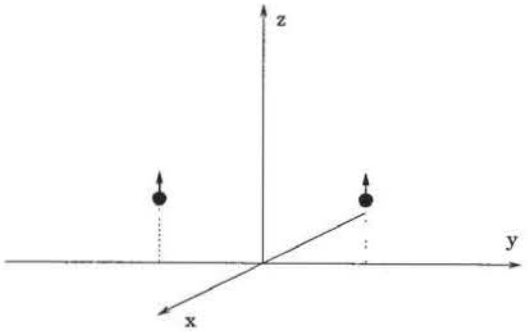

Fig. 2.1 (a) Horizontally displaced stokeslets.

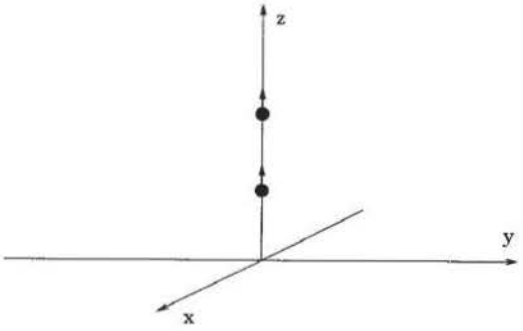

Fig. 2.1 (b) Vertically displaced stokeslets.

Figure 2.1: An illustration to show how stokeslets can either be considered as horizontally or vertically displaced.

2.2 The mathematical formulation

2.2.1 Stokes flow equations

The stokeslet is described by a velocity and pressure field associated with a point force. If this point force was to act at the point $\mathbf{y}$, then the solution to the equations

$$\nabla p = \mu \nabla^2 \mathbf{u} + \mathbf{F}\delta(\mathbf{x} - \mathbf{y}),$$

$$\nabla . \mathbf{u} = 0,$$

yields the pressure, p, and the velocity, $\mathbf{u}$, which give the fundamental singularity of the Stokes flow equations known as the stokeslet. We define the other constituents of the equation as: $\delta(\mathbf{x} - \mathbf{y})$ is the delta function indicating in this case that the force, $\mathbf{F}$, only acts at the point $\mathbf{x} = \mathbf{y}$. The viscosity of the fluid is defined by μ and will allow one to examine the limiting cases previously mentioned and again referred to in greater detail later within this section. We use the steady Stokes flow equations because we

are interested in a point force acting for an infinitesimal period of time. The solution obtained, for example via the method of three-dimensional Fourier transforms or other techniques, is

$$u_i = \frac{F_j}{8\pi\mu}\left(\frac{\delta_{ij}}{|\mathbf{x}|} + \frac{x_i x_j}{|\mathbf{x}|^3}\right) \quad \text{and} \quad p = \frac{F_i x_i}{4\pi|\mathbf{x}|^3},$$

in the case where $\mathbf{y} = \mathbf{0}$. For further details of deriving this result the reader is referred to Blake (1971) and Appendix A. The flow created by each vertically orientated stokeslet is an axisymmetric flow field in this case. This particular solution could correspond to the case of a motile flagellum and does not include a boundary to restrict the flow. Although the flow created by each stokeslet is an axisymmetric flow field, this does not imply that if we have two stokeslets acting together their combined flow field will also be axisymmetric. This will be investigated in more detail later in this chapter.

Figure 2.2 shows two stokeslets horizontally displaced with their position vectors given in cartesian coordinates as

$$S_1 : \mathbf{r}' = (x', y', -h) \quad \text{and} \quad S_2 : \mathbf{r}'' = (x'', y'', -h).$$

The positions of the stokeslets are usually given by $x' = x'' = 0$ and $y' = -y'' = a$, where a is an arbitrary constant, so that the stokeslets lie in the $y-z$ plane equidistance from the z-axis. They are illustrated according to this configuration in Figure 2.2. This positioning is important because we can now consider the particle moving about in a two-dimensional plane corresponding to the $y-z$ plane. Therefore the use of stream functions to examine the flow is a valid method. The two-dimensional section is not a slice of the more complicated three-dimensional motion, as it seems to suggest, but is motion confined to the plane. Therefore, because we are initially going to consider two stokeslets who are within a plane, a particle beginning its motion in the plane will also have its path restricted to this plane, i.e. there will be no azimuthal component to consider. This allows us to trace the particle path within a two-dimensional plane where we know that

we can apply a stream function to follow a particle. However, any displacement off this plane will lead to a fully three-dimensional motion which we discuss in greater detail in Chapter 4.

The orientation of the stokeslets is important in this axisymmetric, horizontally displaced case. We are looking at stokeslets that act perpendicular to the interface so that the method we outline below is applicable. Single stokeslets orientated parallel to the interface would not provide an axisymmetric flow and so considering a plane section would not be a valid method to use in that case. Instead, by looking at two perpendicular forces to the interface the particle will not be influenced to move off the plane. The remainder of this chapter examines a reduction of the three-dimensional space where we always consider the x-coordinate to be zero, as illustrated in Figure 2.2 where both stokeslets lie in the $y-z$ plane.

2.2.2 Stream functions

The flow can be described by stream functions which will differ depending on whether we are looking at the flow in the upper or lower half space. We will use cylindrical coordinates to describe the system where we take the generator of the cylinder to be a vertical line perpendicular to the interface and through the position of each stokeslet. Figure 2.2 illustrates the coordinate systems used. We naturally have different coordinates to describe the position of the tracer dependent on which stokeslet we are considering. The coordinates are given by (r, z, ϕ) where r is the radial distance from the generator of the stokeslet to the tracer, z gives the vertical distance between the tracer and the surface, and ϕ shows the angular direction the tracer lies in with respect to the stokeslet. We take ϕ to be zero in the direction of the positive x-axis. Using the subscripts 1 and 2 we prefer to use two coordinate systems to describe a particle's motion because as the stokeslets pulse alternately their periods of operation will be distinct and within each frame there will be no azimuthal movement. By combining the tracer positions after each stokeslet acts we can obtain an overall description of the flow with respect to any origin we choose.

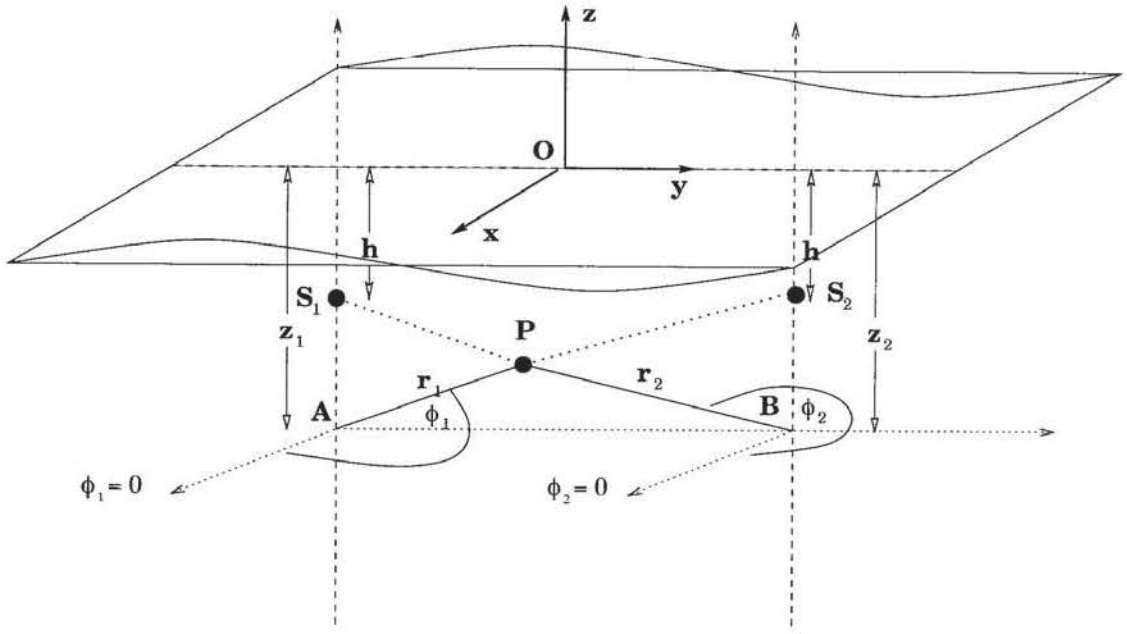

Figure 2.2: The cylindrical coordinate systems showing the position of the stokeslets relative to an arbitrary tracer which is positioned in the same half plane as the stokeslets; in general $z_1 = z_2$. We show here the orientation we will use when the horizontally displaced stokeslets are situated in the lower half plane. The stokeslets lie in the plane $x = 0$ whilst the mean position of the fluid interface is the plane $z = 0$. $\mathbf{r_1}$ and $\mathbf{r_2}$ are vectors in a parallel plane to the $x - y$ plane and containing the particle $\mathbf{P}$. Hence $|\mathbf{S_iP}|^2 = |\mathbf{r_i}|^2 + (z_i - h)^2$, for $i = 1, 2$.

It should be noticed the coordinate system is an axisymmetric system and the initial work considers $\phi_1$and ϕ_2 equal to either $\pi/2$ or $-\pi/2$, i.e. particle motion within the plane.

Following the work by Aderogba & Blake (1978*a*) we can look at the force of a stokeslet as acting either parallel or normal to the immiscible interface. We will consider a force acting normal to the interface as this will be pertinent to the biological situations we describe later in Chapter 4. Although in this case we consider the normal force, parallel forces to the interface also occur in biological fluids and can be useful when studying, for example, the lungs where sheets of cilia act together or in a metachronal wave to move mucus and debris out of the lungs. Examples of other such flows can also be found in the stomach or circulatory system. As previously stated we note that the case of the stokeslets acting parallel to the interface is not an axisymmetric problem. However, it can still be treated in a similar manner to the problem we are addressing. In that case, instead of working with stream functions we would choose to use velocity components.

Initially, the case of the normal force considered by Aderogba & Blake (1978*a*) was ill-posed. This is because one needed to consider a force balance at the interface which could not be suitably attained using surface tension alone. This was resolved when Aderogba & Blake (1978*b*) introduced a density difference between the two fluids which meant that an approximation (to first order) of the interface shape could be derived for forces normal to the interface. The general force balance used, where F describes the strength of the force acting vertically upwards, was

$$F = 2\pi(\rho_1 - \rho_2)g \int_0^\infty r\tau \, \mathrm{d}r,$$

where ρ_1 and ρ_2 are the fluid densities in the lower and upper fluid respectively, g is the gravitational acceleration and τ is the interface shape given by

$$\tau(r) = \frac{3h^3F}{2\pi(\rho_1 - \rho_2)g}(r^2 + h^2)^{-\frac{5}{2}},$$

for the particular case of no surface tension which we use in this problem.

The stream functions we use, given in Aderogba & Blake (1978*b*), are: for $z < 0$

$$\psi = \frac{F}{8\pi\mu_1}\left[\frac{r^2}{(r^2 + (z+h)^2)^{\frac{1}{2}}} - \frac{r^2}{(r^2 + (z-h)^2)^{\frac{1}{2}}} + \left(\frac{2\theta}{1+\theta}\right)\frac{hr^2z}{(r^2 + (z-h)^2)^{\frac{3}{2}}}\right],$$

and for $z > 0$

$$\psi = \frac{F}{8\pi\mu_1}\left(\frac{2}{1+\theta}\right)\frac{hr^2z}{(r^2 + (z+h)^2)^{\frac{3}{2}}},$$

where $\theta = \mu_2/\mu_1$. The other variables are defined as: μ_1 is the viscosity in the lower fluid, μ_2 is the viscosity in the upper fluid and h is the distance the stokeslets are situated below the interface. The coordinates (r, z) are the usual polar coordinates that we previously defined and illustrated in Figure 2.2. Later within this chapter these stream functions will be revisited once a coordinate transformation has been applied.

Notice that varying the value of θ will give several limiting cases which can be considered. We are mostly concerned with $z < 0$, i.e. the region in which the flagellum is taken to be located. The results we present within the next chapter will reflect this. For $\theta \to \infty$, i.e. $\mu_2/\mu_1 \to \infty$, we obtain the case where the immiscible surface is effectively a rigid no-slip wall. An example of this case could occur in the lungs where we have fluid lying over a layer of mucus (the physical representation would be an inverted case of our model with the mucus representing the rigid boundary). For $\theta \to 0$, i.e $\mu_2/\mu_1 \to 0$, we have $\mu_1 \gg \mu_2$ so that the surface above acts like a free surface. This would be comparable to the case where we had mucus underlying the air above, such as at a diffusive surface in any transport system. As noted in Aderogba & Blake (1978*a*), the case of $\theta = 1$ will not reproduce the case of an infinite fluid. This is because we need to consider the distribution of normal stresses over the interface at $z = 0$ which must satisfy the requirement that the normal velocity is zero. The type of physical situation this may represent could be the case of a nearly uniform fluid with some variation within it such as a salinity gradient found in sea water. The varying concentrations would then form the interface in that specific situation.

In Aderogba & Blake (1978*b*), as in this case, the positioning of the stokeslets in the lower half plane gave distinct tracer patterns to the fluid dependent on whether we observe the lower or upper region. In the region without the stokeslets the tracer showed no closed eddy patterns, but in the region containing the stokeslets Aderogba & Blake (1978*b*) showed there are closed stream lines for values of $0 < \theta$, where they neglect to consider the case $\theta = 1$. Again, this is because although it is possible to obtain numerical results for this case, it is not physically representative of any system that we are considering.

Figure 2.3 shows different patterns of the stream functions for both the upper and lower half planes with varying values of θ. Note the graphs plot the value of one stream function only. Also notice that when we increase the values of θ, the region $z > 0$ shows very little detail due to the density of the plotting function. This region becomes mostly

uniform now, which can be seen by referring to Figures 2.3 (e) and (f). We have kept $\alpha = 1$, where α gives the force of the stokeslet, for ease of comparison between the figures. The value of α we use is not important here as it will merely increase the height of the stream lines whilst illustrating the same structures. When θ is small, the surface between the two fluids acts like a free surface. From Figure 2.3 (c) we see that the region $z < 0$ (where the stokeslets are situated) has closed stream lines and the region above the free surface does not show these. A similar pattern could also be seen in Figure 2.3 (b) if the range of the axes was extended to incorporate the closed stream lines. As we increase θ further, the shape of the stream lines in the region $z < 0$ changes. The stream functions in the positive region will retain a similar pattern and it is only the value of the stream function which visibly alters. Finally, when θ is large, Figure 2.3 (f), we see that there is little difference in the stream lines above $z = 0$ and the interface is treated as though it were a rigid boundary. The maximum values of the stream function are given in the caption of Figure 2.3 to indicate the maximum velocities generated in each case for the region $z < 0$.

2.2.3 Blinking stokeslets

The method of working with blinking stokeslets is now incorporated into the study as detailed in Chapter 1. We will consider only one type of temporal variation where the time each stokeslet is active for is equally divided. We know that the radial and the vertical velocity of the tracer can now be expressed in terms of stream functions, the stream function used being naturally dependent on the region of fluid the tracer is situated in. The velocities in the horizontal and vertical directions are given as

$$u_r = \frac{1}{r}\frac{\partial \psi}{\partial z} \quad \text{and} \quad u_z = -\frac{1}{r}\frac{\partial \psi}{\partial r}.$$

To determine the position of the tracer when it has been acted on by two blinking stokeslets we first need to find the position of the tracer relative to the first stokeslet. By

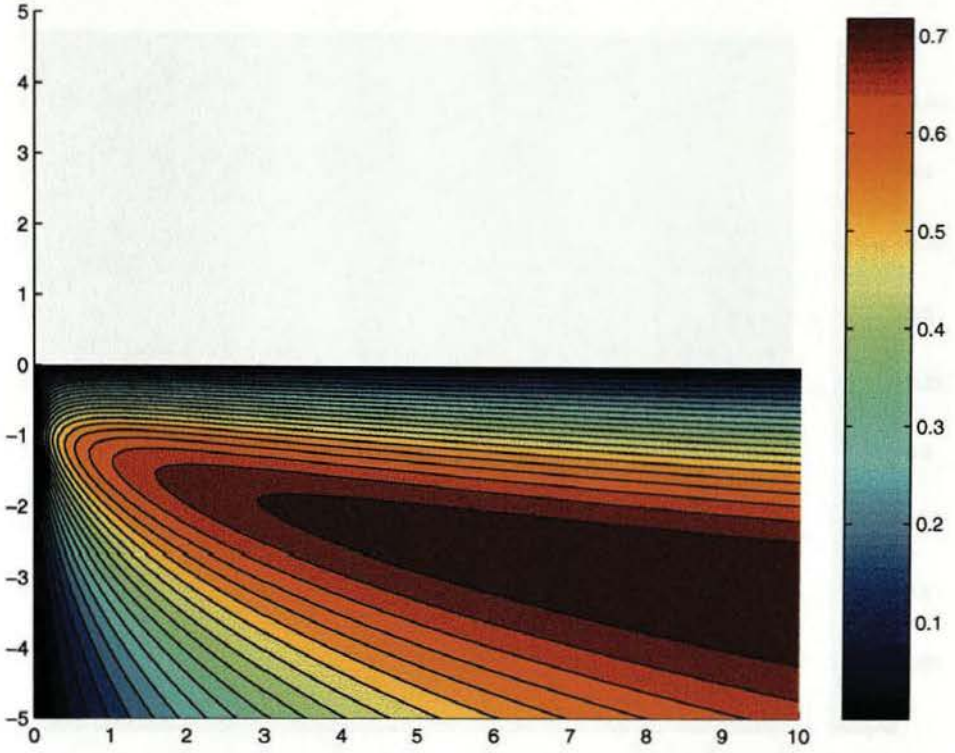

Fig. 2.3 (a) $\theta = 0$; $\max(\psi) = 0.7533$. This case is equivalent to a free surface at the line $z = 0$, hence the blank area in the figure.

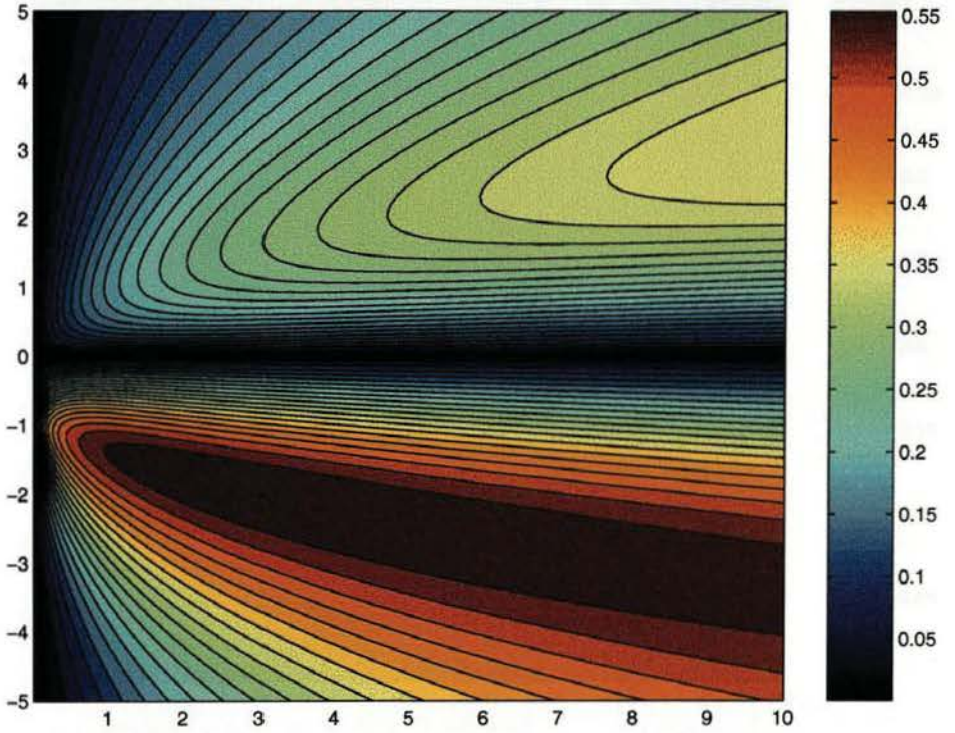

Fig. 2.3 (b) $\theta = 0.5$; $\max(\psi) = 0.3970$; fixed point (3.01,-2.01).

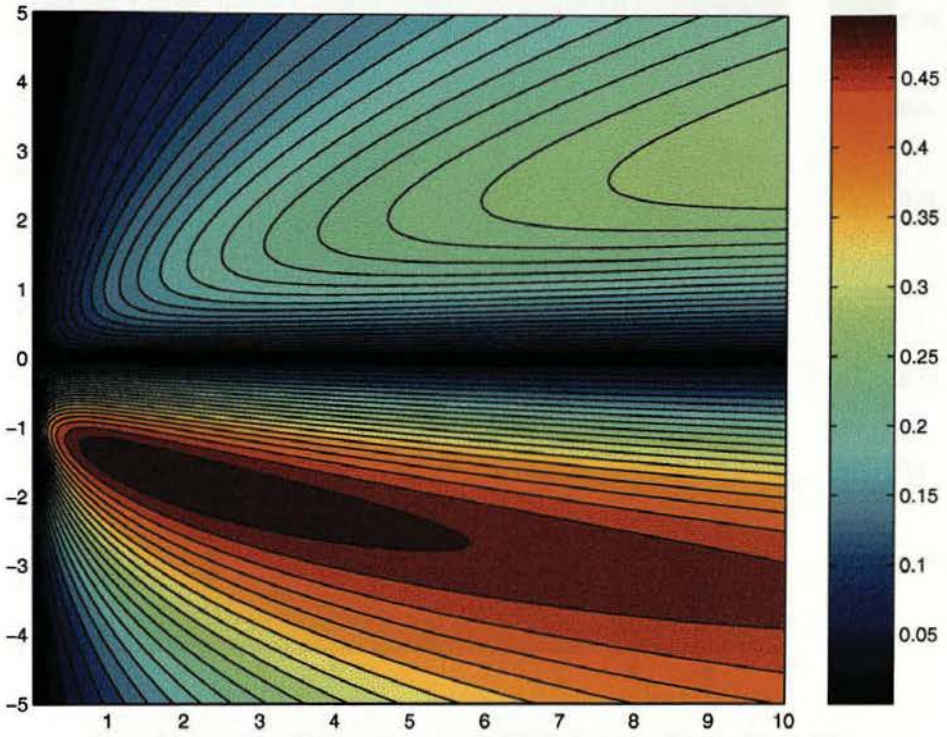

Fig. 2.3 (c) $\theta = 1$; $\max(\psi) = 0.5192$; fixed point (1.61,-1.61).

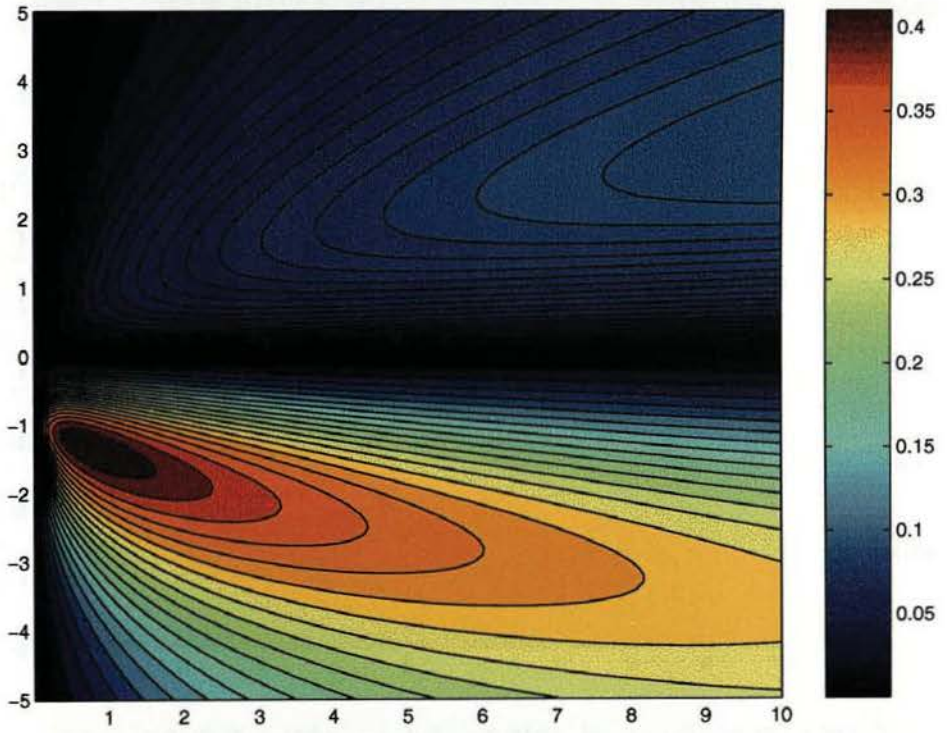

Fig. 2.3 (d) $\theta = 5$; $\max(\psi) = 0.4304$; fixed point (0.71,-1.31).

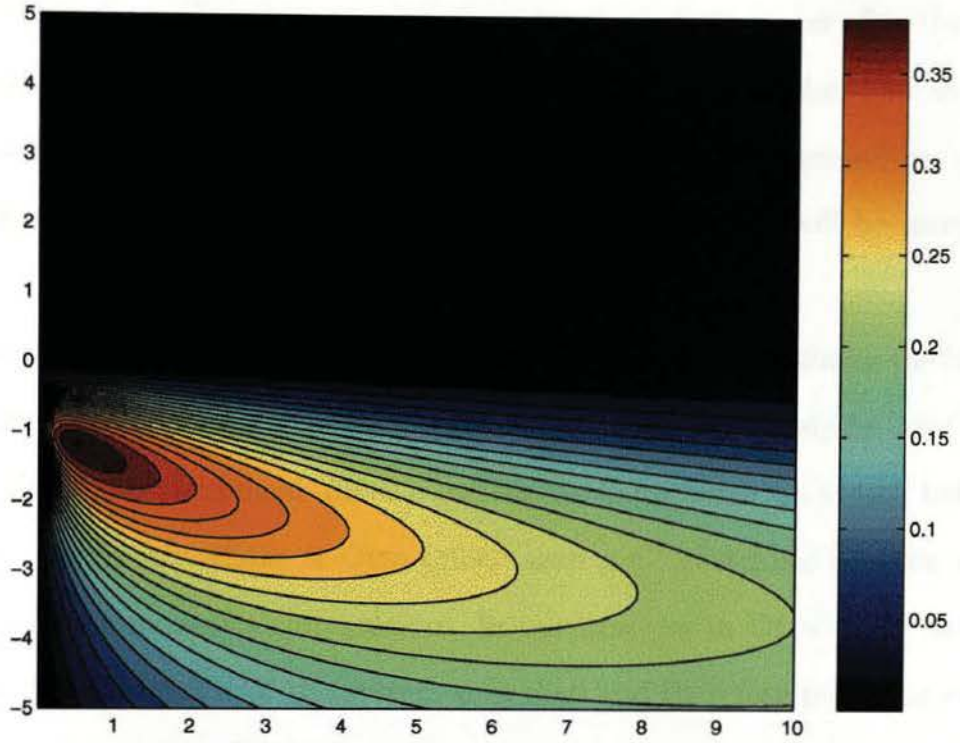

Fig. 2.3 (e) $\theta = 100$; $\max(\psi) = 0.3987$; fixed point (0.51,-1.21).

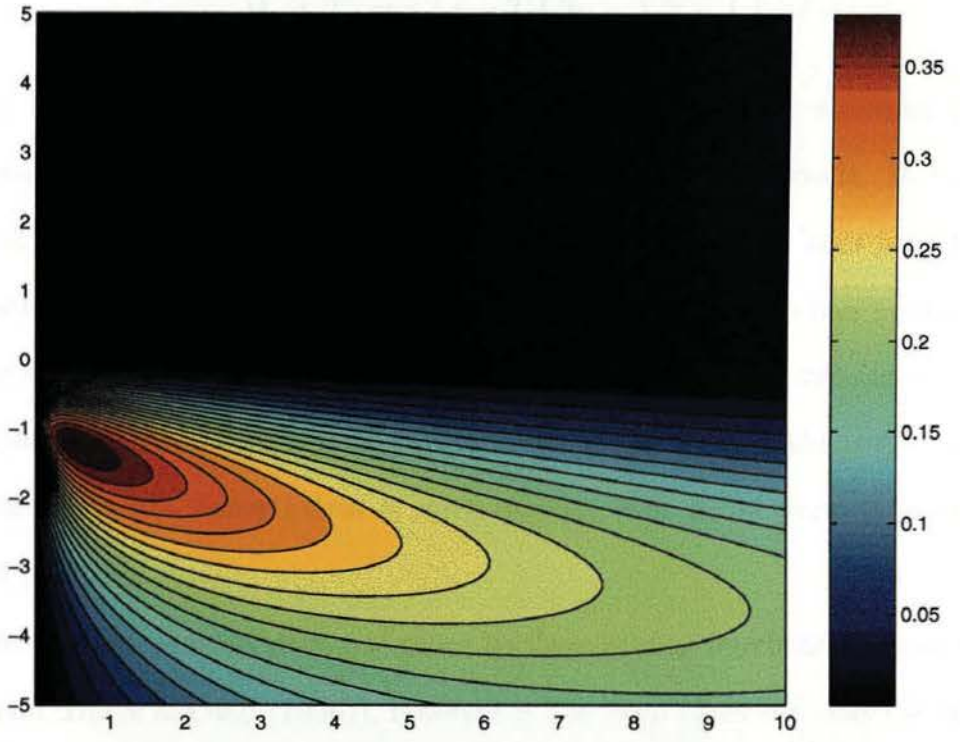

Fig. 2.3 (f) $\theta = 1000$; $\max(\psi) = 0.3971$; fixed point (0.51,-1.21).

Figure 2.3: Graphs showing the stream functions in both the upper and the lower half planes for varying values of θ with $\alpha = 1$. The colour bar indicates the value of the stream function for different areas of the plane while the '+' indicates the location of the fixed point. The values of the stream functions correspond to the speed of the fluid in these regions.

using cylindrical coordinates one can find the location of the tracer after the first stokeslet blink, and then repeat the same procedure for the second stokeslet. One should note it is understood that the first stokeslet pulse has ceased before the second has started. Also, with each stokeslet is an associated coordinate system which will be introduced in due course.

There are different switching protocol that can be used for defining the blinking action of the stokeslet. We need to specify a protocol, as done previously by Aref (1984), Blake & Otto (1996) and Otto et al. (2001), so that we know when we switch between the two stokeslets. Previously, Blake & Otto (1996) used a C^1 switching between configurations to help with the numerical integration. In our case, as in Otto et al. (2001), we want to reduce the description of the system to a map and therefore pulse the stokeslets with a δ-function form. This δ-function shows the temporal variation of the stokeslets and is taken to be

$$\Omega_n(t;T) = \delta\left(t - T\left(2n + 1 \mp \frac{1}{2}\right)\right),$$

where $n \in \mathbb{Z}$ and $2T$ is the period of the system. Here, the right stokeslet pulses at time $t = T/2$ and the left at $t = 3T/2$, and so on for subsequent periods. In experiments on SA, it is noted that the helical motion of the flagellum persists over a finite period and then ceases. Due to the nature of the flow (that is $Re \ll 1$) we can neglect momentum and hence we model the overall effect of this rotation as an upwards force, also operating over a finite time. In nature this cessation may well be so that the organism can recover from its activity, but nevertheless it does operate over finite periods interspersed with periods of inaction.

The micro-organism SA does not move its flagellum as much as other organisms (such as *Vorticella*, Blake & Otto (1996)), however it has been observed that the eddy structure is unsteady and this will promote chaotic advection. We have endeavoured to model this unsteadiness via the inclusion of a periodically moving stokeslet. The flow field associated with a point force is similar to that found to occur in the neighbourhood of a helical flagellum, in that a large toroidal eddy structure is created. The global

effect is one of a point force directed up the core of the helix. Again, referring to an inverted representation of Figure 2.3, we can see these toroidal effects. For larger T, the system is likely to become more chaotic due to the longer length of time between each event pronouncing the stokeslets individual effects. The overall effect may mean the flow becomes unsteady and following Aref (1984), a non-integrable behaviour may ensue. In the biological context with which we are concerned, it is this non-integrable flow we are interested in because it can lead to an efficient mixing régime within the fluid. This is important for organisms who feed from the flow of fluid around them. Any enhanced mixing they can create will be beneficial to their survival. When we let $T \to 0$ we find the system tending towards the integrable case because the fluid responds to the stokeslets as though they are acting 'together' rather than pulsing individually. We regard this case as similar to both stokeslets pulsing together which corresponds to a function of the addition of the stream functions. Again, following Aref (1984), this integrable behaviour will produce an inefficient mixing of the particulate matter within the flow due to the lack of stream lines which cross and tangle. The crossing of stream lines would create regions of mixing since this process could affect the structures of stability which are existent within the fluid.

2.3 The construction of the map

To determine the position of the tracer when it has been acted on by two blinking stokeslets, we initially need to find its position relative to the first stokeslet using cylindrical coordinates. The first stokeslet will act for an instant only, at time T_1 say, and then there will be no force acting until time T_2 when the second stokeslet acts. The second stokeslet will determine the next position of the tracer, and because both stokeslets have acted we say that the tracer has moved through one iteration of the system. We will later define this as a map. Notice that each blink of a stokeslet occurs at a distinct time and that they are both switched on and off instantly. It is now necessary to define this

mathematically.

We look for a map which describes the position of the tracer before the action of the n^{th} pair of pulses with the position after the action of the n^{th} pair of pulses. This map consists of two steps where the first step moves the tracer from the n^{th} to the $(n+\frac{1}{2})^{\text{th}}$ position and the second step moves the tracer from the $(n+\frac{1}{2})^{\text{th}}$ to the $(n+1)^{\text{st}}$ position. This is the point we consider the tracer to have moved to after the action of the n^{th} pair of pulses. This type of map will allow one to produce a Poincaré section which will indicate whether the action of the blinking stokeslet will give a chaotic mixing pattern or not. The Poincaré section shows the position of the tracer every period. The map is a stroboscopic image and shows how initial particles are progressed forward due to the action of the map. Dependent on whether a solid or scattered line is produced the map is either integrable or non-integrable, Hénon (1969). A schematic illustrating the production of a Poincaré section, defined as Σ, is shown in Figure 2.4 and Chapter 3 gives more details along with interpretations derived from the results. After many periods of the map the Poincaré section will suggest patterns which indicate the behaviour of the fluid over time.

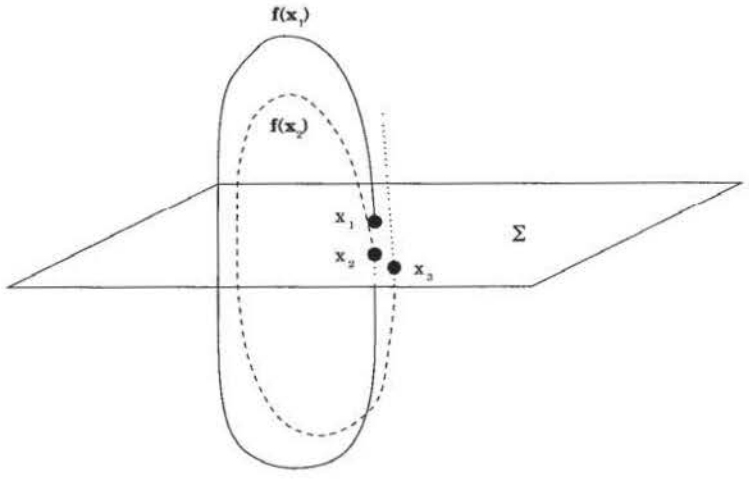

Figure 2.4: An illustration of the construction of a Poincaré section, labelled Σ. For comparison, Figure 1.2 indicates a Poincaré section when the map we are considering is of period two.

2.3.1 The explicit map

The simplest map we can define uses the velocities in terms of the stream functions in both the radial and vertical directions, and moves the tracer along due to the corresponding velocity for each pulse of the stokeslet. The map is obtained via an integration which gives the new position of the tracer in terms of the old position and velocity. Integrating the δ-function at the time of the first stokeslet pulse, $t = (2n+1)T/2$, we notice that during the interval that follows, i.e. $(n+\frac{1}{2})T < t < (n+\frac{3}{2})T$ (where $n \in \mathbb{Z}$), we have no motion due to neither of the stokeslets pulsing and the flow having no inertia. A similar calculation can be considered for the case of the second stokeslet pulse too. The integration is given by

$$\int_0^{2T} \dot{x}\,\mathrm{d}t = \int_0^{2T} \delta(t)\psi(x,y,t)\,\mathrm{d}t,$$

which we can rewrite as

$$\int_0^{2T} \dot{x}\,\mathrm{d}t = \int_{\frac{T}{2}-\epsilon}^{\frac{T}{2}+\epsilon} \delta\left(t-\frac{T}{2}\right)\psi(x,y,t)\,\mathrm{d}t \quad + \quad \int_{\frac{3T}{2}-\epsilon}^{\frac{3T}{2}+\epsilon} \delta\left(t-\frac{3T}{2}\right)\psi(x,y,t)\,\mathrm{d}t\,,$$

because we only need to integrate for the time at which either of the stokeslets are switched on due to the properties of the δ-function.

Following Otto et al. (2001), the explicit map is given by

$$R: \begin{cases} r_{n+\frac{1}{2}} = r_n + \dfrac{1}{r_n}\dfrac{\partial\psi}{\partial z}(r_n, z_n) \\ \\ z_{n+\frac{1}{2}} = z_n - \dfrac{1}{r_n}\dfrac{\partial\psi}{\partial r}(r_n, z_n)\,, \end{cases}$$

which gives the position of the tracer after one stokeslet has acted. The map is explicit because the new point $(r_{n+\frac{1}{2}}, z_{n+\frac{1}{2}})$ is dependent on the previous position of the tracer only. (Notice the point (r_{n+1}, z_{n+1}) would correspond to the position after both the stokeslets had acted, therefore completing one iteration of the map.) This is tantamount

to an Eulerian integration scheme where $(r, z) \to (r + u_r, z + u_z)$. Since the action of one stokeslet induces axisymmetric flow, then the angle ϕ is constant in this instance because the map R is considering a single stokeslet pulse. Due to the incompressibility of the fluid which we are considering, we know that the velocity field should be divergence free. Hence we require the Poincaré map to be area preserving; the map we have stated is not area preserving and so we must instead look at an implicit map together with a simple transformation of the cylindrical coordinates.

2.3.2 The implicit map (midpoint map)

We will consider the same type of scheme introduced in section 2.3.1 above, but first we present a coordinate transformation to give an area preserving map for use in the following implicit study. The symplectic transformation of the coordinates is given by

$$\eta' = r^2/2 \quad \text{and} \quad z' = z,$$

so that the new coordinates are (η', z', ϕ) (which are still cylindrical) and are defined relative to each stokeslet. In this coordinate system, we see by considering Figure 2.2 that $r^2 = x^2 + y^2$ implying $\eta' = (x^2 + y^2)/2$. As indicated in Figure 2.2, both stokeslets lie on $x = 0$ and are situated equidistance from $y = 0$. It is the new coordinate system which must be translated to determine the individual effects of the stokeslets on the particle. We non-dimensionalise the system, taking L as the typical length scale and T as the typical time scale. In the new coordinates we can state the stream functions as: for $z' < 0$ (the region where the stokeslets are situated)

$$\psi = \alpha \left[\frac{2\eta'}{(2\eta' + (z' + h)^2)^{\frac{1}{2}}} - \frac{2\eta'}{(2\eta' + (z' - h)^2)^{\frac{1}{2}}} + \left(\frac{2\theta}{1 + \theta} \right) \frac{2hz'\eta'}{(2\eta' + (z' - h)^2)^{\frac{3}{2}}} \right], \quad (2.1)$$

and for $z' > 0$

$$\psi = \alpha \left(\frac{2\theta}{1 + \theta} \right) \frac{2hz'\eta'}{(2\eta' + (z' + h)^2)^{\frac{3}{2}}}, \quad (2.2)$$

where $\alpha = FT/4\pi h\mu_1$, h is the non-dimensional location of the stokeslets below the interface and as before, $\theta = \mu_2/\mu_1$. The parameter α is used to represent the varying strength of a stokeslet but also includes the effects of length, time and viscosity. In the case studied here, when α is positive we consider the stokeslet acting in the positive z' direction (i.e. towards the interface below which the stokeslets are situated).

The map is defined as implicit if one can find the position of the tracer after the n^{th} pair of pulses by the use of intermediate coordinates. These intermediate coordinates, given by $(\eta'_{n+\frac{1}{2}}, z'_{n+\frac{1}{2}})$, are coordinates used as a step between the first and second stokeslet pulses occurring at times $t = (n + \frac{1}{2})T$ and $t = (n + \frac{3}{2})T$ respectively. Therefore, an implicit map is determined from an explicit map by altering the point at which the map is taken to act. It is necessary to have an implicit map because it will be more stable to use in the numerics than an explicit map. This will be important when we are considering the advection of points within a flow where they are required to be stable so the flow dynamics can be determined. We consider two steps in the implicit map which combine to give the full map. This creates the effect of the total 'pulse' and will eventually move the tracer to the $(n+1)^{\text{st}}$ position. The full map is defined as M where

$$M : \mathbf{x} \to R_2.R_1(\mathbf{x}), \tag{2.3}$$

taking the position of the tracer through one action or iteration of the system. The implicit maps R_1 and R_2 move the tracer due to the first and second stokeslet respectively. First, we have the map R_1 where

$$R_1 : \begin{cases} \eta'_{n+\frac{1}{2}} = \eta'_n + \dfrac{\partial \psi}{\partial z'}\left(\dfrac{\eta'_n + \eta'_{n+\frac{1}{2}}}{2}, \dfrac{z'_n + z'_{n+\frac{1}{2}}}{2}\right) \\ \\ z'_{n+\frac{1}{2}} = z'_n - \dfrac{\partial \psi}{\partial \eta'}\left(\dfrac{\eta'_n + \eta'_{n+\frac{1}{2}}}{2}, \dfrac{z'_n + z'_{n+\frac{1}{2}}}{2}\right). \end{cases} \tag{2.4}$$

This gives an implicit map which acts on the n^{th} position of the tracer to induce the effect

of the first stokeslet. The specific map given in (2.4) is only one of three cases we could have considered. As explained above, to make the map implicit we have merely chosen to alter the point where the map acts so that we now consider the intermediate point too. We could have incremented the z'-coordinate so that the map was implicit in z' using the intermediate coordinates $(\eta'_n, z'_{n+\frac{1}{2}})$, or equally we could have considered the η'-coordinate so that our two step implicit map would use the intermediate coordinates $(\eta'_{n+\frac{1}{2}}, z'_n)$, rather than $\left((\eta'_n + \eta'_{n+\frac{1}{2}})/2, (z'_n + z'_{n+\frac{1}{2}})/2\right)$. We would say in the respective cases, the map was implicit in η' or z' rather than being a midpoint map. In some situations it is possible to decide which map to use via physical arguments. However, in this instance where this is not the case, we choose to exploit the midpoint map. This map, called the Poincaré map, represents the most formal treatment of the inherent discontinuity by using the mean of the left and right limits (as would be exploited in a Fourier series evaluation of a discontinuous function).

The implicit midpoint map, R_1, moves the tracer to half way through the map such that

$$R_1 : (\eta'_n, z'_n, \phi'_n) \to (\eta'_{n+\frac{1}{2}}, z'_{n+\frac{1}{2}}, \phi'_{n+\frac{1}{2}}).$$

To complete the motion induced by the pair of stokeslets we require the map R_2 to move the tracer relative to the second stokeslet and give its final position completing the map as

$$R_2 : (\eta''_{n+\frac{1}{2}}, z''_{n+\frac{1}{2}}, \phi''_{n+\frac{1}{2}}) \to (\eta''_{n+1}, z''_{n+1}, \phi''_{n+1}).$$

We incorporate an alteration to the map R_1 to create the map R_2 via a change of the coordinates representing the stokeslets. As the second stokeslet 'pulses', the change of coordinates from (η', z', ϕ') to (η'', z'', ϕ'') is given by

$$\eta'' = \left[(x - x'')^2 + (y - y'')^2\right]/2 \quad \text{and} \quad z'' = z',$$

with (x, y, z) being the position of the tracer. This map in (η'', z'', ϕ'') is called R_2 and

defined as

$$R_2 : \begin{cases} \eta''_{n+1} = \eta''_{n+\frac{1}{2}} + \dfrac{\partial \psi}{\partial z''} \left(\dfrac{\eta''_{n+\frac{1}{2}} + \eta''_{n+1}}{2}, \dfrac{z''_{n+\frac{1}{2}} + z''_{n+1}}{2} \right) \\ \\ z''_{n+1} = z''_{n+\frac{1}{2}} - \dfrac{\partial \psi}{\partial \eta''} \left(\dfrac{\eta''_{n+\frac{1}{2}} + \eta''_{n+1}}{2}, \dfrac{z''_{n+\frac{1}{2}} + z''_{n+1}}{2} \right), \end{cases} \tag{2.5}$$

where R_2 describes the motion of the tracer from (η', z', ϕ') to (η'', z'', ϕ''). Notice that because the individual stokeslet effect creates an axisymmetric flow, then when we are in the plane containing the stokeslets the angles ϕ will be positive or negative of the previous angle. For example, in the plane of the stokeslets where we consider ϕ to be measured from the positive x-axis, the angle will be $\pm\pi/2$. Hence if the tracer begins between the two stokeslets then $\phi'_{n+\frac{1}{2}} \neq \phi''_{n+\frac{1}{2}}$. It may be possible if the tracer 'crosses' the axis of either of the stokeslets that $\phi'_n \neq \phi'_{n+\frac{1}{2}}$ or $\phi''_n \neq \phi''_{n+\frac{1}{2}}$. The full map defined as M in 2.3 could correspond biologically to one beat of the flagellum for example. Another situation which it could describe is the interaction of two adjacent flagella beating. Notice we are looking at the axisymmetric case here whereas in reality the particles will not always begin within the same plane as the stokeslets. We approach this in Chapter 4 where we look at a three-dimensional flow concerned with the map given above.

By increasing the value of α, we can increase the period or the force of each stokeslet and so examine the different stream lines which are produced. We can also vary the orientation of the stokeslets, with respect to both each other and the interface, to investigate the mixing of the fluid.

2.4 Discussion of the use of the midpoint map

We have briefly mentioned the various maps we can use to determine the fixed points and so here we consider in more detail the implicit map we call the midpoint map. As this study developed, the map we initially introduced was the implicit z map where we satisfied the condition for the map to be area preserving. During the course of this work,

all three maps have been used, each looking from a slightly different aspect at the results of the model. The third map to be considered, which has been dubbed the midpoint map, uses a combination of both r and z as implicit. In the midpoint map, the combination used is midway between the previous and the next points at each step. To explain the validity of this method, we examine the 'value' of the map as it approaches a point in time, T, where the delta function creates the pulse. We know in two dimensions the map can be given as

$$R: \begin{cases} r_{n+\frac{1}{2}} = r_n + \frac{\partial \psi}{\partial z}(\mathbf{r}) \\ \\ z_{n+\frac{1}{2}} = z_n - \frac{\partial \psi}{\partial r}(\mathbf{r}). \end{cases}$$

Depending on the coordinates of $\mathbf{r}$ the map will be implicit in z (when $\mathbf{r} = (r_n, z_{n+1})$) or implicit in r (when $\mathbf{r} = (r_{n+1}, z_n)$). Both of these maps do not show agreement in their results as we approach time T from either the left or right hand limits, i.e. as $t \to T$ they are not 'continuous'. We know both maps preserve areas when they act. By using an amalgamation of these implicit maps we can create both a map which is area preserving in nature and a map which has left and right hand limits equal.

The average of the right and left hand limits, $\mathbf{r} = ((r_n + r_{n+1})/2, (z_n + z_{n+1})/2)$, is the point we obtain which satisfies the mean value of the map at $t = T$. We call this the midpoint map because the limits from both the left and right converge at a point midway between the top and the bottom values of the range of the pulse, i.e. at the arithmetic mean of the function's value. This is also area preserving and hence provides a good compromise between the previous two maps.

2.5 Flow patterns due to horizontally displaced stokeslets

In all the maps, we have seen how the flow develops for both stokeslets acting in one direction. By considering the stream functions and altering the direction in which one of the forces acts, we can build a picture of what will happen to the overall flow picture.

Figure 2.5 gives an indication for a particular case of horizontally displaced stokeslets. Using MatLab it is easy to visualise how the flow develops as we move the stokeslets closer together. In Figures 2.5 (a, b, c), the left hand side stokeslet is pointing away from the interface whilst the right hand stokeslet points towards it. Colour bars have been included to indicate the opposing nature of the stokeslets via the values of the stream functions. We can see how the eddies around each stokeslet begin to affect one another as the distance between them decreases. In Figure 2.5 (b), we see how the eddies between the two stokeslets are beginning to coalesce whereas in the final figure, Figure 2.5 (c), the eddies have merged completely. For comparison, we see Figure 2.6 illustrates the same fundamental model of horizontal displacement but the stokeslets now act in the same direction. Again, we give the development of the flow by presenting three figures which show how the stream functions behave as the stokeslets move closer together. In this case the shading bar indicates the positive values of the stream function on both sides of the line $r = 0$.

2.6 Summary

The map introduced in this chapter will allow the construction of Poincaré sections which can aid the identification of chaotic regions. The midpoint map will indicate whether we have a system which shows a tendency towards chaos or not. We are interested in identifying the strength of the force (along with the other parameters in the problem) which will provide the optimal mixing in the inertia-free environment which SA inhabits. The mixing is restricted by the finite energy present within the system. The ability to compare theoretically predicted results with experimental results will validate the model and provide insight into how SA feeds along with the methods it uses to optimise feeding. Other chaotic and statistical measures, as mentioned previously, will also help to determine which regions see the most mixing, and if there are regions which are characterised by poor mixing.

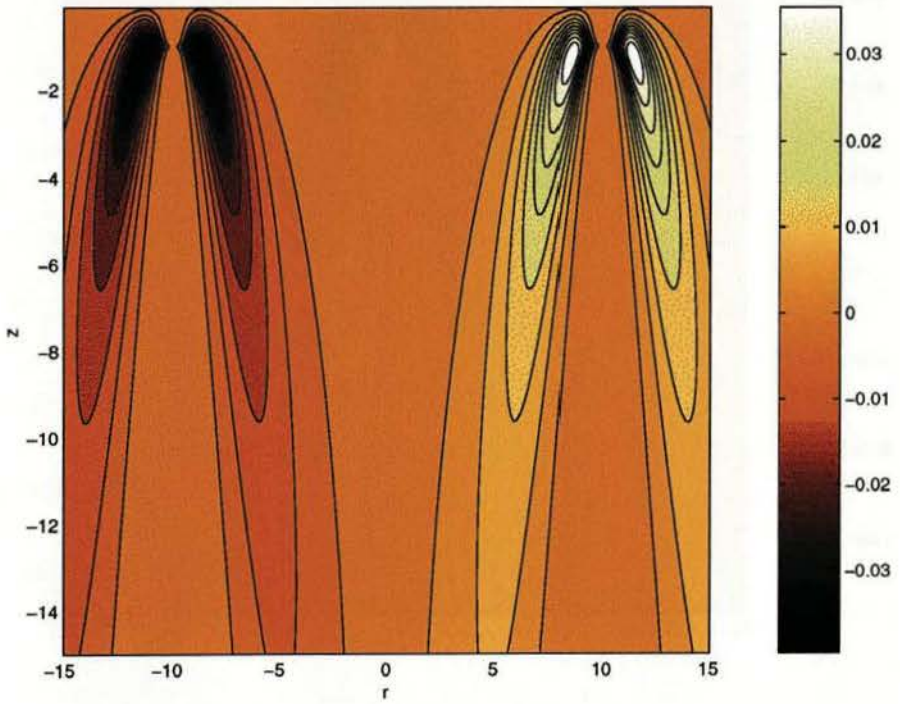

Fig. 2.5 (a) Stokeslets at $(\pm 10, -1)$.

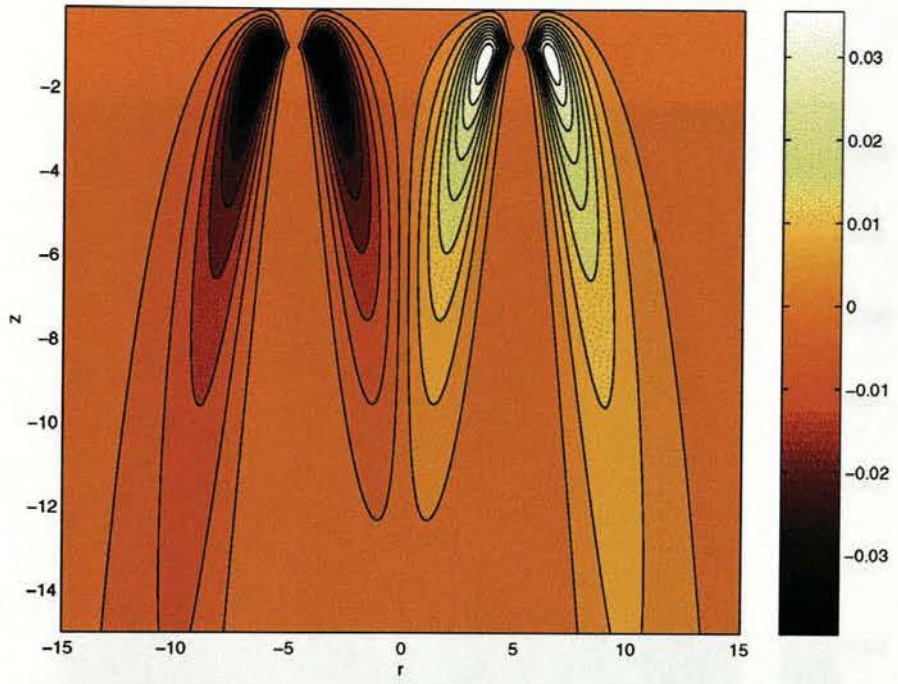

Fig. 2.5 (b) Stokeslets at $(\pm 5, -1)$.

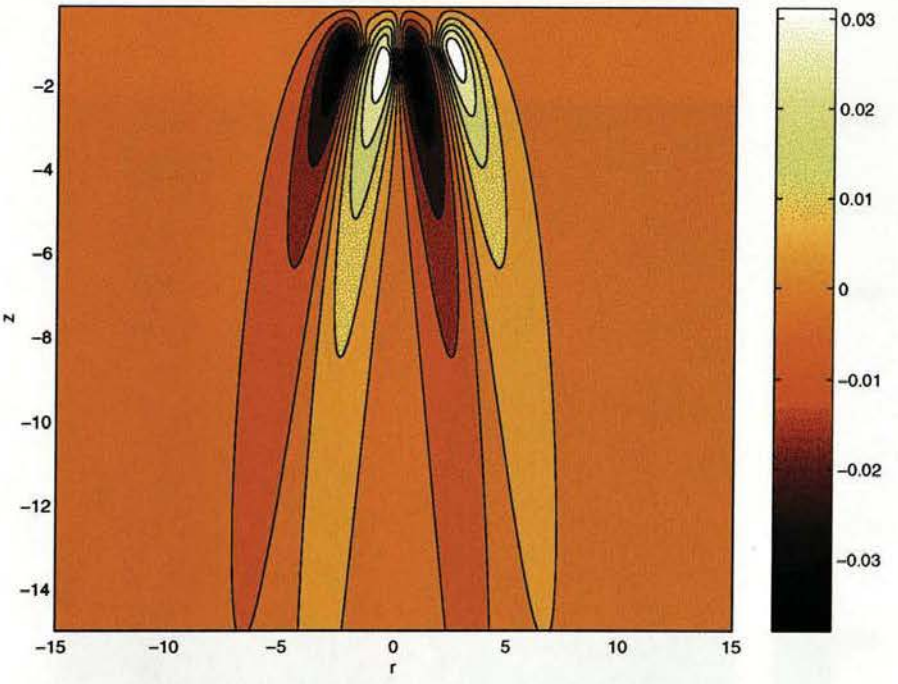

Fig. 2.5 (c) Stokeslets at $(\pm 1, -1)$.

Figure 2.5: The stream functions in two dimensions for two opposing horizontally displaced stokeslets. The map has $\theta = 10^6$ and $\alpha = \pm 0.1$ with the stokeslets positions given below each subfigure. The left hand stokeslet is pointing away from the $z = 0$ axis while the right hand stokeslet is pointing towards it.

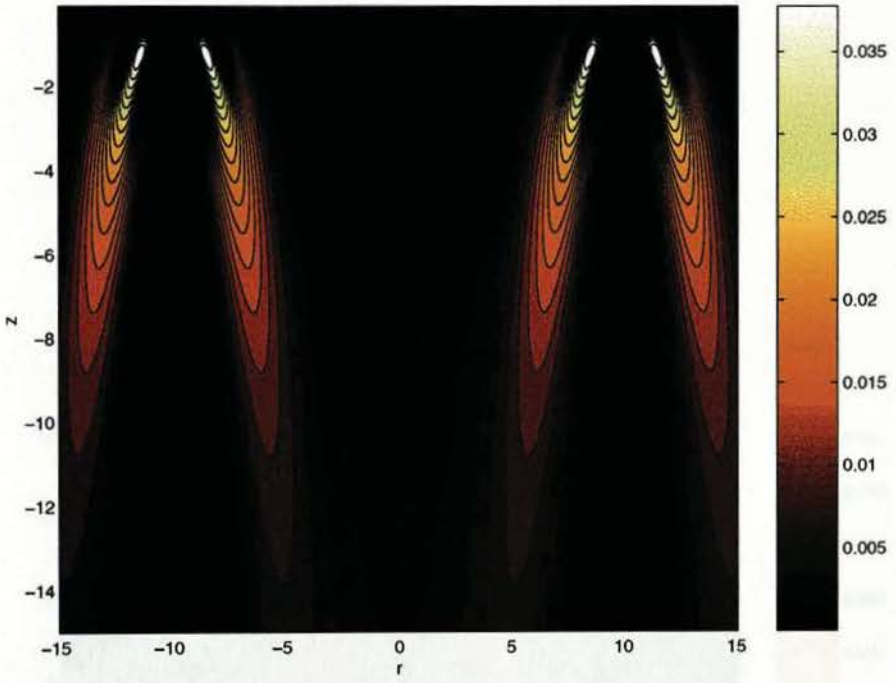

Fig. 2.6 (a) Stokeslets at $(\pm 10, -1)$.

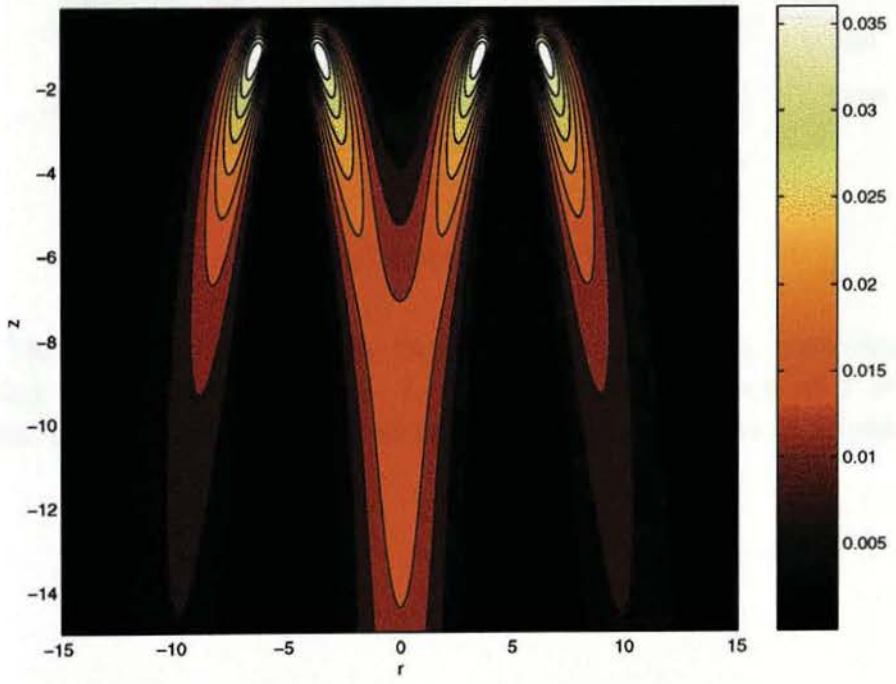

Fig. 2.6 (b) Stokeslets at $(\pm 5, -1)$.

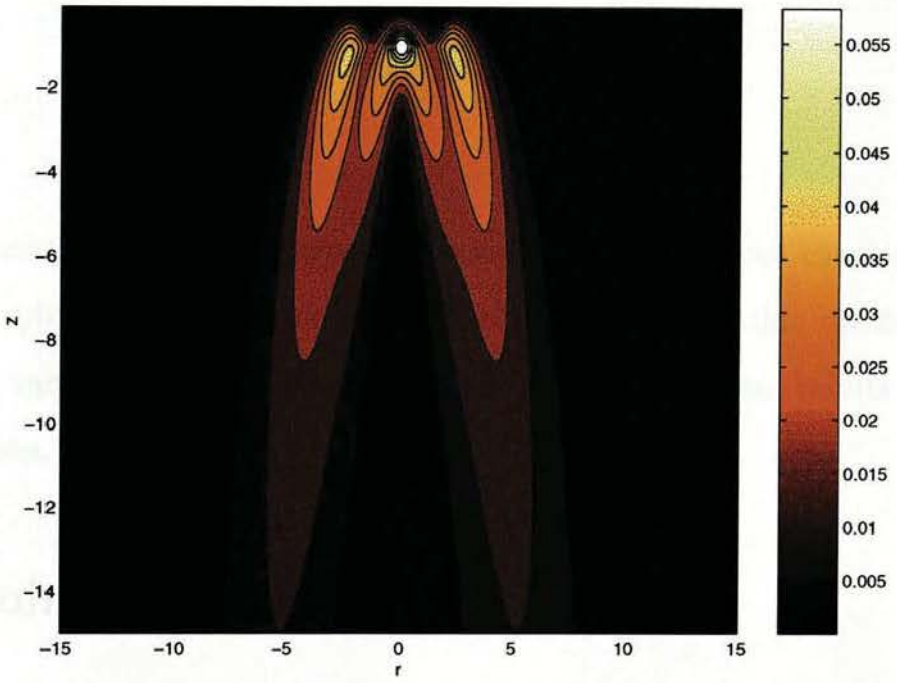

Fig. 2.6 (c) Stokeslets at $(\pm 1, -1)$.

Figure 2.6: The stream functions in two dimensions for two horizontally displaced stokeslets acting in the same direction, i.e. towards the interface at $z = 0$. The map has $\theta = 10^6$ and $\alpha = 0.1$ with the stokeslets positions given in the captions.

Chapter 3

MEASURES OF CHAOS INCORPORATING RESULTS

The mathematical model and formulae presented in the previous chapter are now developed and exploited to investigate how well mixed particles within the fluid become. By considering varying the parameters within the model, we present results for a number of different cases.

3.1 Poincaré sections

Poincaré sections are an important tool used to give a sense of chaotic mixing. They provide a systematic reduction in the complexity of a particular problem by reducing its number of dimensions. Poincaré sections convert a flow into a map by looking at sections sliced through a flow and therefore showing where a point will return to once it has completed a period of its motion. We now describe this type of chaotic measure in greater detail.

In a time-periodic system, this technique takes stroboscopic pictures of initial conditions placed on the plane (which is called the Poincaré section). Then, as time advances, whenever the particle passes through the plane an overall picture of the system becomes built up. The Poincaré section is composed of many images of a particle superimposed onto the plane with each image spaced due to the period of the system. Hence it gives an

overview of the character of the system. The Poincaré section will show regions where the tracer, dependent on its initial placement, experiences either a rotational or stretching motion. We note that if the map is aperiodic then successive points need not occur at regular time intervals. Fixed points of the map will have the same period as the system therefore returning to their initial position once a certain number of periods have been completed. By observing features we call island structures, the period of the orbit can be found. For example, if we are observing an orbit with twice the period of the underlying system then we will see just two individual points on the Poincaré section. The map will take the tracer from one intersection to the other with each iteration of the map. Once the number of orbits have been completed which correspond to the period of the system, we are at the initial position again. This type of periodicity was shown by the schematic in Figure 1.2, where Σ represents the Poincaré section.

The full map M will produce Poincaré sections which allows one to look for the main features of the flow. The map M is given by

$$M : \mathbf{x} \to R_2.R_1(\mathbf{x}),$$

from the previous chapter, see equation (2.3). This is a composition of the two implicit maps, R_1 and R_2, given in detail by equations (2.4) and (2.5). The figures within this current section show Poincaré sections for varying values of θ (the parameter which will determine the ratio of the viscosity between the two fluids) and α (which amongst other values will specifically allow the variation of the magnitude of the stokeslets). Notice that varying α will also be equivalent to varying the period of the system. If the force of the stokeslet is strong, we expect extensive mixing to occur. This high degree of mixing also occurs when the length of time between the stokeslets acting is large, due to each particle feeling the individual rather than the combined action of the forces. The values of θ will show in limiting cases when the surface can be treated as a solid or a free surface. These limiting cases have been mentioned in the previous chapter.

We require three dimensions to be able to define a Poincaré map. In the case of the axisymmetric problem we use the two coordinate axes and time, but when we look at the three-dimensional model the three coordinates are those we are using to describe the system. When we have three coordinate directions in the later model this will not be possible when there is no time variation in the system, see Chapter 4. Integrability of the system is considered to determine the chaotic motion of the system. The integrability means one can find constants in the system which will allow the prediction of the motion of particles. If we do not have enough constants to describe the system then it is non-integrable and the motion of the system unpredictable. Conversely, if we do have enough constants to predict the motion then the system cannot be chaotic.

Many of the features we will see on Poincaré sections can be explained in terms of homoclinic and heteroclinic points, see Ottino (1989) for more details. These are terms used when describing dynamical systems and refer to points where the cycles of the solution meet. If we have two manifolds which meet and did not originate from the same fixed point in the plane, then their connection is heteroclinic. Conversely, if they originated at the same fixed point then their intersection is homoclinic. When these intersections meet tangentially, we have the stable and unstable manifolds merging together. However when these points are formed at a non-tangential intersection, i.e. the cycles cross, then there will be an infinite number of these intersection or 'tangles'. In direct analogy with our problem and in a similar context to work by Aref & Balachandar (1986), we can describe regions of the Poincaré sections using these ideas. The tangles are represented theoretically by the indicators of chaos which we see appearing on the Poincaré sections. These tangles will result in greater mixing within the phase space.

We can now extend the ideas introduced above and identify the types of intersections of the manifolds which we see within Poincaré sections. The island structures seen in Poincaré sections are a measure of the system's integrability. At the centre of each island structure we can find a fixed point (albeit of a higher period). These fixed points are also elliptic points because they are situated at the centre of the islands and feel rotational

motion. They will be the last of the elliptic points to become hyperbolic. One finds situated between each elliptic point a hyperbolic point. This interlacing of hyperbolic points between elliptic points can be seen on the Poincaré sections. Hyperbolic saddle points, by their definition occur at the intersection of stable and unstable manifolds and so any areas close to hyperbolic points will experience a compression in the stable direction whilst undergoing an expansion in the unstable direction. The expanding, unstable direction is the direction which causes points to move away from the hyperbolic point. Hence the regions around the hyperbolic points are the areas where chaos is observed first.

To generate Poincaré sections, we start by considering points in the plane within which the stokeslets are situated. The axisymmetric system has one temporal and two spatial dimensions. We form a Poincaré section by considering the intersection of this space with the plane defined as $t = nT$, $n \in \mathbb{Z}$. Hence M is in effect a return map. Poincaré sections are generated by progressing a number of particles or points forward through time. An individual particle's position after each period of the map is indicated via a dot on the Poincaré section. In this case, the numerics which were involved to plot the Poincaré sections required the solution to equations given by the maps R_1 and R_2 and hence determining the next position the tracer moves to (see section 2.3).

The remainder of this section is divided into two main parts. The first shows the Poincaré sections for the previous work of the vertically displaced stokeslet case (Otto et al. (2001)) and the second for the recent original work of the horizontally displaced case in which we are most interested. Both are included to give a concise representation of previous and new work. We also include details of the bifurcation values for both these cases. This will indicate when we have transition to global chaos.

3.1.1 Vertically displaced stokeslets

By varying the value of θ, we observe that for larger values the flow exhibits more signs of chaos in a wider area of the plane. Also, as the force of the stokeslets become stronger corresponding to an increased α, the stokeslets have a greater effect on the tracer even

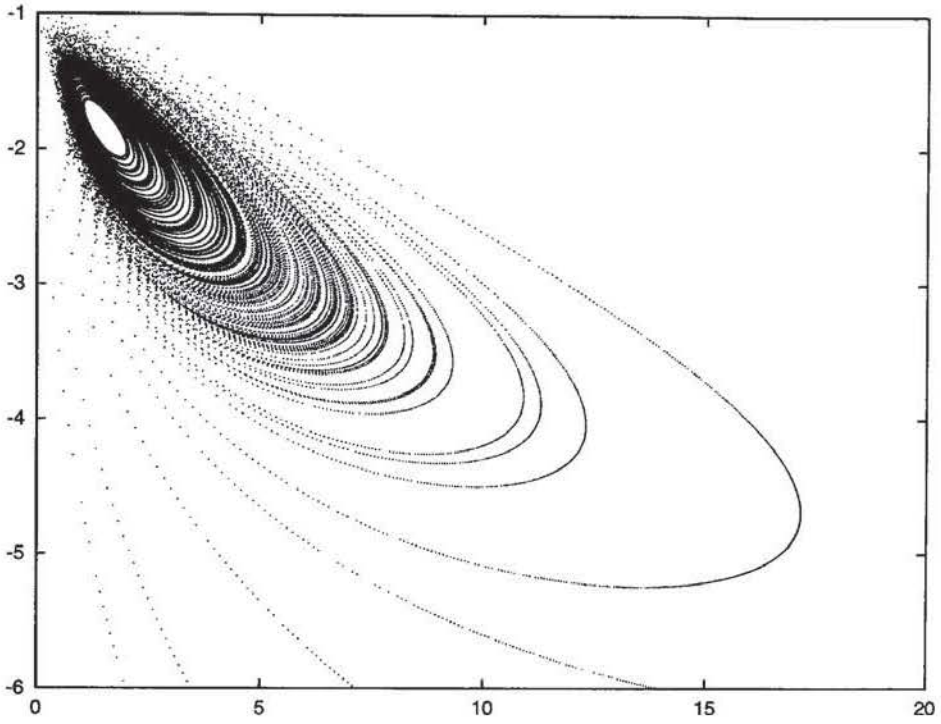

Fig. 3.1 (a) $\theta = 2$

though the ratio of the viscosities of the two fluids may be small. This is explained in more detail in the sequence of figures which follow (Figures 3.1 – 3.3).

Figure 3.1 shows Poincaré sections for varying θ with a constant value of $\alpha = 1$. Notice there is a scale change after Figure 3.1 (a) but this simply enables one to see more of the detail in the structure of the Poincaré section when θ is larger. For smaller θ we see the trajectories close to the fixed point form continuous lines. There are no island structures visible here (even if viewed using a smaller scale). If this smaller value is compared with the higher values of θ, corresponding to a larger difference in viscosity between the two fluids, more complex structures are seen. Observing Figures 3.1 (b) and (c) we can see that closer to the fixed point more scattering has occurred and there are now very visible island structures.

When we increased α to a value of 2, shown in Figure 3.2, we again see a marked variation in the Poincaré sections as θ becomes larger compared with the corresponding graphics in Figure 3.1. The increase in α corresponds to a stronger stokeslet force and

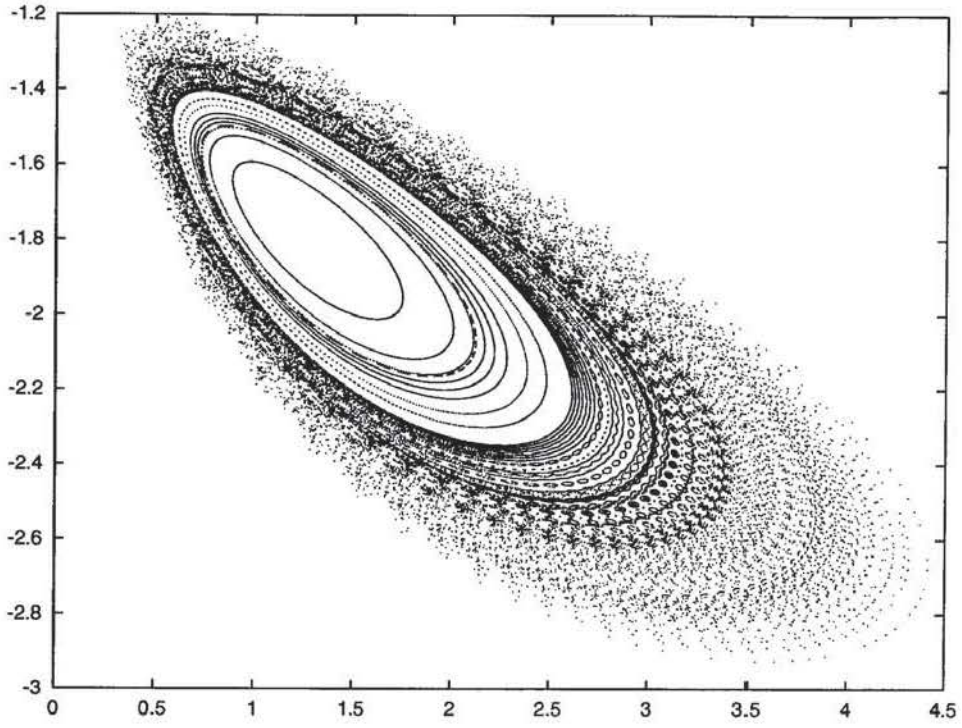

Fig. 3.1 (b) $\theta = 10$

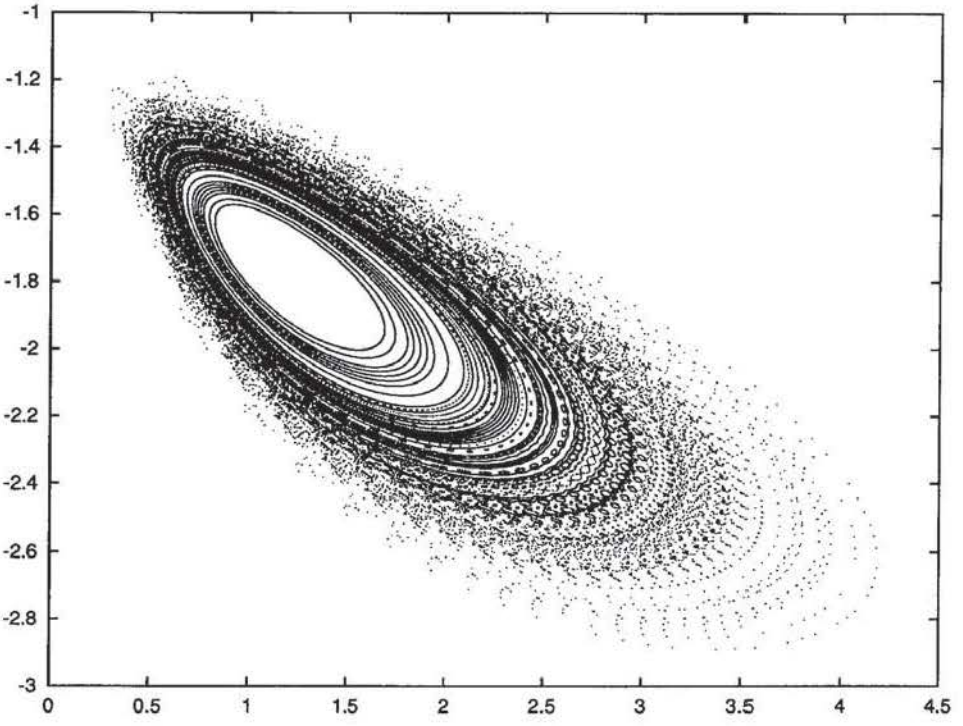

Fig. 3.1 (c) $\theta = 15$

Figure 3.1: Poincaré sections for $\alpha = 1$ with varying values of θ. Note the scale change for the last two subfigures compared to the first.

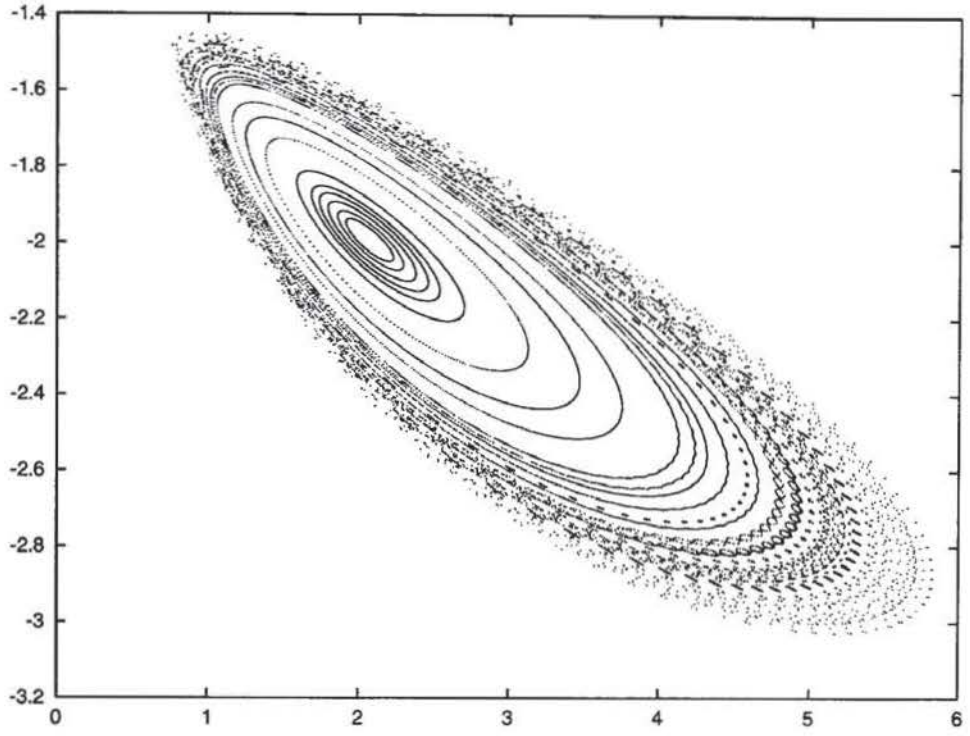

Fig. 3.2 (a) $\theta = 2$

so we expect to see a greater tendency towards the formation of chaotic structures (or equivalently the destruction of integrable structures). This is because the tracers will be moving through each period faster due to a larger value of α. The indicators of chaos we see emerging occur for values as small as $\theta = 2$ where one observes island chains forming at the periphery of the central fixed point structure, even though the scale is slightly larger than for the other figures which follow for $\alpha = 2$. Notice the orientation of some of these islands along their long axis does not always follow the direction of the elliptic shape of the eddy, see Figure 3.2 (c). This may indicate a variation in the directions along which stretching of the tracers occurs and hence the overall degree of mixing.

As θ increases, the degree of scattering becomes highly amplified, compare Figures 3.2 (b) and (d). Note the region bound by integrable curves becomes smaller with each increase in θ. Points that start close to the fixed point soon tend towards infinity if they are not trapped within one of the closed tori which limit the flow. These tori are common structures in flows which do not show chaotic mixing and they are illustrated on Poincaré

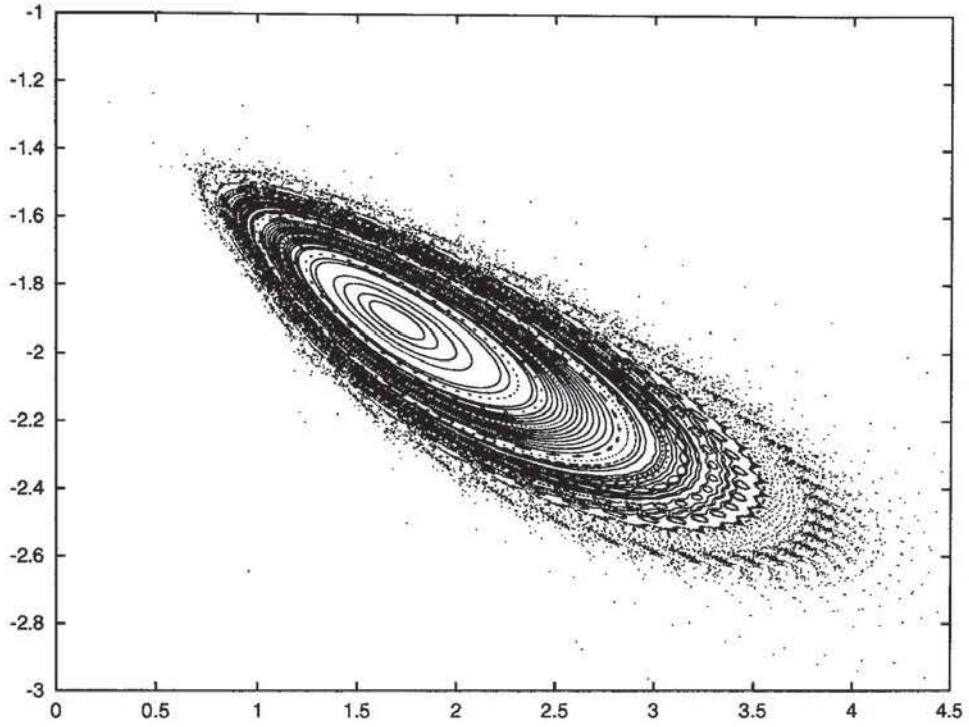

Fig. 3.2 (b) $\theta = 3$

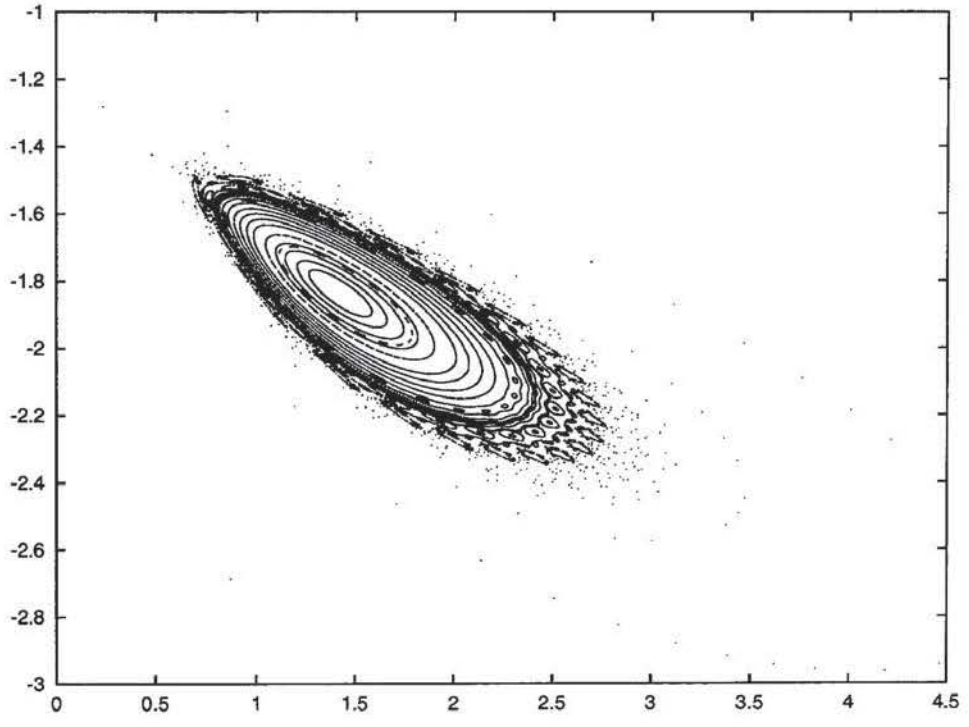

Fig. 3.2 (c) $\theta = 5$

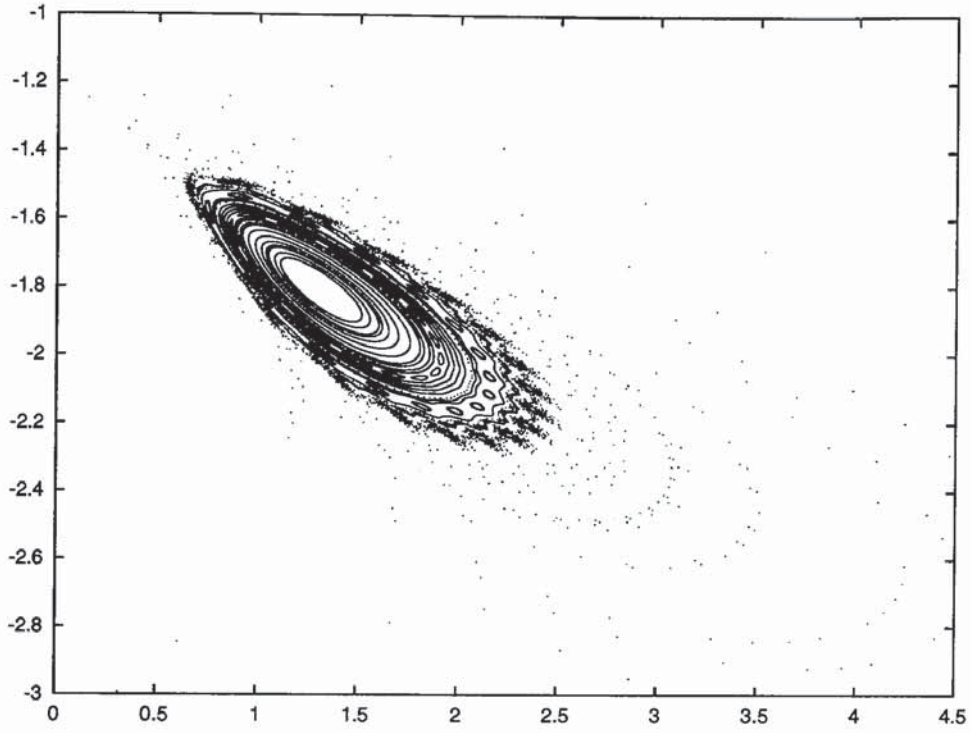

Fig. 3.2 (d) $\theta = 7$

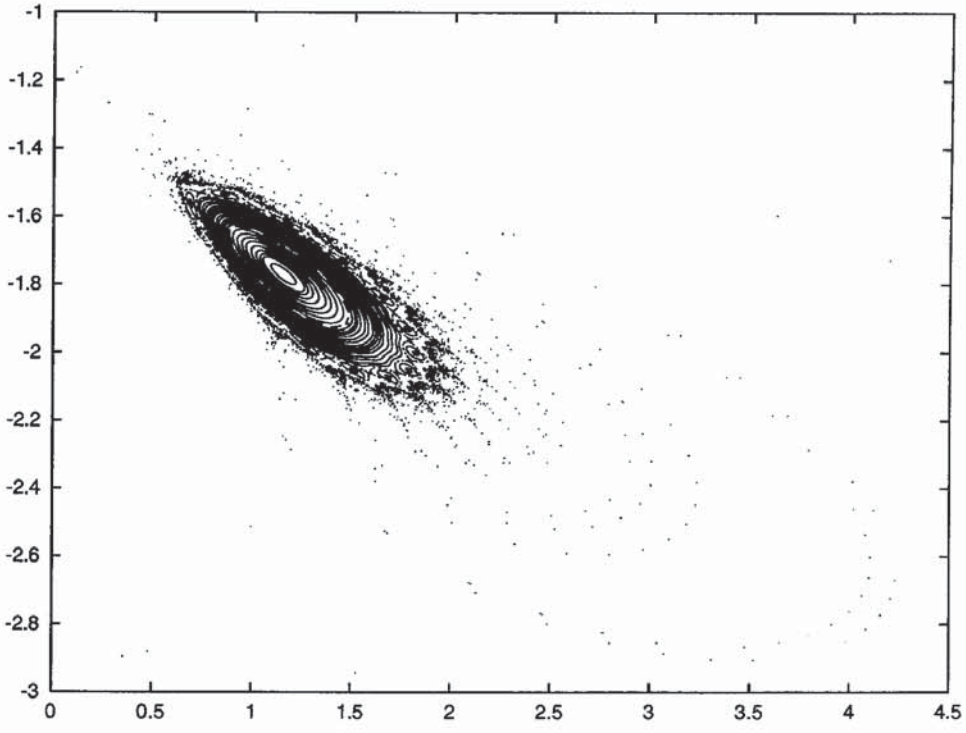

Fig. 3.2 (e) $\theta = 15$

Figure 3.2: Poincaré sections for $\alpha = 2$ with varying values of θ. Notice that the first two subfigures have a different scale to the others.

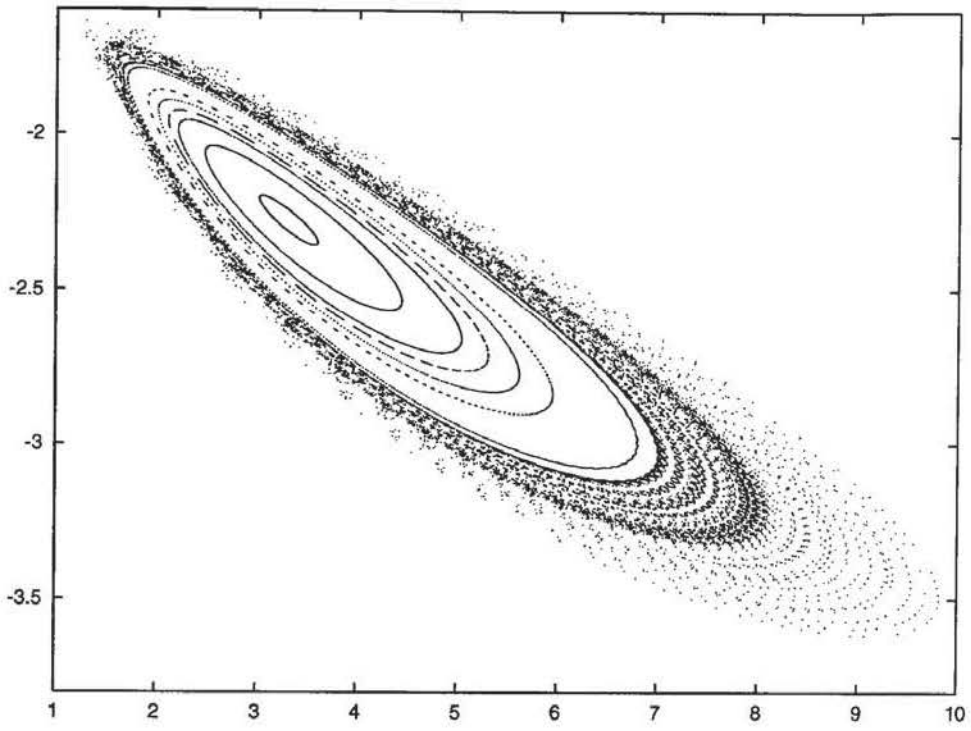

Fig. 3.3 (a) $\theta = 1$

sections as closed loops. When θ is much larger we observe only a concentrated number of points remaining around the fixed point, i.e. a small region of islands, and the rest of the points escape to be scattered around the plane, see Figure 3.2 (e).

We take a few sentences to briefly explain the bifurcation value of α as the value at which the fixed points of the map move from being elliptic to hyperbolic. It is found via consideration of the Hénon index of the map. We define the Hénon index below in section 3.3 but it is a measure which depends on the eigenvalues of the Jacobian of the map. When the eigenvalues are such that the point becomes hyperbolic, the Hénon index will indicate this and allow one to determine the bifurcation value of α at the fixed point. Where α is very large and possibly close to its bifurcation value, there is a limited amount of information we can collect from the Poincaré sections. This is shown in Figure 3.3. In these final figures where $\alpha = 4$, even for smaller θ we observe elements of chaos illustrated by a number of island structures and a degree of scattering. Figure 3.3 (c), where $\theta = 3$, is the largest value of θ we include for $\alpha = 4$ because by considering the scale we can

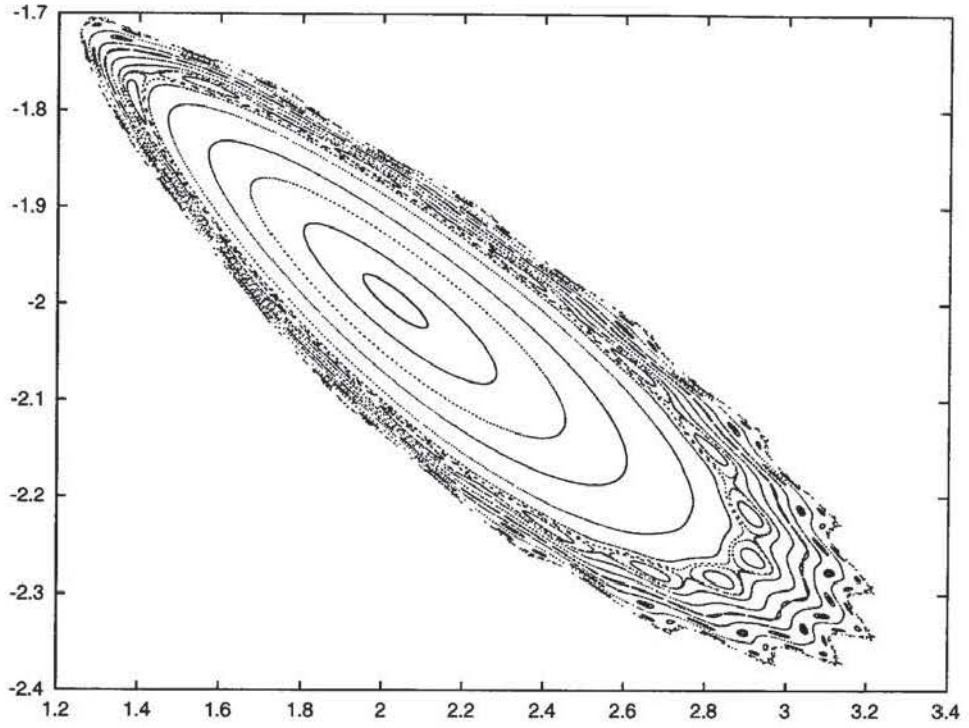

Fig. 3.3 (b) $\theta = 2$

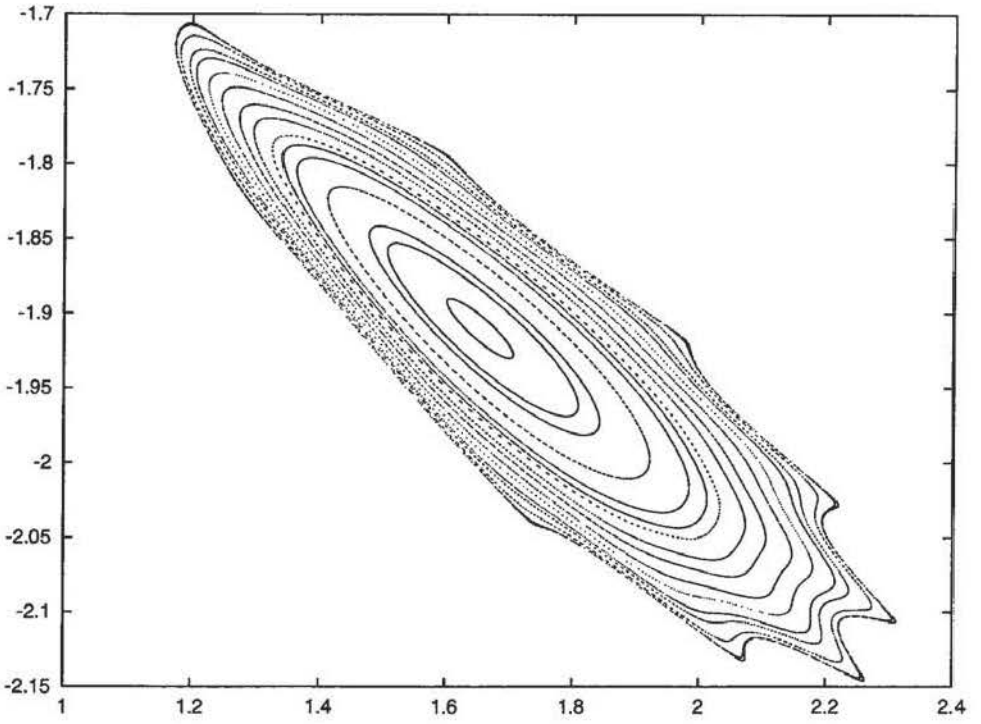

Fig. 3.3 (c) $\theta = 3$

Figure 3.3: Poincaré sections for $\alpha = 4$ with varying values of θ. Note that the scale has changed significantly between the first and the following two Poincaré sections.

observe the unstable structures in close proximity to the fixed point. Therefore due to these unstable points, when we begin to investigate the path of any points outside the integrable limits shown by the bounding curves, we find they tend to infinity quickly.

An interesting feature relating to the periodicity of the points which can be observed on the Poincaré sections, considers small changes to the parameters describing the problem. The underlying theory behind a change in the periodicity is related to the length of time it takes a particle to complete an orbit. We can define a rotation number relating the number of orbits a particle will make along a torus before it returns to intersect the Poincaré section. If the rotation number is rational, the denominator defines the number of orbits a particle makes before returning to its initial position on the Poincaré section. In this case an island chain could be formed. However, if the particle never returns to its initial position, then the rotation number is irrational. In this case the irrational orbits are also known as quasiperiodic, see Ottino (1989). Therefore, when we change α by a small amount, the length of time it takes to complete an orbit will change slightly too. Hence, if the rotation number can no longer be expressed as a rational then we get no island structures and no fixed points. If the rotation number remains rational, the ratio between the integers may still have changed. In this case the number of islands we observe changes implying that the periodicity alters. This is the reason fixed points vary for different values of α. This can be demonstrated via the two following examples.

We look further at the actual details of the island structures for small changes in the strength of the force governed by α. For example, if we take $\alpha = 1.2$ we can generate Poincaré sections with a chain of islands which have period twenty two when $\theta = 10^6$. By perturbing the force slightly so that $\alpha = 1.19$, we can observe similar structures forming where close examination of the fixed points of the islands reveals a small change. When $\alpha = 1.2$ an example of the fixed point for a particular island is $(1.2129, -1.4841)$ but with a change in α to the value 1.19 the corresponding fixed point is located at $(1.1985, -1.4834)$. The period of twenty two remains the same for both values of α. Similarly, we can see the same type of shift for another of the islands where the fixed

point moves from $(0.5959, -1.5640)$ to $(0.6026, -1.5669)$. The next example illustrates another type of difference found by altering the strength of the force. This involves a change in the actual period of the islands which pass through the point we are taking as a reference.

When one sets $\alpha = 1.825$, the distribution of islands looks remarkably different to that which we found for the other relatively similar values of α given in the example above. We now have more islands which is an indication that the periodicity is higher. Following the same procedures as above, we find the values of fixed points are given as $(1.2793, -1.5039)$ and $(1.1985, -1.4834)$ for islands located as close as possible to those cited for the two previous values of α. Again this shows the consequence of a small change in the value of α, in this particular example causing a change to the periodicity. There are no figures provided to illustrate this because they are similar to those Poincaré sections shown throughout this section.

3.1.2 Horizontally displaced stokeslets

We consider examples of Poincaré sections for the alternative case of horizontally displaced stokeslets where one can show representations of the tracer particle relevant to work in three dimensions, discussed later in Chapters 4 and 5. Figure 3.4 illustrates a selection of these Poincaré sections for the horizontally displaced stokeslet case. We show fewer examples of these Poincaré sections because the general patterns follow similar lines to the vertically displaced stokeslet case. The figures included show some of the interesting and significant features we find in these Poincaré sections.

Figure 3.4 (a), where the values of θ can be considered as infinite, i.e. $\theta = 10^6$, is equivalent to the representation in the physical system of a solid boundary situated above the stokeslets. We include two cases showing θ at smaller values so that we can use higher values of α in the numerical code without having the concern of escape from the map, see Figures 3.4 (c) and (d). These smaller values of θ, as mentioned before, will correspond to the surface above the stokeslets being less rigid. We mention briefly again the special

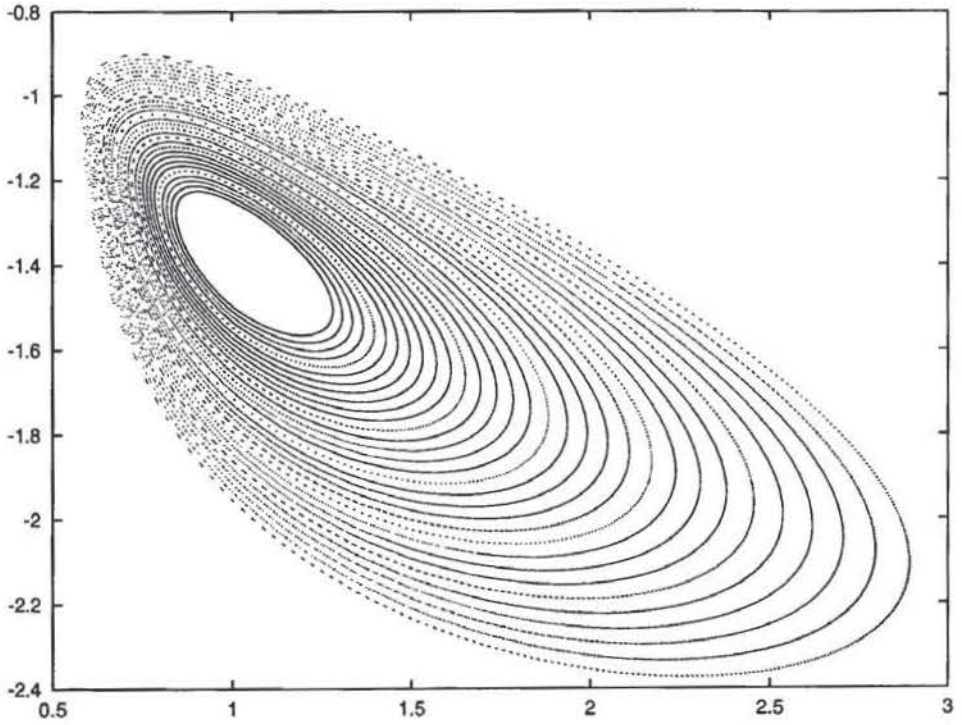

Fig. 3.4 (a) $\theta = 10^6, \alpha = 0.1$

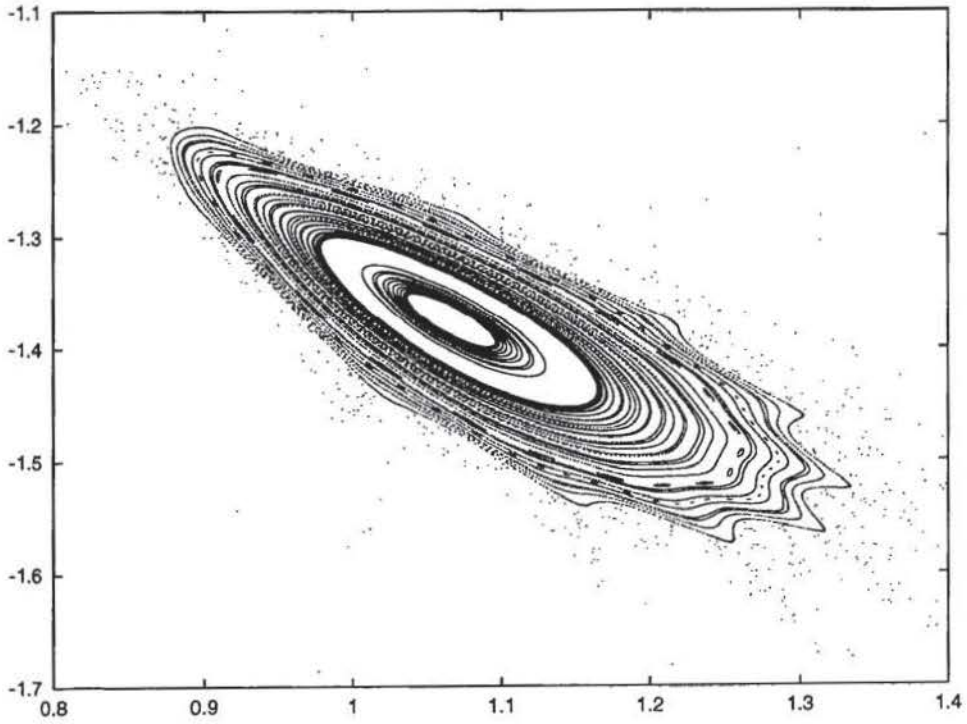

Fig. 3.4 (b) $\theta = 10^6, \alpha = 1.0$

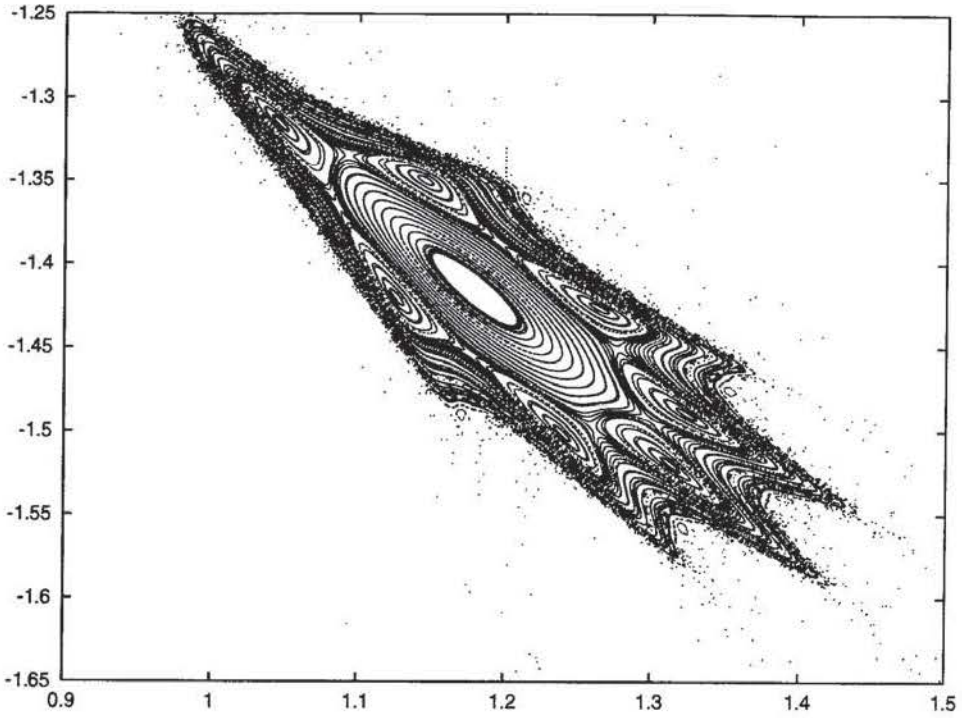

Fig. 3.4 (c) $\theta = 10, \alpha = 1.5$

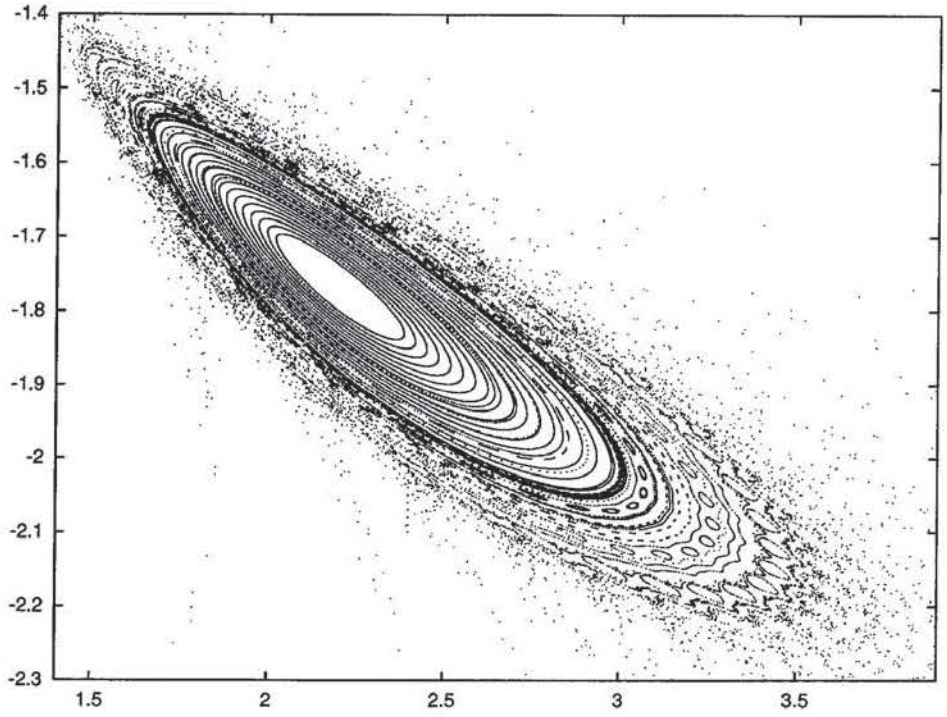

Fig. 3.4 (d) $\theta = 1, \alpha = 2.5$

Figure 3.4: Poincaré sections for horizontally displaced stokeslets. Note the scale and the values of θ and α change for each subfigure.

case corresponding to $\theta = 1$ when the viscosity of the two fluids are equal. There is no physical representation of this case. Again, as for the previous case of vertically displaced stokeslets, we can locate fixed points of the map and show for small variations in α, the periodicity of the map will change. It is not instructive to include these details here because they are similar to the vertically displaced stokeslet case.

Commenting on the periodicity of the map for horizontally displaced stokeslets, it is again indicated by the structures called islands which are composed of points of the map. Referring to Figure 3.4 (c) we observe seven of these islands denoting a collection of many points composing the islands. Because there are seven islands, each point must move through seven iterations of the map before returning to the proximity of its initial position. The central point is described as a point of period seven. The period will change for the map dependent on the parameter values we are using to describe the problem, such as the period of blinking of the force. For example, in Figure 3.4 (d) where the parameters are different to those in Figure 3.4 (c), more island structures are observed. The elliptic point associated with each island is not likely to move far from its initial position over time and hence is not associated with good mixing due to its rotational movement. Between the elliptic points however are situated hyperbolic points which show stretching away from their initial position over time. The hyperbolic points have the same periodicity as the elliptic points between which they are situated (again indicated via the number of island structures present). Where we have these hyperbolic points we tend to find good mixing. This is due to the intersection of stable and unstable manifolds occurring at such points. Section 3.3 gives more details on determining elliptic and hyperbolic points via the Hénon index.

The Poincaré sections for the horizontally displaced stokeslets can indicate, via their appearance, the level of integrability of a system. An integrable system is depicted in Figure 3.4 (a) where we can see solid smooth curves. When the system becomes non-integrable then the lines on the Poincaré section become broken and dotted as in Figure 3.4 (d). Even in this figure we can still identify both regions of scattering and regions

of integrability so the system is not completely or globally chaotic. However, there are critical values of the parameters which indicate when the system bifurcates (that is the central fixed point becomes hyperbolic in character). Finding the bifurcation value for α gives the value of α above which one has a chaotic system for every value of θ. Again, more details on the Hénon index which allow one to find this value of α are given in section 3.3.

3.1.3 Summarising Poincaré sections

Although Poincaré sections indicate spatial locations from which particles are likely to become well dispersed, they are also computationally expensive to generate, i.e. many time steps have to be taken before the figures included could be created. It is therefore important to note that an aphysical number of periods have to be executed in relation to the experimental observations before we arrive at the useful data. This is because in biological systems there is only a finite amount of energy which can be used to generate the flagellum beat and hence a limited number of periods. The numerical methods we use to generate the Poincaré sections involve solving the implicit map using the inbuilt routine `fzero` on MatLab. This is a hybrid scheme of root finding routines: bisection, Newton-Raphson and fixed point iteration. The tolerance is 10^{-10}. By combining information from the Poincaré sections along with other data in the following sections, we can build up a global picture of the system.

3.2 Lyapunov exponents

There is another measure which is useful when attempting to characterise how well mixed the fluid becomes. The measure we use for this quantification of mixing is the Lyapunov exponent, see Ottino (1989). This measures the divergence of the initial conditions of the system. It is calculated by considering a small segment or length between two particles in the fluid. After a set period of time the image length is compared to its original length.

Hence the Lyapunov exponent is related to the local exponential instability. Dependent on the time scale over which this divergence is considered, one can gain either the finite or infinite time Lyapunov exponent. In biological flows we want to find how well the fluid will mix over a finite time scale and so the infinite Lyapunov exponent is of limited use in this case.

The higher the dimension of the flow, the greater the possible number of Lyapunov exponents there are. In theory, we could have a different Lyapunov exponent for each of the linearly independent direction vectors which describe the system. The maximum Lyapunov exponent corresponds to the expansion aligned with the average direction of most expansion of the system. Therefore it gives only a rate of stretching and is not a direction.

Consider the images of two neighbouring points as a map, M, acts on them. The points are initially situated a small distance apart and after the map has acted on them the distance will either have expanded or contracted. In either case, by comparing the distance between the images with the distance that separated the initial points, we can quantify the degree of expansion or contraction the map has had on the points. This method often becomes infeasible if the expansion action of the map is large. When the ratio of the distance between the points is smaller than one, the map is contracting (decreasing the distance between the points). A small exponent illustrates the flow is mostly rotational in that region, showing little divergence from the initial conditions. If the ratio is greater than one, the map is expanding (increasing the distance between the points). A large amount of stretching after a certain fixed time scale indicates extensive mixing within that region of the system. This would be characterised by a large Lyapunov exponent. This is explained further in Ottino (1989) who notes 'positive Lyapunov exponents imply an exponential rate of stretching of material elements, and hence, good mixing'. However, to reach a limit which would allow one to determine this measure requires a prohibitively large number of iterations of the map, which is often not realistic in physical systems. We ideally want the system to reach a well mixed state within a small number of periods, without

having to exert prohibitive levels of forcing (which corresponds to a large expenditure of energy). In the case of a flow which is growing exponentially, we often rescale or normalise the distance between the image points and then perform the map on these renormalised points. This is illustrated in Figure 3.5 which shows both the methods explained above.

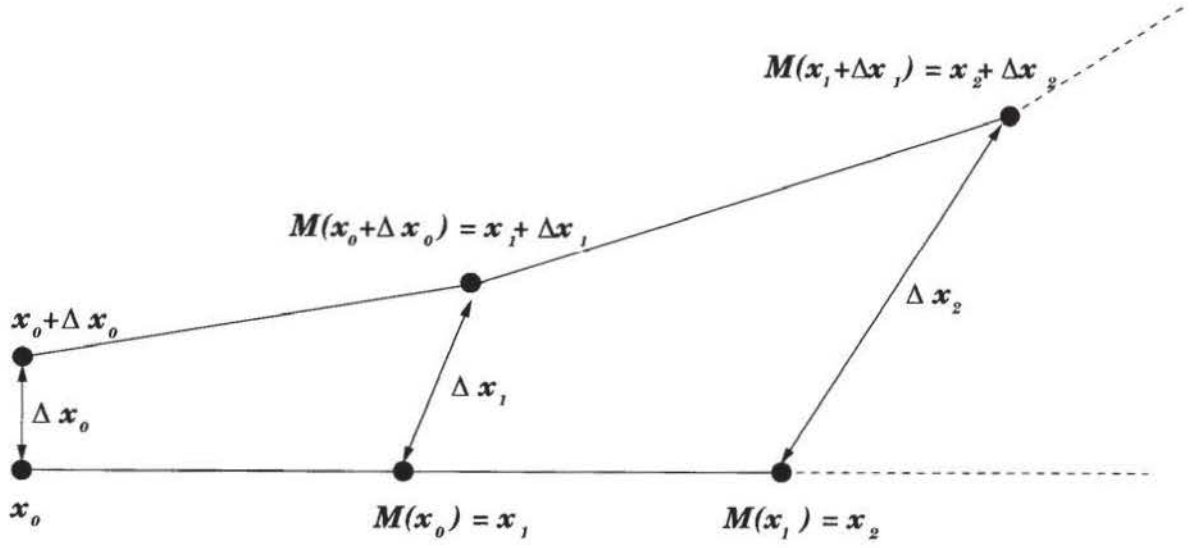

Fig. 3.5 (a) Expanding flow without normalisation

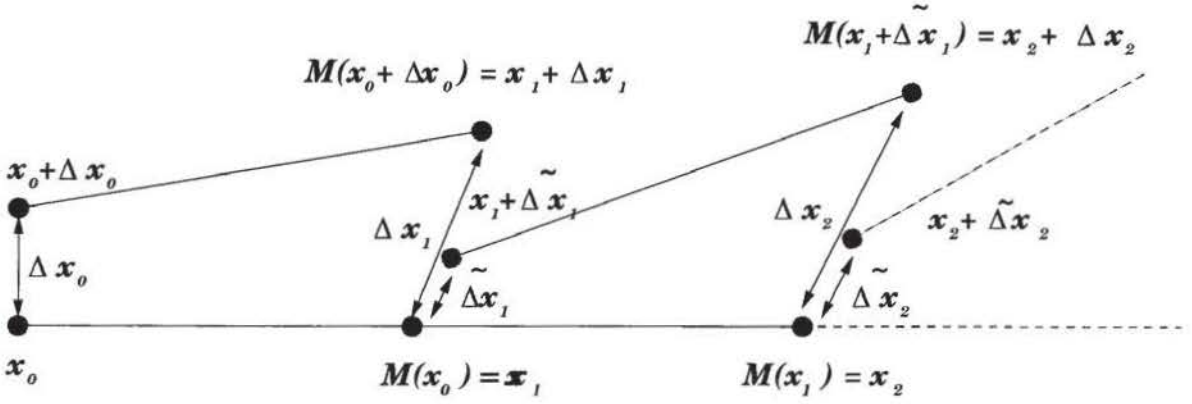

Fig. 3.5 (b) Expanding flow with normalisation

Figure 3.5: The figures show explanations of methods for the calculation of the Lyapunov exponent with and without the normalisation. The distance Δx_i in case (a) is taken as the Lyapunov exponent without normalisation, whilst in (b) the distance $\tilde{\Delta x_i}$ allows the distance between successive image points to be compared.

By examining the Lyapunov exponent we can determine areas where the mixing is

best. The definition of the Lyapunov Exponent (LE) is given as

$$\lambda_{LE} = \lim_{t\to\infty} \frac{1}{t} \ln \left(\frac{\| \delta \mathbf{x}(t) \|}{\| \delta \mathbf{x}(0) \|} \right),$$

where $\delta \mathbf{x}$ is the deviation from an orbit of the system. We often call this the infinite time LE, see Eckhardt & Yao (1993). It is not always the best to use in practical circumstances because we will be more interested in how the fluid mixes over a shorter time scale due to biological implications, as previously mentioned. For this purpose we define the finite time LE as

$$\lambda_{LLE}(\mathbf{x}_0, t) = \frac{1}{t} \ln \left(\frac{\| \delta \mathbf{x}(t) \|}{\| \delta \mathbf{x}(0) \|} \right),$$

which is also known as the local Lyapunov Exponent (LLE). We define $\mathbf{x}_0$ as the initial point of a trajectory and $\delta \mathbf{x}$ as the divergence of a nearby orbit from this trajectory.

In the same way the LE gave the average rate of stretching of the fluid over an infinite time, the LLE gives the average rate of stretching after a time t. The LLE depends on both space and time. This is also the case with the LE but the LE becomes independent of the initial conditions in ergodic regions. The ergodicity of a system describes whether it has many or few regular trajectories. A fully ergodic system is one with no regular trajectories. These systems mix more easily because there are no set paths for the particles to follow. Therefore the chaotic regions are fully connected. Further details of ergodicity are found in Guckenheimer & Holmes (1983) and Lichtenberg & Lieberman (1983). As mentioned, divergence of the initial conditions is the quantity the LE allow one to measure to determine the integrability of the system. Most importantly, if the initial conditions diverge rapidly, then the system can be characterised as chaotic. Hence in systems where there is no divergence, i.e. the LE is zero, we have an integrable system. From Ottino (1989), we know that chaotic systems have at least one positive LE and hence an integrable system cannot be chaotic. Therefore, in integrable regions there is no mixing because there are no connected chaotic regions. We can describe the points in the system by saying that they are limited by the torus which they are moving around.

By using the colour graphic capabilities of MatLab, we are able to represent the LE's in the areas around the fixed points and stokeslets. This means we see regions of high mixing as areas of lighter colours, whilst fixed points of the map remain very dark with the particular colour map we are using. These dark regions are the areas points will move away from last of all so that any mixing in these areas is at a minimum. In flows, regions of high or low stretching are related to the mixing of the phase space. This is a property which is also said to be true of maps.

We include two figures illustrating LE, Figures 3.6 (a) and (b), for vertically displaced and horizontally displaced stokeslets respectively. Notice we only show one quadrant of the plane due to the axisymmetry of the problem and the large amount of computing time taken to generate the graphs. We can assume the same patterns would be shown for the negative quadrant where the results for the region $r > 0$ would be simply reflected in the z-axis. For both vertically and horizontally displaced stokeslets, we observe in the neighbourhood of the central fixed point very little stretching (depicted by the dark colour). We also notice the 'stripes' evident in both figures above the region of the vortex core. These areas are regions of alternating low and high stretching. This would suggest a region where mixing is being stimulated.

Along with the LLE, another measure we could investigate is the geometry of stable foliation lines (s-lines), Tang & Boozer (1996). These s-lines indicate where rapid diffusive transport will occur through the LLE. Tang & Boozer (1996) find that diffusion is impeded if the LLE are small along the s-lines. This is illustrated diagrammatically as a sharp bend in the s-line corresponding to a dip in the LLE. More importantly, these sharp bends indicate barriers to diffusion. Comparisons of the LLE and s-lines are given in Otto et al. (2001), and illustrate how the s-lines correspond to small LLE. They explain why the 'striped' patterns we see in Figures 3.6 seem to suggest alternating high and low regions of mixing.

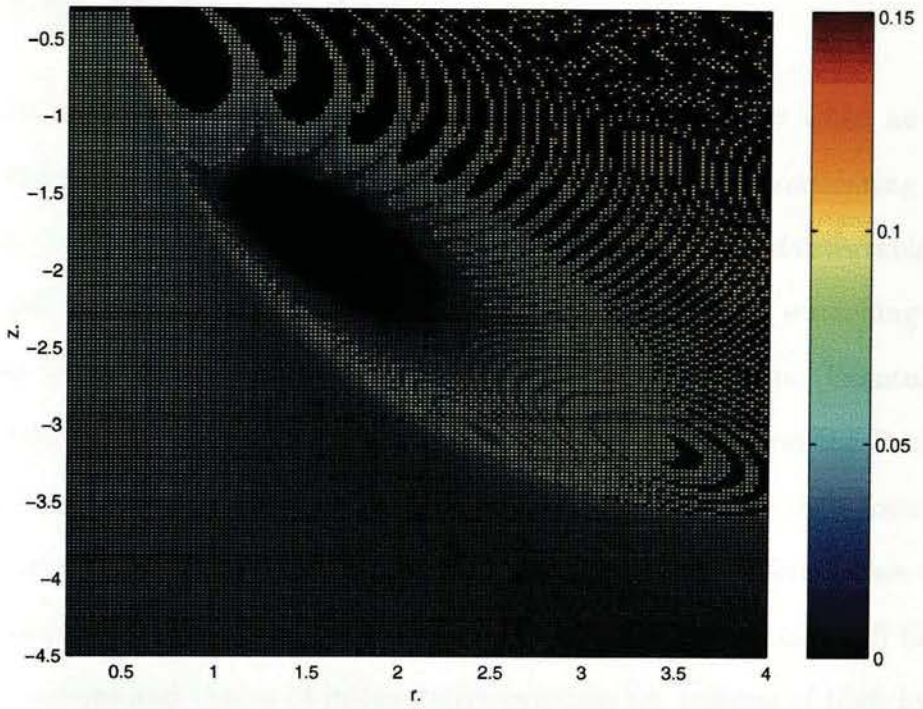

Fig. 3.6 (a) Vertically displaced stokeslets. Here $\alpha = 1.1$ and $\theta = 10^6$ with the stokeslets positioned at $(0, -1 \pm 0.5)$.

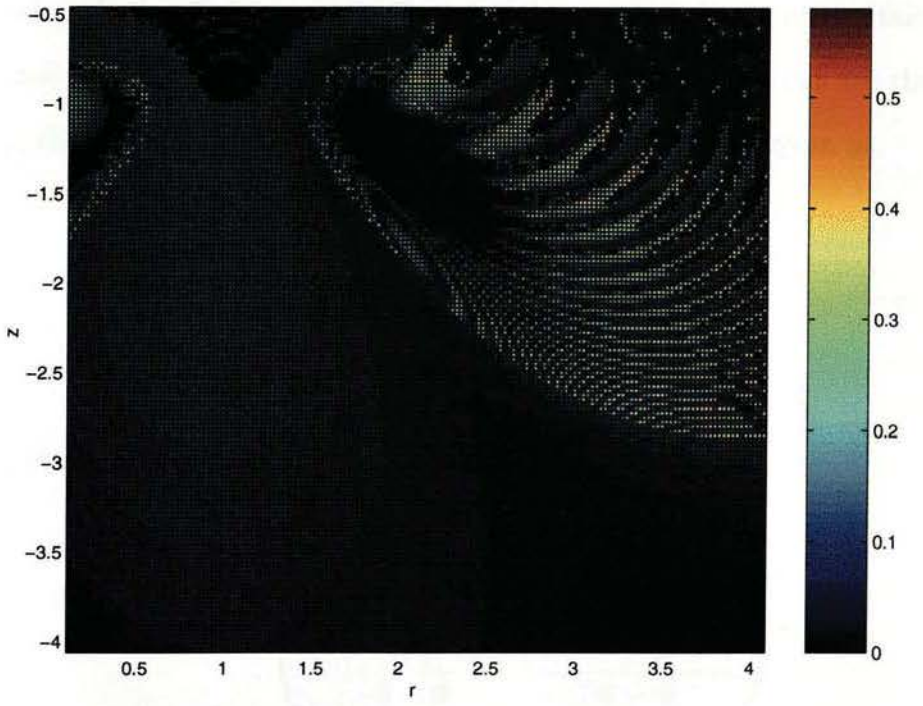

Fig. 3.6 (b) Horizontally displaced stokeslets. Here $\alpha = 1.1$ and $\theta = 10^6$ with stokeslets positioned at $(\pm 1, -1)$.

Figure 3.6: The figures show the Lyapunov exponents (LE) for different alignments of the stokeslets with the colour bars indicating the value of the LE.

3.3 The Hénon index

The Hénon index, mentioned previously in section 3.1, indicates when an elliptic point becomes hyperbolic (see Hénon (1969)). This is important when considering the transition into chaos. As we move closer towards a chaotic system, the area of integrable points found around each elliptic point becomes smaller. This is due to the stretching occurring on the system which removes points from between the elliptic points. Eventually there are very few regions of integrability that can be found or observed on the Poincaré section. These regions tend not to have the central elliptic fixed point as their focus and so have no set pattern to their dispersion around the plane. This is a different case to that which has a central elliptic point because in this type of situation we can still find both non-integrable regions and chains of integrability existing, i.e. regions of both hyperbolic and elliptic points. As mentioned in section 3.1 these are indicated by island chains shown on Poincaré sections, such as those in Figure 3.4 (c).

Examining the implicit map introduced in section 2.3, there are certain features we are interested in. By considering the Jacobian, $\mathbf{J}$, of this map, we can see the map is area preserving, that is $\det(\mathbf{J}) = 1$. The definition of the Jacobian is given as

$$\mathbf{J} = \begin{pmatrix} \dfrac{\partial \eta'_{n+1}}{\partial \eta'_n} & \dfrac{\partial \eta'_{n+1}}{\partial z'_n} \\ \dfrac{\partial z'_{n+1}}{\partial \eta'_n} & \dfrac{\partial z'_{n+1}}{\partial z'_n} \end{pmatrix}.$$

Therefore, the Jacobian of the map R_1 is given by

$$\mathbf{J}_{R_1} = \begin{pmatrix} \dfrac{4(1+\psi_{\eta z})+\Phi}{4-\Phi} & \dfrac{4\psi_{zz}}{4-\Phi} \\ -\dfrac{4\psi_{\eta\eta}}{4-\Phi} & \dfrac{4(1-\psi_{\eta z})+\Phi}{4-\Phi} \end{pmatrix},$$

where we have defined $\Phi = \psi_{\eta z}^2 - \psi_{\eta\eta}\psi_{zz}$, and all the terms are evaluated at $(\eta'_{n+\frac{1}{2}}, z'_{n+\frac{1}{2}})$. Notice that this is the Jacobian for the map R_1 (denoted by the subscript R_1), and not the whole map, M.

By considering the Jacobian of the map we can easily determine the condition which will indicate where the bifurcation value of α occurs, i.e. when the central elliptic point becomes hyperbolic. We know for an area-preserving map the determinant of the Jacobian is unity (as above $\det(\mathbf{J}) = 1$). Also, we know the determinant of the Jacobian is equal to the product of its eigenvalues such that

$$\lambda_1 \lambda_2 = 1,$$

where λ_1 and λ_2 are the eigenvalues. If $\lambda_1, \lambda_2 \in \mathbb{R}$ then the local action of the map is one of stretching and contraction since

$$\lambda_1 = \lambda_r \quad \Rightarrow \quad \lambda_2 = \frac{1}{\lambda_r},$$

for $\lambda_r \in \mathbb{R}$. If $\lambda_1, \lambda_2 \in \mathbb{C}$ then

$$\lambda_1 = \lambda_i \quad \Rightarrow \quad \lambda_2 = \lambda_i^*,$$

where λ_i^* is the complex conjugate of λ_i and $|\lambda_i|^2 = 1$; both λ_i and λ_i^* lie on the unit circle.

Now if we determine the characteristic equation for the Jacobian we have

$$\lambda^2 - \mathrm{tr}[\mathbf{J}]\lambda + \det(\mathbf{J}) = 0,$$

where $\mathrm{tr}[\mathbf{J}] \equiv \mathrm{trace}[\mathbf{J}]$ and is defined as the sum of the eigenvalues. Since we know that in this case $\det(\mathbf{J}) = 1$, then the solution to the characteristic equation is given by

$$\lambda = \frac{1}{2}\left\{\mathrm{tr}[\mathbf{J}] \pm \sqrt{(\mathrm{tr}[\mathbf{J}]^2 - 4)}\right\}.$$

To determine whether or not the eigenvalues are real or complex depends on the discriminant and hence on the value of $\mathrm{tr}[\mathbf{J}]$. When $|\mathrm{tr}[\mathbf{J}]| < 2$, the eigenvalues are

complex and so the effect of the map is a rotation, as associated with elliptic points. There is a rotation because the eigenvalues have to occur in complex conjugate pairs and hence lie on a circle. When $|\mathrm{tr}[\mathbf{J}]| > 2$, the eigenvalues are real and associated with hyperbolic points. Due to the relationship between real eigenvalues, one value must represent a stretching and the other a compression in the directions corresponding to their eigenvectors.

In order to determine the structure of the fixed points defined in section 3.1, it is first necessary to locate these points. We construct a simple routine which effects the calculation

$$\mathbf{x}_n \overset{M^j}{\longrightarrow} \mathbf{x}_{n+j}.$$

This operation is implicit, involving the use of two-dimensional Newton-Raphson iteration, and the routine is called j-times. We further exploit a two-dimensional iteration to determine values of $\mathbf{x}_n$ such that

$$\mathbf{x}_n = \mathbf{x}_{n+j},$$

thereby determining points of period j. We can use this calculation to determine bifurcation values for both the vertically and the horizontally displaced stokeslets. As a representation of the type of results this generates, Figure 3.10 illustrates results for the horizontally displaced case when $j = 1$, that is fixed points. Associated with these fixed points we can construct the idea of linear stability allied to the consideration of the local Jacobian.

We can present results which indicate how varying the parameters of different implicit maps for horizontally and vertically displaced stokeslets yields information relating to the bifurcation value. Figure 3.7 shows how, for various values of θ, we have obtained the value of α at which the fixed point makes the transition from being elliptic (rotational) to hyperbolic (stretching). Figure 3.7 is for the case of vertically displaced stokeslets with (a) giving the values of α relating to r and (b) giving the values for z. We can see the lines converging to one fixed line once θ becomes large, i.e. above $\theta = 10^3$ for both r and z. For

this map one knows for any chosen value of θ, then any value of α above the corresponding bifurcation value relevant to θ will give chaotic mixing in the fluid flow. For example, from Figure 3.7 by taking $\theta = 10^6$, one infers when α is greater than 4.4 the central point will have bifurcated. The graphs allow the positions of the r and z coordinates to be recorded both before and after bifurcation by examining the corresponding values on the vertical axes. In this example for $\theta = 10^6$, the central point is located at approximately $(0.965, -1.754)$ when the map bifurcates.

Using the same methods described above, one can look for bifurcation values of α when the stokeslets are horizontally displaced. This provides data for comparison between the two types of stokeslet orientation. The details of the results are found in Figure 3.8 (which includes more detail than the previous figure for the vertically displaced case). We found there is a difference between the type of implicit map one uses and the corresponding fixed point determined from each map. To demonstrate this we have plotted the different types of map (implicit in either r or z) for $\theta = 10^6$ and on both plots have stated the value of α where bifurcation occurs, i.e. the value at the transition when the magnitude of the Hénon index becomes greater than two. Notice the graphs indicate a previously mentioned feature involving the composition of the map when one takes an intermediate point, the $(n + \frac{1}{2})^{\text{th}}$ point, to find the final point in the n^{th} map, refer to section 2.3. The graphs show the 'half-way map' which we have interpreted as giving the fixed points for the particular case of the $(n + \frac{1}{2})^{\text{th}}$ operation of map. The graphs show the different fixed values for these points both for the full and half-map along with their corresponding bifurcation values (which are obviously the same values given for the full map).

The last two figures in this section show a concise way to determine the bifurcation values of α for any given value of θ. Whereas before we were required to plot specific values of θ to find the corresponding value of α, we can use the graphs in Figures 3.9 and 3.10 for any θ. It is obvious that the value for α above which the system is always chaotic for large enough θ is given by the vertical sections in each graph. In Figure 3.9 we have the bifurcation value $\alpha = 4.4$ when two stokeslets are vertically displaced (we only considered

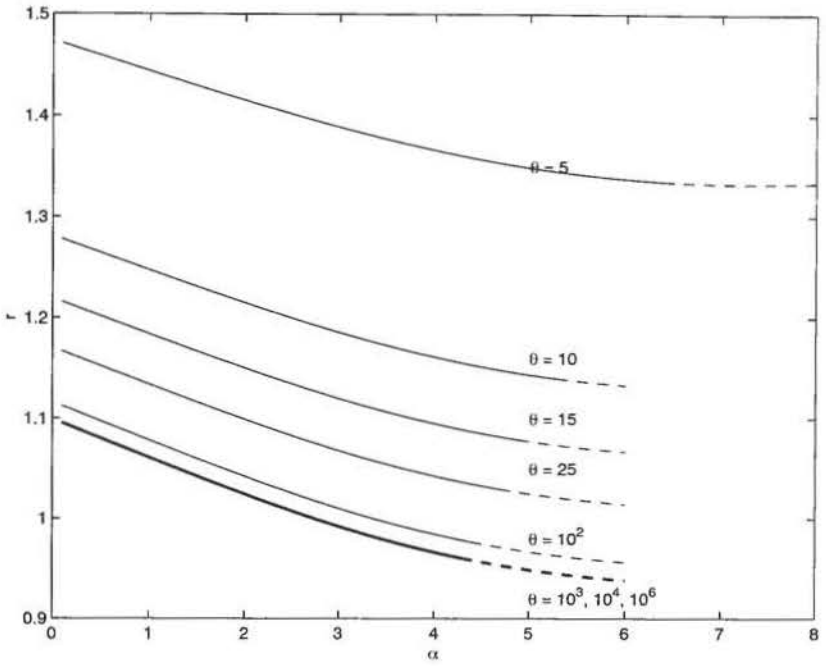

Fig. 3.7 (a) (α, r)

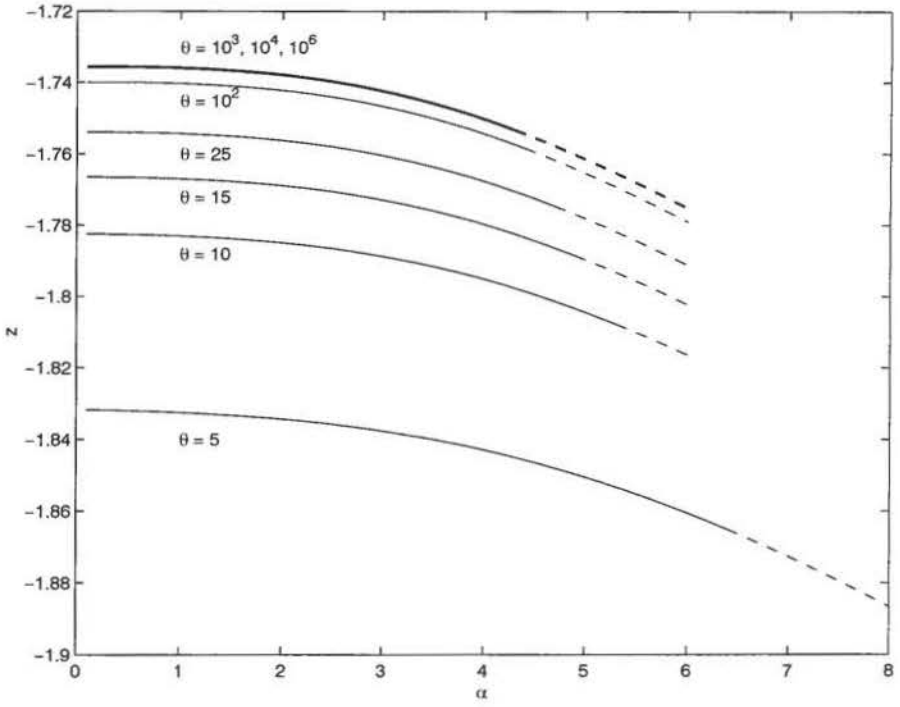

Fig. 3.7 (b) (α, z)

Figure 3.7: The graphs show how the fixed points change for different values of θ. The dashed line indicates where the central fixed point is hyperbolic. The stokeslets are vertically displaced here.

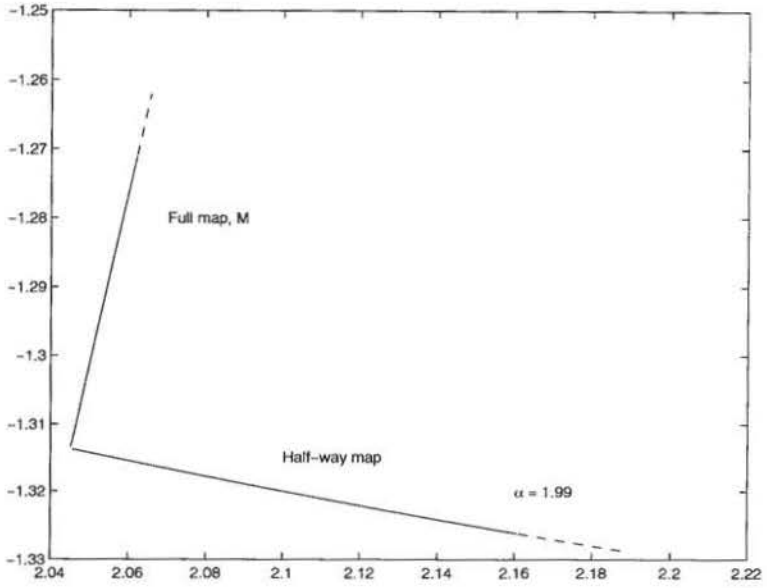

Fig. 3.8 (a) The implicit z map.

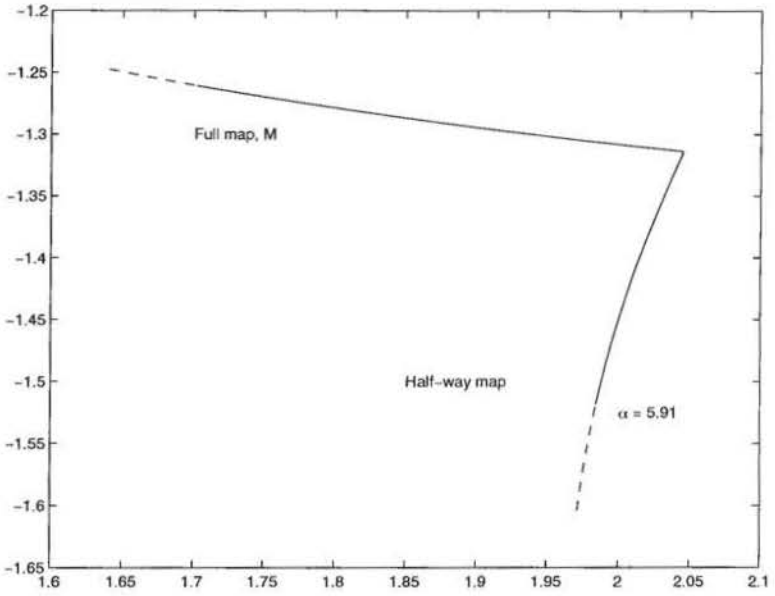

Fig. 3.8 (b) The implicit r map.

Figure 3.8: The graphs show how the fixed points change for $\theta = 10^6$ within the $r - z$ plane. The dashed line indicates where the fixed point is hyperbolic. The stokeslets are horizontally displaced here. Notice that the scales are different between subfigures.

one type of map in this case). For any greater value of α, the map will always bifurcate for all θ. Similarly, we construct a graph illustrating the bifurcation values of α for two

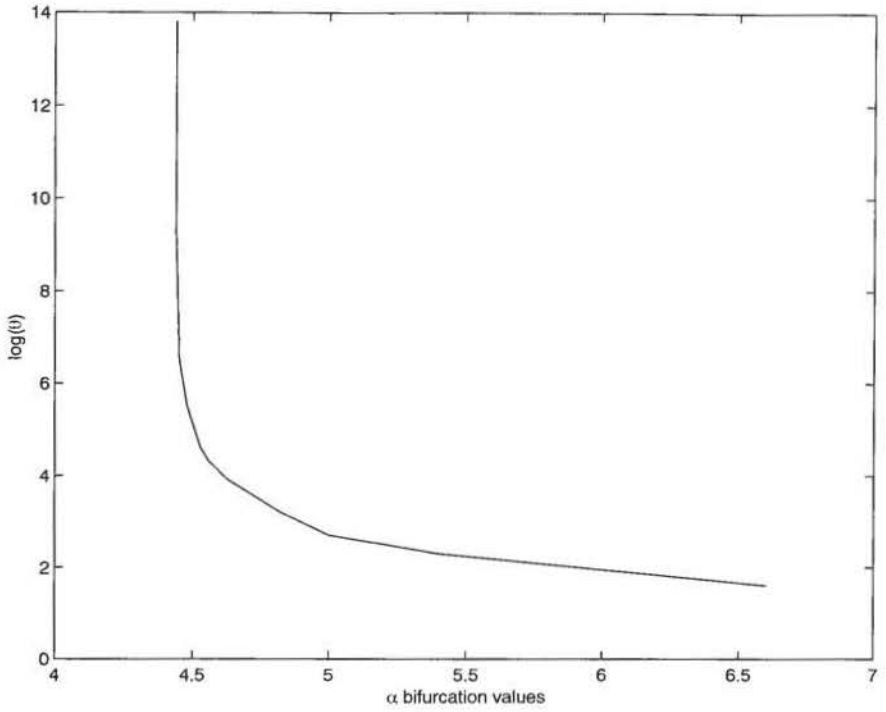

Figure 3.9: The graph shows the bifurcation value of α against the logarithmic value of θ for two vertically displaced stokeslets. This allows one to find the bifurcation value for any given θ.

horizontally displaced stokeslets as in Figure 3.10 (where we have included bifurcation plots for each of the three maps considered). Comparing the bifurcation values, we found the value of α for the horizontally displaced stokeslets using the implicit z map is closest to that found for the vertically displaced stokeslet case.

3.4 Statistical techniques and dispersion

As well as characterising how well the points stretch and rotate away from the fixed points, we are able to use statistical variance to determine the amount of spreading which acts on them. Taking a tight grid of a hundred regularly spaced points, we can perform the map on them simultaneously and then after each iteration compare the amount of spreading which has occurred. This dispersion or spreading of the points will be due to the dynamics of the system because the map we use is area preserving. We are going to consider this dispersion as being due to diffusion. Although the model of the physical

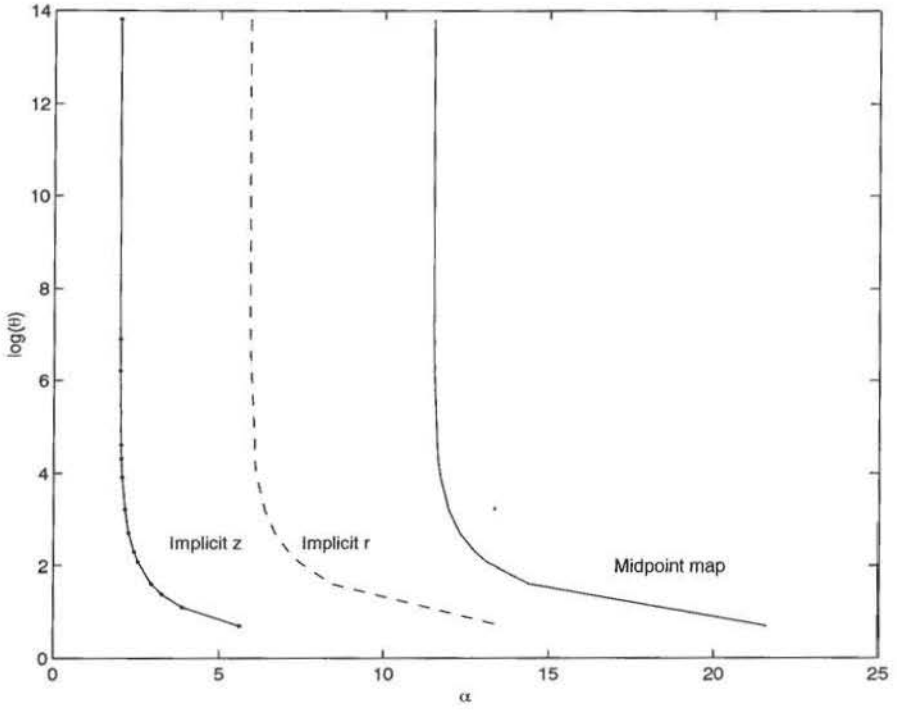

Figure 3.10: The graph shows the bifurcation value of α against the logarithmic value of θ for two horizontally displaced stokeslets. This allows one to find the bifurcation value for any given θ. The graph shows the different maps used, each appropriately labelled on the graph.

system does not involve diffusion (as an assumption) we can examine what effect the flagellum would have on the weak diffusion of the particles if it were present. We assume in a system where there is no flow of fluid (other than flow created due to the beating flagellum), that with each iteration of the map the particles in a fixed area will disperse proportional to the iteration of the map. This is standard diffusion when there are no external factors affecting the movement of the particles.

The particular method we use is taken from Otto et al. (2001). We start by considering the mean position of the grid of points in terms of the individual coordinate directions given by r and z. The statistical techniques used will then involve examing the variance of the positions of the coordinates that constitute the grid. The grid of particles is advected with the flow and the following calculations are made:

$$\sigma_{rr} =< r_n^2 > - < r_n >^2 \quad \text{and} \quad \sigma_{zz} =< z_n^2 > - < z_n >^2 .$$

These are the variances in the r and z directions respectively after n iterations of the map. In each case we would expect the variance to obey a simple power law. The index of this power is said to be representative of the level of diffusion; for powers less than one the system is said to be subdiffusive and superdiffusive for those greater than one. In the above equations, the symbol $< . >$ is taken to be the mean of the quantity over all the points in the block. Hence we use logarithms to determine the effective diffusions, such that

$$\sigma_{rr} \sim n^{\beta_r} \quad \text{and} \quad \sigma_{zz} \sim n^{\beta_z}.$$

It is also possible to calculate the covariance σ_{rz}, although in this case enough information can be gleaned using the variances. By determining the parameters β_r and β_z we will be able to tell if the amount of dispersion of the system can be classified. The case we explained initially where one has the 'standard diffusion' behaviour of the system (no external factors affecting the dispersion) will have $\beta_r = \beta_z = 1$. This shows the diffusion is dependent on the number of iterations of the map only, i.e. n. We can therefore take

the value of β as a standard against which varying degrees of diffusion can be classified. Figure 3.11 shows various values of β depending on the different values of α and θ used for each map. A subdiffusive map shows where the diffusion is confined so there is very little mixing. A superdiffusive map occurs when the diffusion is much larger and causes the points to diverge from the initial conditions very quickly. These are intuitive definitions when we consider $\beta = 1$ representing the standard dispersion of particles due to only diffusion acting.

Figure 3.11 shows different cases of the map for varying values of the parameters. When we have a small value of α and a large value of θ, as in Figure 3.11 (a), we can observe subdiffusion. This is even more marked when α is increased further as in Figure 3.11 (b). Both graphs show subdiffusion in both the r and z directions because the value of β is less than one. This indicates a system where the values of the parameters for viscosity and force cause the particles to become less well dispersed due to diffusion than we would see in the standard case. The system of particles would show better chaotic dispersion without the action of the flagellum in both these cases.

In the final figure, Figure 3.11 (c), for larger α and smaller θ we observe values of β_r in the superdiffusive range. This indicates for these parameters we now have greater diffusion within the system than would otherwise occur without the force on the standard system. The parameter α indicates either a large strength of force or a longer time between the stokeslets pulsing could provide this greater level of diffusion.

These results give a more realistic impression of what is happening to the particles when diffusion is present. By developing a larger dispersion of particles, one can assume the environment within which the organism is situated is more favourable to prey particle uptake. The increase in feeding ability may come from a greater mix of particles around the organism and hence higher contact rates increasing the likelihood of interception. The results enable one to see the effects which the strength of the force and ratio of viscosities will have on the diffusion of the tracers. The greater the diffusion, the larger the opportunity for mixing to occur in the system because particles will be diverging as

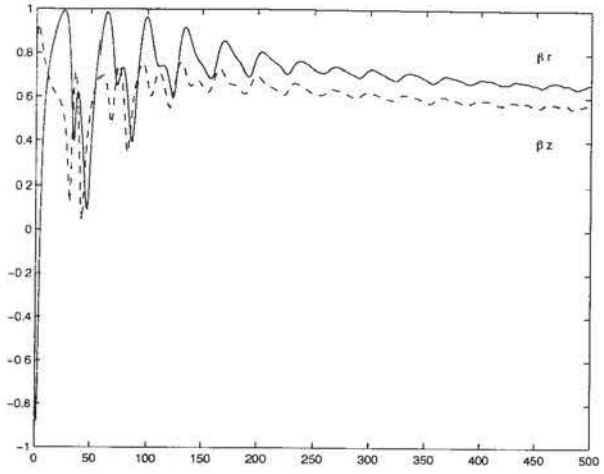

Fig. 3.11 (a) $\alpha = 0.5, \theta = 10^6$.

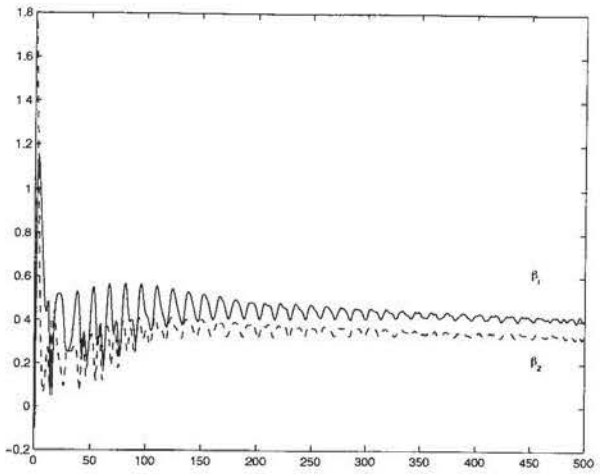

Fig. 3.11 (b) $\alpha = 1.1, \theta = 10^6$.

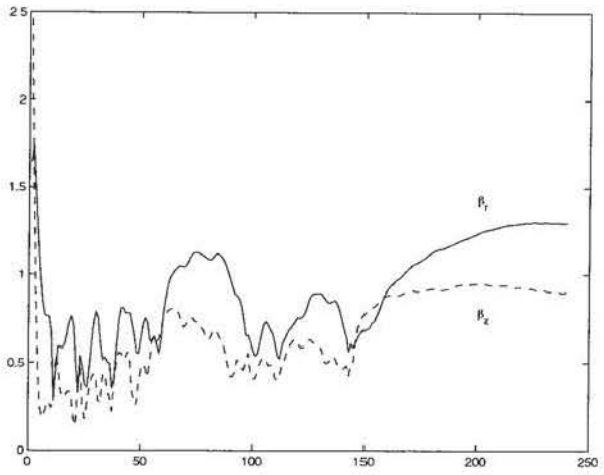

Fig. 3.11 (c) $\alpha = 1.7, \theta = 10$.

Figure 3.11: Figures illustrating the values of β_r and β_z for different θ and α. The horizontal axis indicates the time scale over which the flow has evolved and the vertical axis gives values of β_r and β_z. They allow identification of subdiffusive or superdiffusive cases for two horizontally displaced stokeslets.

opposed to remaining equidistance from one another.

The model can also be modified to account for the diffusion which can be present in such a system. Rather than solving both the problem of the advecting fluid alongside that of diffusion, we can incorporate white noise into the advection problem. The white noise represents the motion the particles could experience due to molecular diffusion and

it can be shown that this is equivalent to solving a diffusion-advection equation (and can be thought of as a Wiener process). A full and detailed description of the results can be found in Otto et al. (2001) and the references contained therein. The white noise terms take the form of identically distributed Gaussian variables with the amplitude equal to 0.01 which represents the inclusion of noise.

The three cases where we have calculated the diffusion in Figure 3.11 can be compared to the cases in Figure 3.12 which now include the white noise term. Unsurprisingly, the addition of white noise significantly increases the levels of diffusion. The values of both β_r and β_z are higher especially in Figure 3.12 (b) (compared to Figure 3.11 (b)) where the system becomes superdiffusive as opposed to only subdiffusive without the inclusion of noise (or with only natural diffusion).

3.5 Summary

This chapter has developed the use of methods enabling investigation into the degree of mixing one can witness in the axisymmetric problem. Mixing can be observed to be improved when forces and time steps are increased, which is verified by the use of Poincaré sections, Lyapunov exponents and measures of statistical dispersion. These results all complement one another showing agreement amongst themselves. One notes that the measures we have used within this chapter are limited, but allow progression to the more complex case of analysing the problem of a fully three-dimensional model with its associated flow field.

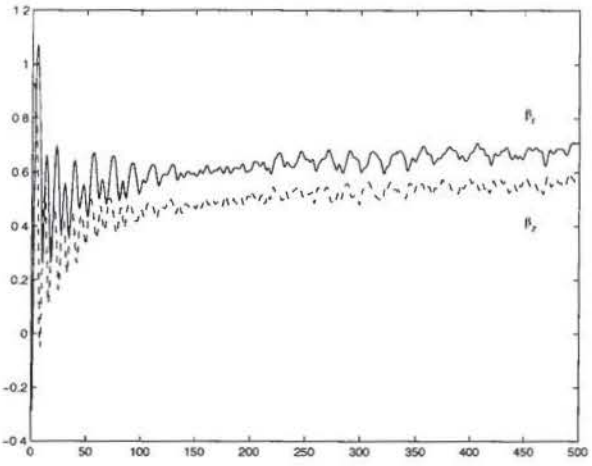

Fig. 3.12 (a) $\alpha = 0.5, \theta = 10^6$.

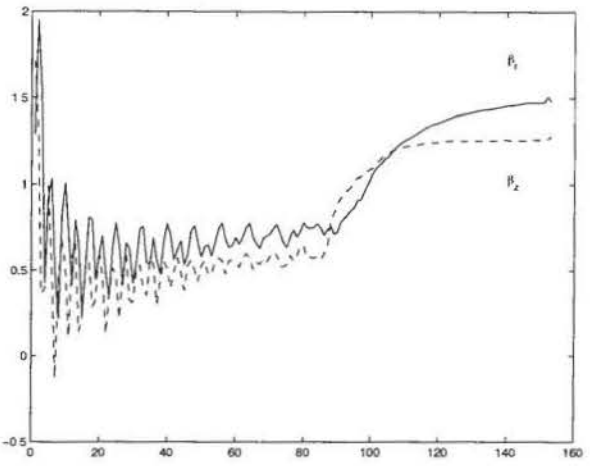

Fig. 3.12 (b) $\alpha = 1.1, \theta = 10^6$.

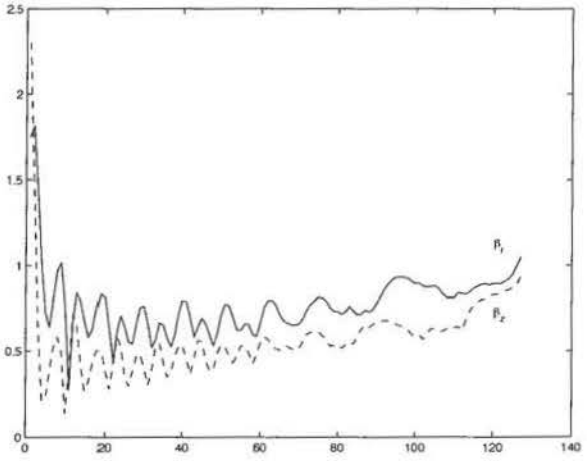

Fig. 3.12 (c) $\alpha = 1.7, \theta = 10$.

Figure 3.12: Figures illustrating the values of β_r and β_z for different θ and α with the addition of white noise at an amplitude of 0.01. The horizontal axis indicates the time scale over which the flow has evolved and the vertical axis gives values of β_r and β_z. Again identification of subdiffusive or superdiffusive cases can be made for two horizontally displaced stokeslets. Comparison with Figure 3.11 shows increased diffusion with the addition of noise.

Chapter 4

MOTIVATION FOR A THREE-DIMENSIONAL MODEL DUE TO APPLICATIONS OF FEEDING AND MIXING IN BIOLOGY

In a step towards looking in greater detail at a three-dimensional representation of the organism which motivates this study, we investigate the manner with which individual particles are mixed within three-dimensional space. The intermediate model presented within this chapter retains features from the horizontally displaced case of two blinking stokeslets (to represent the action of the flagellum) whilst the other features of the organism are neglected. Considering three-dimensional space will allow particles to be tracked in their movement around the organism due to non-axisymmetric properties. The previous chapter considered the motion of an inert particle or tracer due to horizontally (and to some extent vertically) displaced stokeslets. Using an axisymmetric coordinate system allowed tracers to be followed over a certain time period, creating an understanding of the mixing properties in the plane containing the stokeslets for various sets of parameters. The work presented within this chapter extends this theme.

This chapter considers previous work by various others from the fields of microbiology, biofluiddynamics and mathematics, researching the specific mechanics of micro-organism motion, see section 4.1. This stimulates the study of the biological features of SA which ultimately motivate the study within this thesis. To satisfy the requirements of the physical

system, we introduce methods taken from research by Pettitt (2000) and various considerations required to replicate a simplistic model of the organism in three dimensions. Experimental data and measurements are given for the specific problem with which we are concerned, to illustrate some of the important features of the subject matter. Agreement of our results with these experiments will require an understanding of a number of processes which occur in the physical system. Presenting a brief synopsis of these processes will allow material contained within later chapters to be considered in the correct context.

Although this chapter considers the motivation for studying a fully three-dimensional case, we start by presenting details of changing the axisymmetric problem into a three dimensional one to corroborate the earlier studies of horizontally displaced stokeslets. We could examine both horizontally or vertically displaced stokeslets although we concentrate on the first case here. Numerical representations of particle paths will show how varying the stokeslet position can affect the flow field, see section 4.3. We will validate the axisymmetric case presenting comparable Poincaré sections generated from the numerics for the three-dimensional case.

4.1 Motivation for studying a three-dimensional model

There are many biological entities which employ flagellar and cilia mechanics for a range of different purposes. Two of the common reasons are propulsion and feeding, both of which have been studied widely by biologists and mathematicians alike.

Early work by Oseen (1927) investigated Green's functions representing a stokeslet's interaction with a plane. This was then built on by Blake (1971), Sleigh (1973) and Lighthill (1976), to name a few, furthering work specifically considering stokeslets and their use for modelling a variety of different biological flow fields. Studies into the shape of the flagellum and how its beat affects the flow have been studied in the original work of Taylor (1951) and Hancock (1953) who analysed the motion associated with swimming

Flagellar radius	Flagella length	Cell Body diameter	Flagellar Base height	Rigidity of stalk
Radius of CA	CA	C	OC	Sway in OC
0.4	7.9	4.5	17.5	0.4
0.4	6.4	4.3	26.3	1.6
0.4	8.1	5.2	17.9	1.9
0.4	8.3	2.7	20.2	0.4
0.4	10.8	4.3	17.9	0.8
0.4	9.3	4.8	30.0	0.8

Table 4.1: Measurements (in μm) taken from *Codosiga botrytis* showing the variation in size between a number of cells. Figure 4.1 gives details of the lettering with respect to the physical features of the organism. The data is taken from Pettitt (2000).

micro-organisms. This led to further work by Gray & Hancock (1955) who studied resistance coefficients and Appendix C discusses this method in greater detail. Although resistance coefficients do not directly contribute to the method used to finally model the organism, they can give approximate information about both the magnitude of the forces and the flow fields due to a beating flagellum.

The organism *Salpingoeca Amphoridium* (SA) filters nutrients through a collar composed of fine tentacles as introduced in section 1.5. It is appropriate to study work on filter feeding which has been specifically considered by Rubenstein & Koehl (1977), Higdon (1979*a*), Fenchel (1986), and Fulford & Blake (1995). The action of a flagellum beating has also been studied with regards to methods of locomotion (also applicable to cilia) by Higdon (1979*c*) and Ramia et al. (1993). Although the organism studied is sessile, it is possible to study various features of the forces around a motile organism to enhance our understanding of the flow fields. This thesis draws on many common features from the above mentioned papers along with other similar studies.

Typical dimensions of the choanoflagellates which we study are given in Table 4.1 where the lengths correspond to the positions indicated in Figure 4.1. By beating the flagellum in what we assume to be a helical motion (although Lighthill (1996) also reviewed planar waves), the flagellum creates currents in the flow which move both the fluid and particles within it. These particles can be considered to be nutrients for the organism and

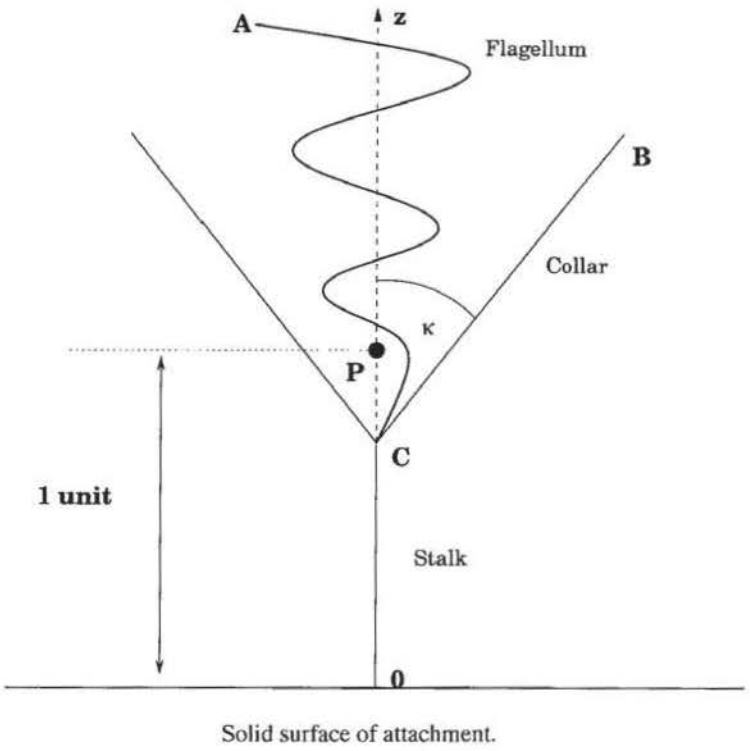

Figure 4.1: A simplified two-dimensional model of the organism showing its stalk, collar and flagellum. Table 4.1 gives an indication of the dimensions of a typical organism with reference to the features shown in the illustration.

include bacteria and prokaryotic cells on which the organism will feed. As the particles move around and through the collar, the organism is able to filter the fluid and possibly capture its nutrient source for ingestion.

The method of capture at the mouth and the ingestion process have relatively little known about them. We do know that particles are 'eaten' because from experimental results provided in Pettitt (2000), certain tracers will not reappear again once they have moved into the organism's mouth area. Work by Berg & Purcell (1977), Rubenstein & Koehl (1977) and more recently Shimeta & Jumars (1991) look from a more biological than mathematical view point at the way in which particles are captured by filters.

The work by Berg & Purcell (1977) considers how particles adhere to the surface of a cell which are the filaments of the collar in our study. They consider, in a statistical manner, how likely receptors are to absorb a number of specific particles which they are intended to capture. Their work moves on to investigate whether the movement of the

organism affects the intake of particles. The methods they use which are applicable to our work consider whether a local stirring induced by the organism will increase the rate at which particles reach the receptors. This is similar to the way swimming organisms strive to achieve more contact between particles within the fluid by actually moving through it. Fixed organisms are trying to replicate this mixing by forcing the fluid to move around their cell body because they do not have the ability to move through the fluid themselves. In addition, Berg & Purcell (1977) look at the concentration of particles around the cell and the chemical gradients the cell can create to induce greater absorption. These are factors which show the simplicity of our model because these effects are not included within the model we choose to develop.

The work by Rubenstein & Koehl (1977) follows a more mathematical path to model the interception and capture of particles than Berg & Purcell (1977). The work is mainly concerned with direct interception but other methods are discussed which relate to particle capture. These methods involve considering the density of particles incorporated within the flow, the gravitational forces acting on the particles and the usual Brownian motion (i.e. particle diffusion). By developing encounter rates based on the model of flow past a cylinder, they determine for a given set of conditions (or parameters of the system) the method which will produce the highest capture rate, and hence be most beneficial to the organism for any given conditions. The model used in their paper is appropriate to our feeding organism because it considers the pattern of flow around a cylindrical collector. It is possible that one could model each micro-villus as a cylinder, but this investigation is left for later collaborative work.

An important feature of the environment within which SA lives is the rigid boundary. This is where we will introduce the differences to the model we go on to describe and utilise compared to other previous work examining motile organisms. Earlier work has mainly concentrated on considering an infinite fluid around such an organism. Introducing a rigid boundary would mean the flow will now be constrained somewhat. As with the previous axisymmetric work, the flow is in the low Reynolds number régime due to the dimensions

being very small and viscosity being large. As mentioned in the introduction, the typical Reynolds numbers for these types of flows are 10^{-2} to 10^{-6} for various environments.

By first modelling the organism with an axisymmetric model, we considered how chaos may appear in the flow patterns around the choanoflagellates which are being studied. In theory, in an axisymmetric flow which is area preserving, we do not get any significant mixing of the fluid. This is because the stream lines are closed and particles following particular stream lines will only be able to stay on that specific path unless the trajectories become crossed and tangled as mentioned in Chapters 2 and 3. This is not beneficial to an organism who feeds using filtering as it will mean there will be a relatively small amount of new particulate matter to filter each time the fluid moves through the collar. By introducing an element of irregularity in the form of chaos into the feeding patterns, it will enable the stream lines to become irregular so the trajectories are no longer continuous therefore destroying the eddy structure due to intersecting stream lines. These resulting scattered patterns should then bring more fluid into contact with the collar and mouth than would otherwise reach it if it were only being fed by fixed stream lines. Hence, more particulate matter will also come in to contact with the collar enabling improved capture and eventually feeding by the organism. As the cited works indicate, the ability to study this organism within three dimensions would enhance the investigation of mixing around the organism. Therefore, we now progress within the next two sections to study first an augmentation of the axisymmetric model, followed second by particle paths in three-dimensional space.

4.2 Comparison of particles on and off the plane containing the stokeslets

To progress from the work which has been previously studied in both biological and mathematical research, there is an intermediate stage we consider to aid the progression of this thesis. Section 4.1 has introduced some of the background to this work along

with the biological scenarios which are motivating this study. It is obvious that although the initial axisymmetric model introduced in Chapter 2 serves as a good approximation, there are significant improvements which can be made. We can begin by considering how a simple system of two horizontally aligned stokeslets influences the flow field in three-dimensional space. This can also provide confirmation of the axisymmetric work in the plane which has been previously presented in Chapter 3.

As introduced in section 1.6, it is possible to consider an approximation of a flagellum as a linear distribution of point forces along the central axis of a helix. This would create a larger area over which the effect of the force could be spread, therefore closely representing the true nature of the flagellum. Previous work, Liron & Blake (1981), has investigated this type of configuration. More recently, Pettitt et al. (2001) have generated flow patterns allowing comparisons with both the simpler case presented in Chapters 2 and 3, and the more detailed work to follow in Chapter 5. Flow patterns generated due to a linear force distribution show similarities with the stream functions illustrated in Figures 2.5 and 2.6. By considering the dimensions of the organism we investigate, the numerics can distribute the stokeslet force along a line to replicate the length of the flagellum. Good comparison is found between the eddies in experimental and theoretical investigations for all three organisms considered in Pettitt et al. (2001).

The three-dimensional case obviously involves adding another dimension to the model, creating more difficulties in the numerics and consequently in visualising the motion of the tracer. The model in three dimensions will be essential for any further advancement in our understanding of what happens within the real-life flow fields of the system. As before, the model consists of two stokeslets who lie a prescribed distance apart and are situated below the interface between two fluids. The extra dimension in the problem will now allow one to move the stokeslet positions off the plane in which they were situated in the axisymmetric case and vary their position with respect to one another into this third direction. We could then investigate what effect this has on the flow fields for various configurations of these stokeslets. For example, the stokeslets could be situated

at different heights giving one a more marked effect adjacent to the interface than the other. In this case we would see more mixing currents around the stokeslet which is situated closest to the interface whereas the eddies associated with the other stokeslet would appear to have a smaller effect on the overall flow field. Figure 4.2 shows this effect by considering two different stokeslet positions. The contours marked are the values of the stream functions at set intervals so that the flow field can be seen for the two different stokeslet configurations.

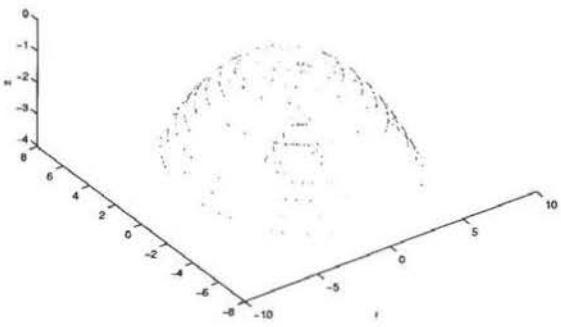

Fig. 4.2 (a) Two stokeslets positioned at (5,-2,-1) and (-5,-0.5,-1), both with $\alpha = 0.1$ and $\theta = 10^6$.

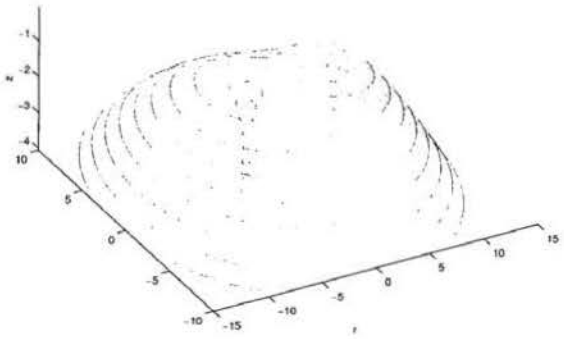

Fig. 4.2 (b) Two stokeslets positioned at (1,-1,-1) and (-1,-0.5,-1) with the same parameters as in Fig. 4.2 (a).

Figure 4.2: Figures generated using MatLab to illustrate the flow fields around two alternative stokeslet configurations. The contour lines represent stream functions evaluated at several positions along the z-axis and then superimposed onto one figure to recreate the overall flow field. Note the scale change between the two subfigures.

In this chapter, by initially investigating various arrangements of stokeslets, we can gain a better understanding of the effects of the flagellum when it is simply modelled by two horizontally displaced blinking stokeslets in three-dimensional space. This will be an improvement on the single point force representation in the axisymmetric system which may not be a very realistic model to study when we are required to consider the various directions the flagellum will act in due to its fully three-dimensional beat. The model we move on to investigate will involve integrating a distribution of point forces over the length of the flagellum. This will allow the force acting on the fluid to vary dependent

on the flagellum shape at any instant in time. Investigations into the interaction of the flagellum with both the cell body and plane are another area requiring consideration, but more details of this will be presented in Chapter 5.

It will be possible to change the tracers initial positions as well as varying where the stokeslets are acting within the three-dimensional model. In this simple three-dimensional model, a tracer can initially be situated off the plane the stokeslets lie in unlike the initial horizontally displaced stokeslet case. This will enable observations to be made indicating whether the plane of the stokeslets is attracting or repelling particles. This area of the study is pursued further in section 4.3 where particle paths are investigated. For this work, we consider the stokeslets to be horizontally displaced with their forces acting perpendicular to the interface.

To corroborate the results from Chapter 3 we define the three-dimensional model to recreate the $y - z$ plane by eliminating the third coordinate direction. By examining the variation between the coordinate systems, one can numerically construct stream lines within a 'plane' of the flow. Knowledge of stream lines will provide maps which can facilitate the tracking of particle positions over time. They can be used to begin comparisons of Poincaré sections for the two- and three-dimensional numerics. The Poincaré sections for the axisymmetric case are given previously in section 3.1 and we can reproduce the equivalent of these from the three-dimensional numerics once the third dimension is reduced to zero. A comparison will only be valid if we position the tracer within the same vertical plane as the horizontally displaced stokeslets. The three-dimensional problem can then be reduced to the initial case where we considered the interaction effects of the axisymmetrical nature associated with each individual stokeslet.

Figure 4.3 shows two Poincaré sections generated via the three-dimensional numerical code, using only stokeslets and a tracer situated within a single plane. Comparing these to figures from section 3.1 which have the same parameters for the problem, we see agreement between our results because the two-dimensional result for horizontally displaced stokeslets produces an identical result to the three-dimensional model. This is an impor-

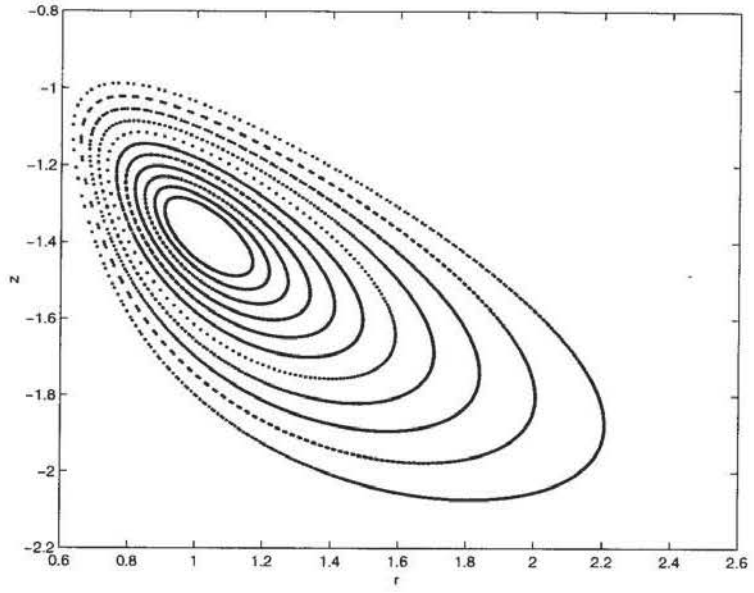

Fig. 4.3 (a) Stokeslets at $(\pm 0.5, -1)$ with $\theta = 10^6$ and $\alpha = 0.1$.

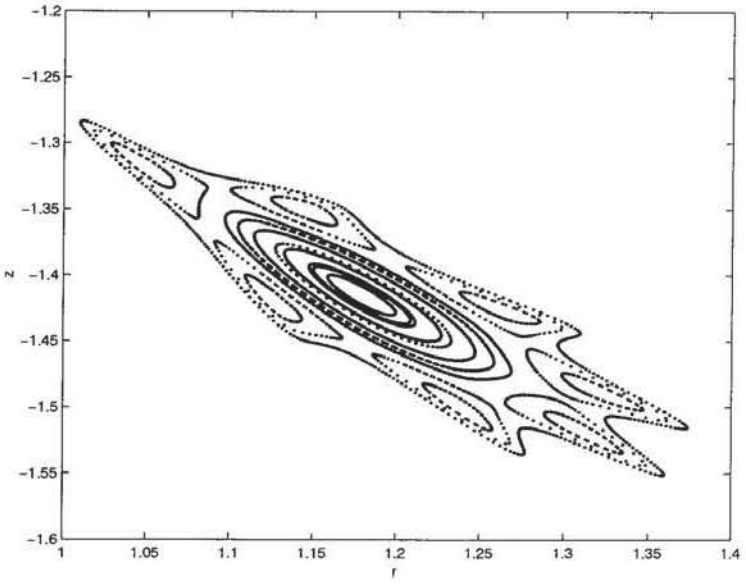

Fig. 4.3 (b) Stokeslets at $(\pm 0.5, -1)$ with $\theta = 10$ and $\alpha = 1.5$.

Figure 4.3: A Poincaré section generated using the three-dimensional numerics but showing specific two-dimensional cases. This should be compared with Figure 3.4.

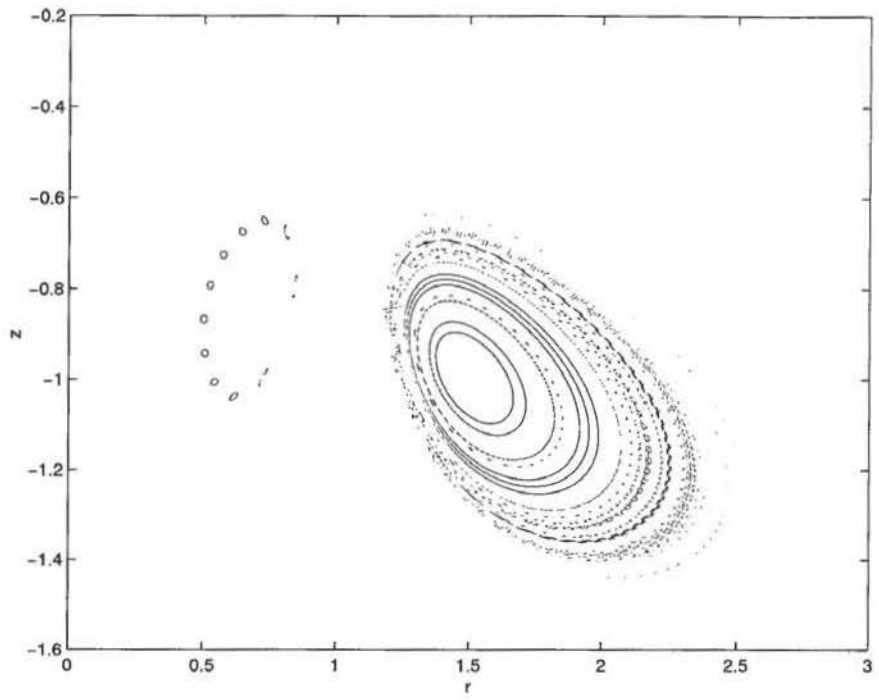

Figure 4.4: The horizontally displaced stokeslets positioned at $(0, \pm 1, -1)$ show how the internal eddy is visible on the Poincaré sections. $\theta = 10^6$ and $\alpha = 0.5$ with both stokeslets acting towards the interface. Reflection of this figure in the z-axis will show the effect in the left hand side stokeslet due to symmetry.

tant result because it is necessary to know that viewing the three-dimensional problem as a simplified case within the plane provides valid results. Section 4.3 proceeds to illustrate the validity of this axisymmetric method of presenting results showing a plane containing the stokeslets will act as either an attractor or a repeller.

4.3 Three-dimensional flow fields and resulting particle paths

In the three-dimensional case we have more difficulty in applying the principles of Poincaré sections to illustrate the properties of the flow field. This is due to the nature of the problem having a fourth dimension, i.e. the three dimensions of the coordinate system and the time dependence of the problem. In section 4.2 we have eliminated this problem by merely considering two of the three dimensions. This created a restriction to motion in the plane rather than considering the full variability of paths in three coordinate directions.

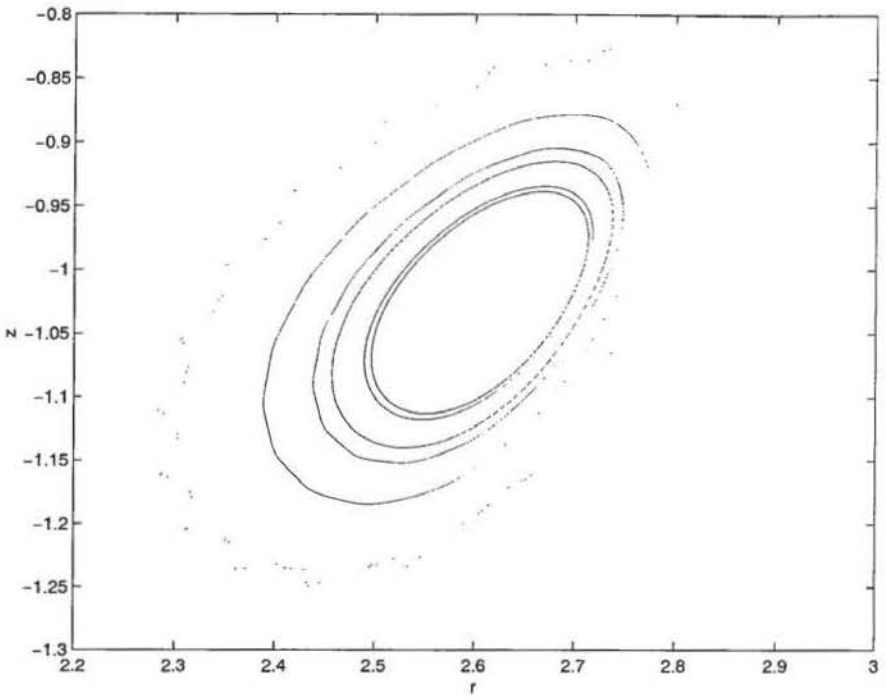

Figure 4.5: The horizontally displaced stokeslets positioned at $(0, \pm 3, -1)$ show a variation on the Poincaré section we have shown in the previous figure. Only the internal eddy associated with the right hand stokeslet is shown here. Again, $\theta = 10^6$ and $\alpha = 0.5$ with both stokeslets acting towards the interface. Reflection of this figure in the z-axis will show the effect in the left hand side stokeslet due to symmetry.

To be able to develop particle paths taken over time in the fluid around a micro-organism, one needs to consider recording their action in the fully developed three-dimensional flow field.

Cartwright, Feingold & Piro (1996) use a method of recording particle paths when constructing a three-dimensional unsteady flow between concentric spheres. They specifically study the dynamics of unsteady, spherical Couette flow with particular interest in the particle paths of idealised particles within the flow. They use the technique of taking Poincaré sections to reduce the dimension of the system by studying a map in either time or space. The dynamical behaviour of their system can then be studied with relative ease by way of a Poincaré map. In a three-dimensional flow, methods to plot a stroboscopic map do not give much information about the systems dynamics. Two methods are employed by Cartwright et al. (1996) to investigate extracting the information contained in such a map. The first looks at taking a thin slice of the actual space, a good technique

which reveals some of the salient features of the flow. The second is to project the map onto a plane. In cases when the system is not near integrable, this will not give much information about the flow. We use the latter method of projection (as opposed to taking slices of the flow) to illustrate the eddies and particle paths created for a near integrable case, see Figures 4.4 and 4.5. These are both very similar to Poincaré sections. However, unlike the previous Poincaré sections which have been constructed for a variety of parameters, we choose values of α and θ which give near integrable cases. Both of the figures show the internal eddies which have not been illustrated within the previous Poincaré sections. Figure 4.4 shows the islands which are formed on the innermost eddy. The corresponding stokeslet would be positioned between the two eddy structures, as expected and its coordinates are given in the figure caption. Figure 4.5 illustrates more detail of the inner eddy structure found between two stokeslets. It is noted that the stokeslet positions have changed so we can observe the inner eddy to a greater extent. The parameter values of α and θ remain the same and as shown previously; when considering smaller values of α one expects to see continuous lines due to the system being near integrable.

The island structures observed on Poincaré sections, created due to periodic points, can illustrate in some detail the effects of the stokeslets, as Figure 4.6 shows. We position the stokeslets a nominal distance of one unit below the z-axis. By starting a particle off the plane within which the stokeslets lie, we can see the particle tending towards the plane. In the case of the specific parameters and stokeslets position chosen to generate Figure 4.6, the particle settles into a structure of period eleven islands. Notice how the islands closest to the position of the stokeslet have become stretched and elongated as a result of the effect of increased forces. Figure 4.6 (b) looks directly onto the $y - z$ plane so that the correct perspective of each island can be seen.

Now we have illustrated the Poincaré sections for three dimensions by considering a projection or a slice of the flow, we move on to look at the overall path lines a particle may take over time. It is these lines which will show the tendency of a particle towards a plane whilst illustrating the attracting and repelling properties of the plane. Figure 4.7

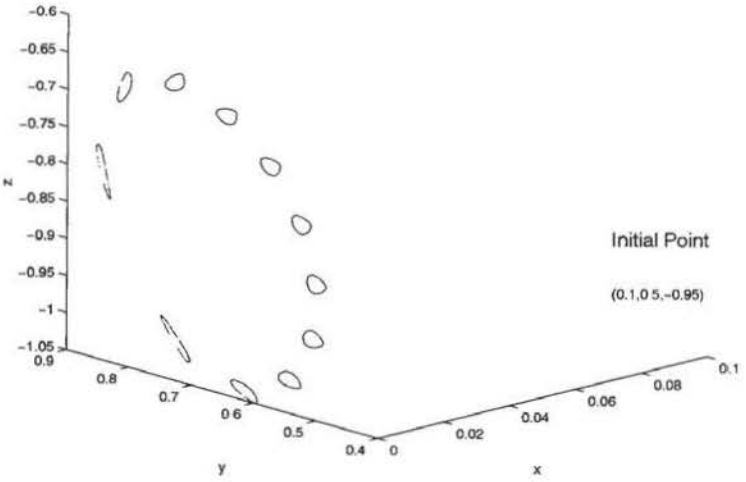

Fig. 4.6 (a) A three-dimensional particle path.

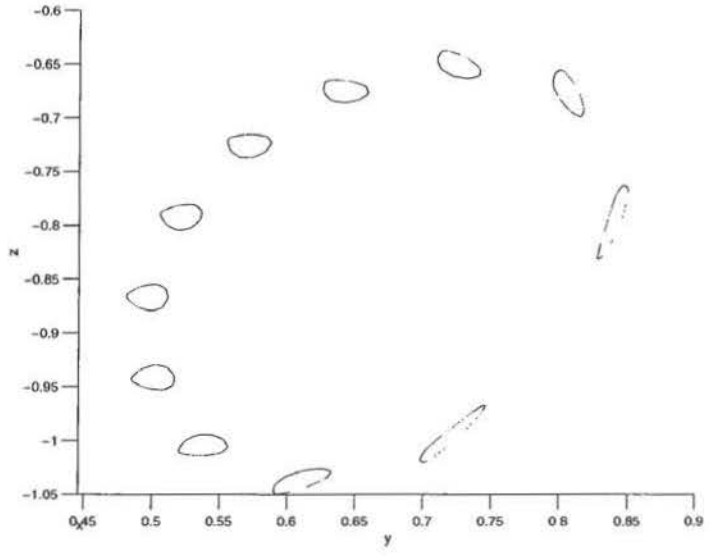

Fig. 4.6 (b) A section of the $y-z$ plane showing the region of attraction.

Figure 4.6: A particle path started at (0.1,0.5,-0.95) between the two stokeslets which are situated at $(0, \pm 1, -1)$.

gives an interpretation of a particle within the flow. The particle is initially located off the plane within which the stokeslets lie so that the path in three dimensions can be followed. This figure is three dimensional and therefore cannot be regarded as a Poincaré section because it merely tracks a particle whose position is recorded with every stokeslet pulse.

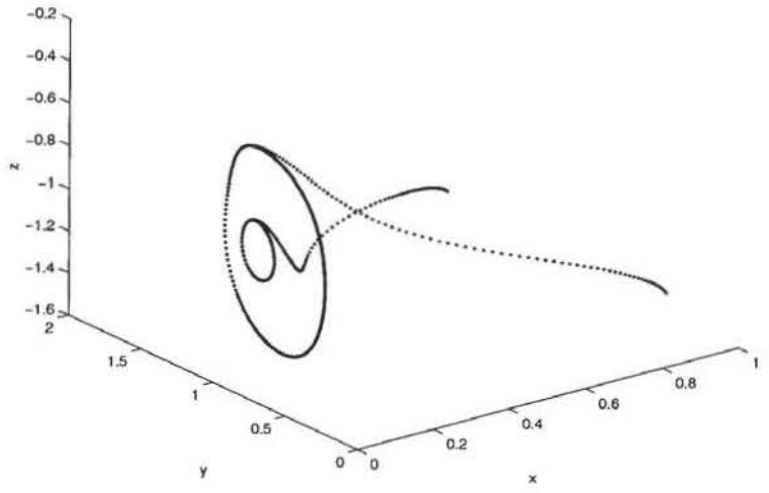

Figure 4.7: Computer generated three-dimensional paths to illustrate particles initially placed off the $y-z$ plane spiralling in towards it. The stokeslets are positioned in the $y-z$ plane at $(0, \pm 1, -1)$ and the map is for $\theta = 10^6$ and $\alpha = 0.1$.

Figure 4.7 shows the plane within which the stokeslets lie attracts the particles and in this particular case they proceed to move around a closed loop in this plane. During this three-dimensional study, the attraction properties of the plane within which the stokeslets lie has been open to investigation. The attraction or repulsion of the plane can be dependent on a number of factors, including the distance of separation between the stokeslets. We now proceed to explain how particles located in certain regions of space are attracted towards the plane whilst others are repelled away. This will reinforce the previous work in Chapters 2 and 3 where we confined particle motion to a plane section. We show how work in a plane was relevant due to the attracting properties of the plane implying only the consideration of particles situated within the stokeslets' plane. By considering particles whose initial positions are slightly displaced off the $y-z$ plane within which the stokeslets lie, we can study the flow direction of the tracers.

By investigating the displacement of an area composed of a number of points over several iterations of the map, we can begin to understand the overall flow directions. The area of the plane above the stokeslets' lateral position will attract particles who initially have the modulus of their y-coordinate less than the modulus of the stokeslet's

y-coordinate. We consider these points to start closer to the origin and the horizontal axis than the stokeslets' positions. For those particles who begin with the modulus of the y-coordinate greater than that of the stokeslet's y-coordinate modulus, but are situated close to the $y-z$ plane (i.e. x small) we see an initial trend of motion away from the $y-z$ plane, followed by an attraction back towards the plane once the particles have begun to feel the influence of both the stokeslets. In the regions further away from the stokeslets, although the velocity may be small, the stokeslets still have a marked effect when influencing the direction of movement of the particles. We illustrate this in Figure 4.8 which shows a particle tending towards the $y-z$ plane from two different initial positions. Figure 4.8 (a) shows the motion first out and then back towards the $y-z$ plane when the particle is initially situated above the stokeslet. In Figure 4.8 (b), the initial position is similar except for the z-coordinate placing it below the stokeslet. The different effect of the stokeslets can be seen in the loops which are created between the initial start position and the final resting trajectory of the particle on the eddy within the plane.

Numerically, we calculate the tracer moving close to the plane and then remaining an infinitesimal distance away from the plane. This is because the stokeslets are only creating forces in the $y-z$ plane resulting in zero velocity in the x-direction, i.e. perpendicular to the plane. This agrees with previous analysis because the only method by which a particle can reach the plane is if it travels along the axis of the stokeslet. The importance of the numerics implying there is no velocity moving particles off the plane of the stokeslets has allowed our earlier study to be completely based in the $y-z$ plane. The value of the velocity is found from the known stream functions (see section 2.2), allowing the calculation of velocities in both radial and vertical directions. Obtaining information on the value of these velocities can corroborate the explanation given above.

Analytically, determining which regions of the $y-z$ plane are attracting or repelling particles can again be derived from the velocity direction. This will confirm the observations made from the numerics which we have discussed in the paragraph above. For x close to zero, the leading-order term in the Taylor series expansion of the velocity is

zero. Hence, examining the first-order term in the expansion, it is possible to determine what happens close to and on the $y-z$ plane. We find above an approximately horizontal line running through the stokeslets positions, the first-order term is negative indicating an attraction to the plane. Below this imaginary line we find the opposite, and particles are repelled from the plane. This agrees with the trend of motion we see from Figure 4.8. This horizontal line does not remain parallel to the $x-y$ plane after passing to the right or left hand side of the stokeslets. Outside the stokeslets, the line begins to curve upwards, tending towards the y-axis. This indicates that the farther particles start from outside each of the stokeslets' positions, the more likely they are to be repelled away from the $y-z$ plane dependent on how close to $x=0$ they began. Overall, we generalise to say, more particles are likely to be attracted to the plane when they start from inside and above the stokeslets than any other position within the three-dimensional space.

4.4 Summary

This section has given validity to the analysis which we have presented in the previous chapters where we have considered the axisymmetric case of the flow associated with two horizontally displaced stokeslets. The three-dimensional results we have generated in this chapter are important within the biological context of the problem because of the environment the species inhabit. It is unusual for the organism under consideration in this study, SA, to live in isolation and instead they are often found congregated together creating a community of micro-organisms. Investigations into the actions of the eddies, and their influence on one another using graphics similar to Figure 4.2 to predict flow fields, can give an overview of the main flow features. This flow could be considered by superimposing the results we have generated onto a model for many organisms involving a distribution of stokeslets, rather than only two individual stokeslets. Due to the flow associated with each stokeslet being axisymmetric, we move towards a three-dimensional representation of the flow field for two or more stokeslets because this type of interaction

will not be axisymmetric. Most importantly, we can say the particles are influenced by the plane in which the flagella lie and so ultimately they will attract to that plane as the work within this chapter has illustrated.

For the penultimate chapter of this thesis, we consider a full three-dimensional study. Work within this current chapter will serve as an indication of the best location for particles to be initially located when we are interested in examining the features of the flow fields.

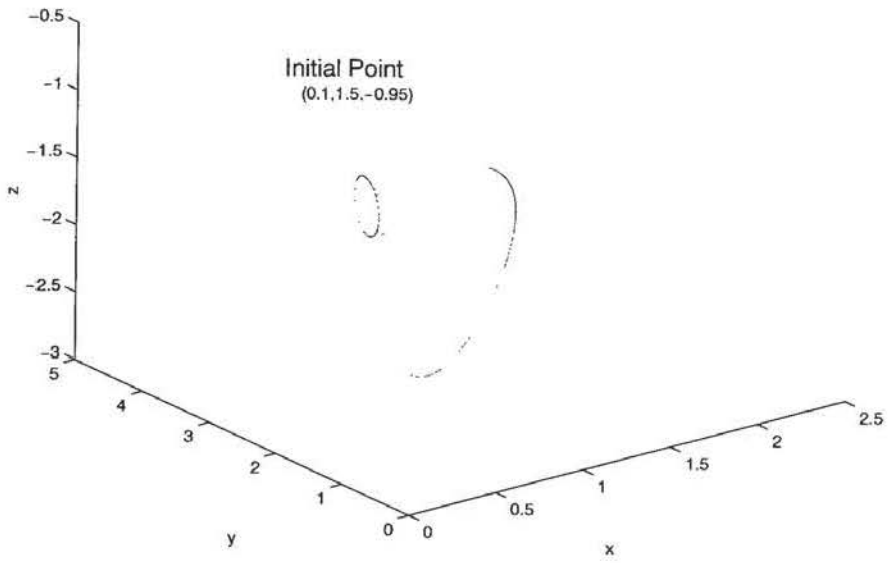

Fig. 4.8 (a) A particle spiralling towards the plane $x = 0$ from an initial position above the stokeslet. Once on the plane it moves along the orbit indefinitely.

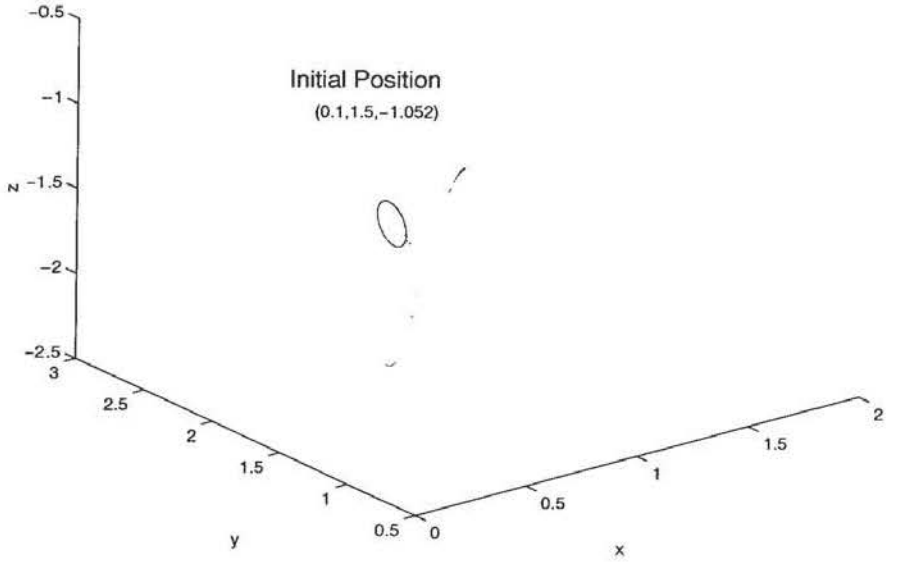

Fig. 4.8 (b) A particle spiralling towards the plane $x = 0$ from initial position below the stokeslet. Again, once on the plane it moves along the orbit indefinitely.

Figure 4.8: Particle paths in three dimensions. The first figure has the initial point starting above the stokeslet's position $(0, 1, -1)$ and shows how it spirals into the $y - z$ plane. The second figure has the initial position below the stokeslet and when this point spirals into the plane it settles onto an eddy between the two stokeslets.

Chapter 5

THE FLOW FIELDS AROUND SESSILE CHOANOFLAGELLATES DUE TO A HELICAL BEAT PATTERN

5.1 Abstract

The three-dimensional particle paths due to a helical beat pattern of the flagellum of a sessile choanoflagellate, *Salpingoeca Amphoridium* (SA), are modelled and compared against experimental observation. The organism's main components are a flagellum and cell body which are situated above a substrate such that the interaction between these entities is crucial in determining the fluid flow around the choanoflagellate. Due to the environment within which we observe the organisms residing, the flow of fluid around them can be characterised as Stokes flow. By distributing stokeslets and dipoles along a centre-line curve which has the form of a helix with a fixed, non-dimensionalised length, a flow field analogous to that created by the flagellum can be generated.

To model the flow due to the choanoflagellate, the interaction between the slender flagellum, the substrate above which the choanoflagellate resides (modelled as an infinite flat plane) and the cell body (modelled as a sphere) are incorporated. This is achieved by the use of image systems allowing the introduction of an appropriate set of Green's functions for a sphere and plane boundary as described in Higdon (1979*a*).

Results showing particle paths followed by passive tracers around the organism are generated. Results can be obtained for comparison with experimental results from Pettitt (2000) and Pettitt et al. (2001). In these experiments, polystyrene spheres were introduced into the organism's environment so that the action of these passive particles could be observed. The results illustrate particle velocities, flagellar forces and overall flow patterns. Applications such as inferring the length of flagellum and the distance from the substrate of an organism for whom particle paths are known can be investigated. Figures are presented comparing recorded experimental data with numerically generated results for a number of particle paths. The principal results show good agreement between the experimental study of certain cases considered in Pettitt (2000) and the paths tracer particles follow in numerically generated results.

5.2 Introduction

As motivation for the study of filter feeding currents around sessile microscopic organisms, we consider the motion of particles around *Salpingoeca Amphoridium* (SA), a type of choanoflagellate. This organism belongs to the phylum Protozoa and we investigate this specific organism due to the availability of experimental data provided in Pettitt (2000). Two further collared organisms with slightly different aspect ratios are investigated in Pettitt (2000) for comparison. The flow patterns associated with these can be compared to our results by varying the parameters in the model which follows (described in detail in section 5.3). Varying the stalk length between a number of organisms will allow a greater appreciation of the fluid dynamics of the system we are studying. In addition to the stalk length, we have considered effects of the substrate and the cell body. Other key parameters are those specifying the ratio of the dimensions of the organism around which we want to examine the flow of particles in relation to filter feeding. The paths particles take is important when investigating the optimum feeding patterns of these organisms.

Figure 5.1 shows a photograph of SA which can be compared to the sketch included

within the same figure. The sketch gives details of the dimensions of the organism. Typically, we can describe SA from the base upwards as consisting of first, a stalk attached to a substrate (which maybe a rigid surface or one covered in mucus) and joined at the other end to the cell. In the experiments from which we have taken the data, the substrate was a human hair. In some cases, we also find organisms directly attached to the substrate, i.e. there is no stalk to position the flagellum further away from the boundary. Again this effect may be investigated by altering the parameters within the model. The cell body is surrounded by the lorica which is a protective basket for the cell body. The flagellum, which emerges from the top of the cell body, causes the fluid to circulate around the organism. There is also a collar made up of fine finger-like projections, called micro-villi, which also emerge from the cell body and extend upwards and outwards around the flagellum. The collar is the filter where particles may become trapped before being transported close to the base of the flagellum (i.e. the 'mouth' region) where phagocytosis can occur. The angle of the collar is a feature which varies between different varieties of species studied in Pettitt (2000). The base of the flagellum, located inside the collar, is the region where the particles can be engulfed. Alternatively, the collar may not retain the particles which have been intercepted, providing another method by which mixing may be increased due to the release back into the fluid of these particles at a later time. This is explored in greater detail in Shimeta & Jumars (1991) who investigate various particle interception and retention methods.

In experiments, the particle size was investigated to look at the effect it had on retention of nutrients by SA. The latex microspheres used by Pettitt (2000) were 0.5μm in diameter. For the purpose of the model, we consider point-particles which will be influenced by the flagellum in the same manner as particles in experiments but which will give a perspective on the flow fields. We do not include the stalk's influence in the model because we assume that the effect of the cell body has a much greater influence on the fluid flow than the stalk. As in Higdon (1979*a*), and for simplification, we may neglect the addition of the collar at this stage. Due to the relative size of micro-villi compared to the

Fig. 5.1 (a)

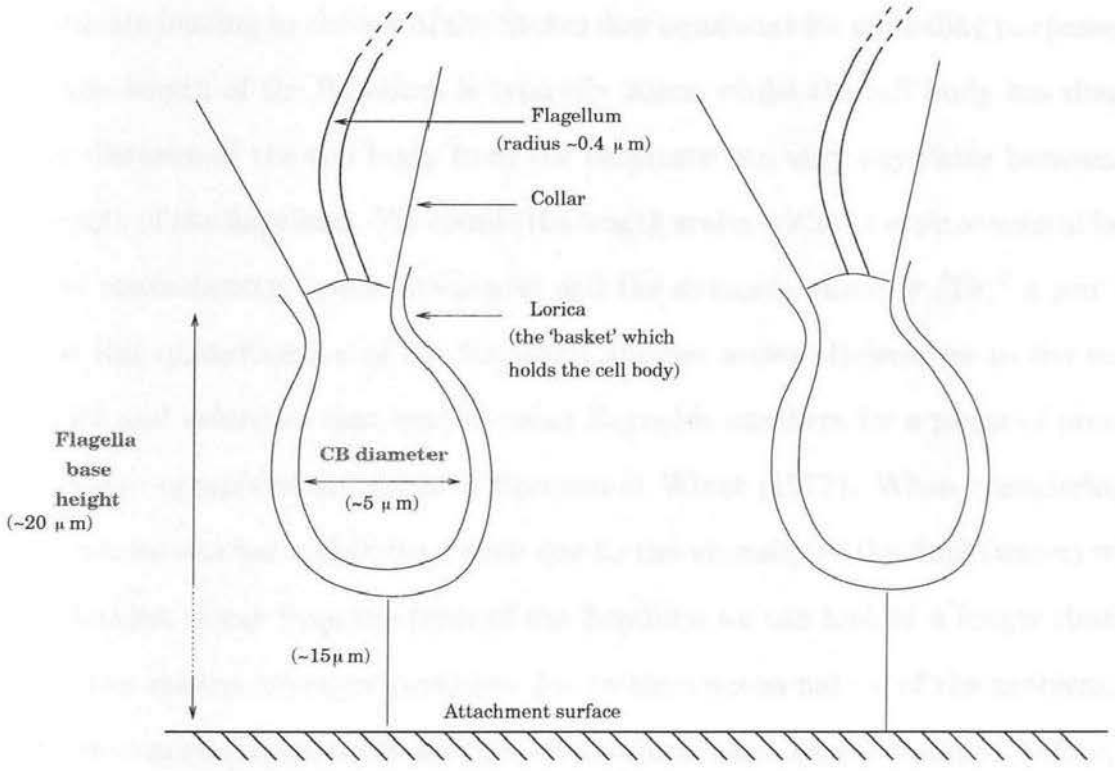

Fig. 5.1 (b)

Figure 5.1: A photograph and illustration of Salpingoeca Amphoridium showing details of the scale and structure. The photograph is magnified approximately 1000 times and the figure is not to scale.

cell and flagellum, this simplification is shown to provide a good initial approximation to the problem. Another simplification is the consideration of just one organism. In nature there exists an interaction between many of these organisms, whether they are adjacent to one another or above and below one another. By initially considering the model for the case of just one organism (or cell and flagellum system) we can infer the types of flow patterns we expect around a system where there is an interaction between more than one organism. Blake et al. (1998), Otto et al. (2001) and Orme et al. (2001*b*) consider the axisymmetric flow and two-dimensional flow interaction, respectively, between two horizontally displaced forces which can be considered indicative of the way in which two adjacent organisms may interact.

The typical dimensions of SA are of microscopic length scales so that as far as the fluid mechanics is concerned, the Reynolds number is very small and consequently viscous forces dominate leading to the use of the Stokes flow equations for modelling purposes. For example, the length of the flagellum is typically 20μm whilst the cell body has diameter 5μm. The distance of the cell body from the substrate can vary anywhere between zero and the length of the flagellum. We couple the length scales with the environmental factors such as the characteristic speed ($100\mu m/$s) and the dynamic viscosity (10^{-2} g μm^{-1}s^{-1}) to see how this quantification of the Reynolds number arises. References to the various length scales and velocities that lead to small Reynolds numbers for a range of problems involving micro-organisms are given in Brennen & Winet (1977). When considering the flagellar beat, we can use a slow time scale due to the viscosity of the fluid (water) within which SA resides. Away from the force of the flagellum we can look at a longer time step over which the system advances particles, due to the viscous nature of the problem.

There are various approaches to this work which have been examined before, and we will extend one of these methods initially by Higdon (1979*a*) beyond the range of that original work. Lighthill (1976) gives an excellent overview and review of flagellar hydrodynamics, encompassing flagellar motions and flow fields generated by a flagellum and later revisited the subject (see Lighthill (1996)). In Higdon (1979*a*), there is a study

of an organism very similar to SA which could also be described by Figure 5.1 (b). To model this organism, Higdon makes several assumptions, some of which are referred to above, and we will adhere to these initially. Higdon (1979*a*) relies on using the method of distributing singularities along the centre-line of the flagellum. The first use of this method for micro-organism locomotion was presented in the classic paper by Hancock (1953). Following this, the appropriate image system to satisfy the boundary condition in an approximate way is developed in greater detail in section 5.3.3. This leads to a complicated set of singularities which are based on the earlier work of Blake (1971) and Higdon (1979*b*).

The flagellar beat of SA usually occurs in three dimensions in a helical wave, which is the type of beat used during this study. From experimental data, one finds it is most usual for the beat of the sessile choanoflagellate to move in three-dimensional space rather than a two-dimensional plane. Note, it would be a straightforward extension of this study to consider the planar beat and hence derive particle paths associated with the optimal parameters as in Higdon (1979*a*). The first section of the following work formulates the helical beat pattern extending the planar case in Higdon (1979*a*). Note in later work, Higdon (1979*c*) does consider helical waves but with regard to the propulsion of a motile organism rather than a fixed organism as in the case presented here. This initial formulation of the helical wave includes considering the image systems required to satisfy the no-slip boundary conditions on the wall, the cell body and the flagellum.

Section 5.4 presents results of paths traced by particles in three-dimensional space. By varying the parameters of the problem, we are then able to compare and contrast our results to those observed experimentally in the work by Pettitt (2000). Velocity vectors are given for various flagellum forms. We then investigate how the various forces created by the beating flagellum will influence the particles within the fluid.

Discussion of the work, including how improvements have been incorporated into previous work, is presented along with how well the results represent the *in vitro* situation. We finally conclude in section 5.5 with a brief summary and details of possible extensions

to the work presented.

5.3 Representing and modelling the flow field

By specifying the shape of the flagellum as a function of time, we will be able to determine the velocity induced on particles within the fluid due to the forces acting along the flagellum. This is approached using the method of Green's functions. First, we need the form of the flagellum along which we will distribute singularities. By positioning stokeslets and dipoles at intervals along the centre-line of the slender flagellum, we can represent the flow field induced by the beating flagellum. Then one can construct the image system to satisfy conditions on any boundaries within the problem. This will lead to an approximate representation of the system such that the velocity at points within the fluid can be determined.

5.3.1 Kinematics

This section will introduce the function representation we use to initially represent the flagellum and mention modifications which can be made to the wave form later in the study. The function representation will allow one to determine the boundary conditions which must be satisfied to obtain an approximate solution to the problem.

The solution we consider involves satisfying the boundary conditions to determine the unknown values of the problem which, in this case, are the forces generated along the flagellum. The forces vary depending on position and time. If, for example, the section of the flagellum we are considering is at the extremity of the bent flagellum, the force created there will not necessarily be the same in magnitude as the force from a point in a straight mid-section, which sweeps directly across the axis of the flagellum. This consideration is more apparent for planar waves when we look at the range of forces they produce over one cycle of motion. The helical wave will have the same form throughout the beat cycle. To illustrate this, Figure 5.2 shows a representation of the forces positioned along a helical

flagellum above a spherical cell body. We know that for any rotation of this helix, the forces will keep the same magnitude and direction relative to the curve. This is important because we will be able to exploit this property when we investigate the interaction of the forces with a tracer particle. Thus, if we take a rotating frame within which the flagellum shape is always fixed, the force distribution will be the same for any time step within the rotating frame. Determining the forces and hence the velocities created within the fluid around SA can be derived by simply changing the line along which the forces of the flagellum lie. This is what happens every time the flagellum rotates to a new position and, by looking at small increments between each rotation, we will produce the impression of a continuous beat. To determine the force and hence the velocity acting on any tracer we choose within the fluid, it is important to know where the flagellum (and hence the forces) are situated with respect to the tracer. Initially, we are considering the cell body and substrate to be fixed and the flagellum to beat, which is identical to how the physical system is observed. In section 5.3.6 we will describe how the cell body and substrate are located in a fixed coordinate system whilst the flagellum is within a rotating frame relative to the fixed frame.

We introduce in greater detail the three-dimensional helical representation of the flagellum. The problem is set up such that it is straightforward to consider the two-dimensional problem. Figure 5.3 shows the model we use to describe the coordinate axes relative to the wave pattern, the cell body and the substrate. We will show a similar figure later in section 5.3.6 (see Figure 5.4 (c)) where we introduce the rotating axes which are very important as a frame of reference for the tracer. Figure 5.3 is similar to Figure 1 in Higdon (1979*a*) but the figure included within this work has a third dimension. We begin by describing points along the wave by the vector

$$\mathbf{X} = (X, y(X,t), z(X,t)).$$

Further, we can define a wave form with constant amplitude and wave number (as in

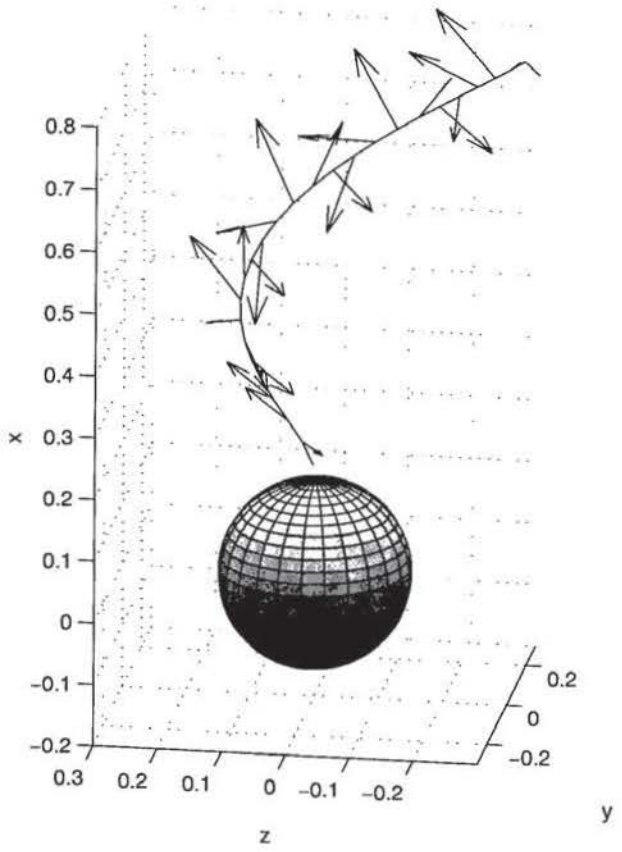

Figure 5.2: A representation of the force distribution along the centre-line of a helical flagellum for a given position and time.

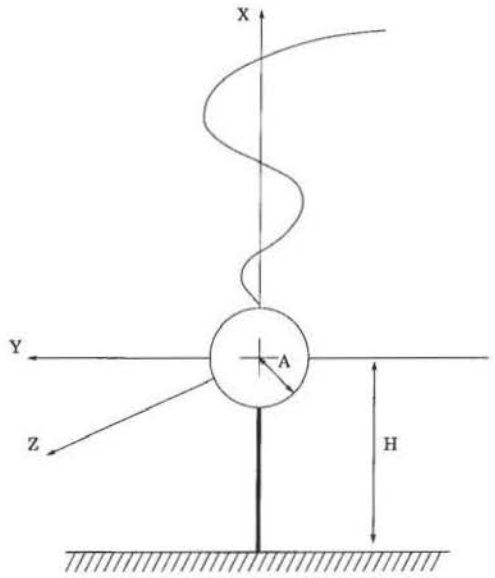

Figure 5.3: A reproduction of Figure 1 from Higdon (1979a) showing the model we will study in three dimensions. The height of the cell body above the smooth infinite plane and the cell body radius are indicated.

Higdon (1979*a*)) such that

$$y(X,t) = \alpha^* \sin[k(X - X_0) + \vartheta(t)], \quad z(X,t) = \alpha^* \cos[k(X - X_0) + \vartheta(t)], \tag{5.1}$$

where X_0 is the X-coordinate giving the height of the base of the flagellum. The direction of wave motion created by this description will be dependent (amongst other factors) upon both the function $\vartheta(t)$ in the argument of the trigonometric functions and the parameter α^*. The function $\vartheta(t)$ describes the phase velocity of the wave such that one can determine how far through the beat cycle we have progressed. The parameter α^* will describe the amplitude of the wave. However, on examining the wave form created by $\mathbf{X}$ for a specific time t and over a range of X, there is a noticeable difference to that produced in nature by SA. The wave amplitude of SA grows gradually from the base and reaches its maximum amplitude about a third of the way along its length. Therefore, we alter (5.1), multiplying both the terms for y and z by the exponential function given as

$$E(x) = 1 - \exp[-(k_E x)^2].$$

The value of k_E is chosen such that the wave will reach its maximum amplitude a third of the distance along its length. In this case, $k_E = 5$ will give $E(x) \approx 0.9$ when $x = 0.3$. This exponential function creates a more realistic wave form and more importantly satisfies the condition that the flagellum is attached radially to the cell body. This is because of the exponential function's properties which give: $E(0) = 0$, $E'(0) = 0$ and $E(\infty) = 1$. Therefore equation (5.1) can now be rewritten as

$$\begin{aligned} Y(X,t) &= E(X - X_0)\alpha^* \sin[k(X - X_0) + \vartheta(t)], \\ Z(X,t) &= E(X - X_0)\alpha^* \cos[k(X - X_0) + \vartheta(t)], \end{aligned} \tag{5.2}$$

where $\mathbf{X} = (X, Y(X,t), Z(X,t))$ now describes any point along the flagellum. Now that we have an expression for the wave form, one can begin to construct the velocity components

at various points along the flagellum. These will ultimately affect the velocity of the fluid in both the near and far fields. This is significant because the method of distributing singularities within this problem is important when we determine the strengths of the singularities for each fixed interval defining the flagellum.

For consistency, we assume the flagellum is inextensible which necessitates the length of the flagellum remains constant over all periods of the beat. We will divide the flagellum into segments of equal length in this case using arc length as the length dimension. The beginning and the end of each segment is denoted by s_i and s_{i+1} respectively, where $i = 0, ..., N-1$ and the flagellum is split into N intervals. Hence, in the three-dimensional case, arc length is given by

$$s = \int_{X_0}^{X} \left[1 + \left(\frac{\partial Y}{\partial X} \right)^2 + \left(\frac{\partial Z}{\partial X} \right)^2 \right]^{\frac{1}{2}} \mathrm{d}X. \tag{5.3}$$

Each of the N segments has length L/N, where the total length of the flagellum is L. Substituting into equation (5.3) the known values of each s_i (for $i = 1, .., N$) we can determine the corresponding X-coordinates. (Notice that s_i can be described as giving the arc length from the base of the flagellum to the end of the i^{th} interval). This is calculated via the method of cubic interpolation which allows one to find the corresponding value of X for a known value of s. We take the curve as the known function given in equations (5.2). The integral value, s, can then be chosen at set intervals, i.e. the various s_i, and the corresponding coordinate along the helix axis of the centre-line of the flagellum, X_i, can be found. Once we know the position on this axis, the other two cartesian coordinates can be determined using equations (5.2).

We now have a vector describing the motion of a particular segment of the flagellum for each time step and for each arc length position (s_i). This means that for any chosen time, one can describe an approximation to the position of the whole flagellum and also the positions it will move to over subsequent time steps. If we assume the flagellum has been approximated using linear segments, the midpoint of each segment, s_i^m, can be defined

to lie equidistant between each s_i and s_{i+1} along the centre-line of the flagellum. These are used later to enable the derivation of the forces created by the singularities which are taken to be situated at the midpoint of each flagellum segment. The work by Hancock (1953) describes the method we use to place a distribution of stokeslets and dipoles along the centre-line of the flagellum. Assuming that the flagellum can be described as slender, i.e. as having a small radius compared to its length, then one can find the velocity induced at any segment on the flagellum. Hancock (1953) shows that by assuming the length of a segment ($|s_{i+1} - s_i|$) to be large compared to the flagellum radius, the consideration of a distribution of singularities within that segment making a contribution to the velocity of the segment is a sufficiently good representation of the forces. Since this process can be repeated for all segments, we can build up the velocity profile created by the whole flagellum. Further details are given in Hancock (1953).

5.3.2 The singularity structure

Following Higdon (1979*a*) closely, this section will give details of each of the singularities which we will need to find an approximate representation of the flow fields around SA. The methods by which we propose to satisfy the assumptions and boundary conditions (some of which are given in the previous section) will follow with the introduction of various image systems. We initially present this work for the coordinate system as illustrated in Figure 5.3 but note that we later introduce an alternative coordinate system for which the structure presented here will remain similar bar a simple rotation, see section 5.3.6.

Higdon (1979*a*) modelled an organism which he assumed had a smooth slender flagellum and a spherical cell body, with the height of the cell body a fixed distance above the substrate. The flagellum was represented by placing stokeslets and dipoles along the centre-line of the flagellum. This type of distribution enabled the fluid around the organism to feel the forces which the flagellum should create due to its typical beat pattern. Because the flagellum is attached to a cell body above a substrate, the interaction between these separate entities (the sphere and the plane) needs to be taken into account. So that

the fluid and particles within this system move in accordance with the organism. Green's functions are used to allow the correct boundary conditions to be observed.

Using Higdon's approximation to the organism, the boundary conditions we must satisfy are no-slip on the cell body, substrate and flagellum (which is beating in a helical motion). These conditions are described in greater detail in section 5.3.3. They briefly arise due to the introduction of image systems which must satisfy the conditions of no-slip on the surfaces in the model. We assume the flagellum is modelled by a helical wave (as discussed in detail in section 5.3.1 when introducing the wave type). We are looking at a very thin flagellum where we take its length, L, to be much greater than the flagellum radius, a, i.e. $L \gg a$. This is referred to as the slender-body approximation. This approximation allows one to consider the flagellum being represented by a helical line as described in section 5.3.1 and given by equation (5.2). Along this line, we distribute both stokeslets and dipoles along with their associated image systems. Due to the approximations of a slender body, the image system and the distribution of singularities, Higdon (1979*a*) is able to state that this model is representative of the effects of the flagellum within this system.

The shape of the flagellum is time dependent within a fixed coordinate system, hence the wave form will be both dependent on space and time. Also, the force from the flagellum will be dependent on the degree of bend in the wave (defined using the parameters and functions given by α^*, k, k_E and ϑ in expression (5.2)) and the number of dimensions the wave moves in. Higdon (1979*a*) considered a sinusoidal wave within a plane for a sessile organism, and then later the three-dimensional case of helical waves for a motile organism, Higdon (1979*c*). The first paper looks in detail at the use of stokeslets, dipoles and images to define the problem, and we now proceed to explain how we use this type of formulation and convert the problem to a numerical method from where particle paths can be generated. In our case, we are interested in how varying the parameters describing the organism in the model affect the tracers situated within the fluid. Following the progression of particles over time around the model of a single organism will lead to insight

into how well mixed the particles can become. As well as allowing comparison with the experimental results in Pettitt (2000), this also gives data which can be used to predict unknowns from the experimental results. For example, by examining the particle paths taken by an organism for whom certain dimensions are unknown, a prediction can be made from the models' parameters inferring the actual dimensions of the organism. This may be useful when the results from experimental measurements and recordings lack either clarity or details of the cell's dimensions. Interesting comparisons to the flow fields created in the axisymmetric case where a single point force creates an approximate representation of the flagellum could also be made. This more straightforward representation has been considered in Orme et al. (2001*b*). In previous axisymmetric work, where we have two dimensions of space and the third dimension is time, we see chaos due to the action of two alternating stokeslets. We note that where chaos previously appeared because of the time dependence in the axisymmetric flow, chaotic mixing if present in this case, will be due to the three-dimensional nature of the problem.

The problem, defined by Higdon (1979*a*), initially requires the use of a stokeslet, a Stokes-doublet and a dipole, which give the fundamental building blocks for the model. For all of these singularities, we regard the force to be acting at a point $\mathbf{y}$ whilst the tracer or particle which the force is affecting is situated at $\mathbf{x}$. Typically, we would be interested in $\mathbf{y}$ as a location of a stokeslet on the centre-line of the flagellum, whilst the general position of a particle within the fluid would be at $\mathbf{x}$. The stokeslet is given by

$$S_{jk}(\mathbf{x},\mathbf{y}) = \frac{\delta_{jk}}{r} + \frac{r_j r_k}{r^3}, \tag{5.4}$$

where we define $r = |\mathbf{x}-\mathbf{y}|$ and $r_m = (x_m - y_m)$. This definition is carried throughout the following work, along with δ_{jk} which is defined as the usual delta function. This stokeslet creates a velocity at $\mathbf{x}$, due to a force with strength and direction $\mathbf{f}$ acting at $\mathbf{y}$, defined by

$$u_j(\mathbf{x}) = S_{jk}(\mathbf{x},\mathbf{y})\frac{f_k}{8\pi\mu}.$$

Here, the parameter μ represents the viscosity of the fluid. The subscripts j or k (as for all the following work) indicate the components of the force, $\mathbf{f}$, or the velocity, $\mathbf{u}$, with respect to direction.

The second type of singularity can be derived by differentiating equation (5.4) with the operator $\partial/\partial y_l$, which due to linearity gives another solution to the Stokes equations called a Stokes-doublet. This is given as

$$S^D_{jkl}(\mathbf{x},\mathbf{y}) = \left(-\frac{\delta_{kl}}{r^3} + \frac{3r_k r_l}{r^5}\right) r_j + \left(\frac{r_l\delta_{jk} - r_k\delta_{jl}}{r^3}\right). \tag{5.5}$$

If the Stokes-doublet has tensoral strength σ_{kl}, then the velocity at the point $\mathbf{x}$ due to a Stokes-doublet acting at point $\mathbf{y}$ (again taken to be situated on the flagellum) is given by

$$u_j(\mathbf{x}) = S^D_{jkl}(\mathbf{x},\mathbf{y})\frac{\sigma_{kl}}{8\pi\mu}.$$

The Stokes-doublet can be considered in its physical sense as consisting of two components. From equation (5.5), the first is the symmetric component which is a fundamental singularity called as stresslet. It represents the straining motion of the fluid. The second is the antisymmetric component called a rotlet. Physically, this generates a flow due to the action of a torque.

Finally, we can differentiate equation (5.4) again to obtain the second derivatives. The term we have most use for is the dipole, derived from the Laplacian of the stokeslet. Differentiating the stokeslet with respect to the operator $-\frac{1}{2}\nabla^2_y = -\frac{1}{2}\frac{\partial^2}{\partial y_k^2}$ gives the dipole in its standard form as

$$D_{jk}(\mathbf{x},\mathbf{y}) = \frac{-\delta_{jk}}{r^3} + \frac{3r_j r_k}{r^5}. \tag{5.6}$$

Again, the velocity field $\mathbf{u}$ at a point $\mathbf{x}$ created by a dipole of strength and direction $\mathbf{d}$ which is situated at $\mathbf{y}$ is given as

$$u_j(\mathbf{x}) = D_{jk}(\mathbf{x},\mathbf{y})\frac{d_k}{4\pi}.$$

Equations (5.4), (5.5) and (5.6) give all the components we require to be able to construct the Green's function enabling the description of the fluid flow around the flagellum, cell body and substrate whilst satisfying the relevant boundary conditions by the introduction of image systems. We now proceed to introduce and then explain the image systems we require, but will neglect to include any great detail of the more complicated equations to facilitate the reader's understanding.

5.3.3 Construction of the image systems

As mentioned at the start of section 5.3.2, the distribution of singularities along the flagellum creates a velocity field which alone does not satisfy all the boundary conditions of the problem to a satisfactory degree of accuracy. By the introduction of specific Green's functions, which include the image systems for these singularities, the correct combination of singularities can be considered such that we satisfy all the given boundary conditions to second order with respect to the radius of the cell body over the distance from the plane. However, the problem is more complex than simply looking at one boundary on which we need to satisfy any given condition. For example, once we have satisfied the no-slip conditions on the plane boundary (i.e. the substrate) we need to consider how the introduction of the forces which allow the boundary conditions to be satisfied have affected the other boundary conditions, such as the no-slip condition on the sphere (i.e. the cell body). Hence, we simultaneously have to consider the sphere's surface, and the sphere and boundary interaction too. We present first the image system for a sphere, second for a plane and finally combine the two, enabling all the boundary conditions to be satisfied approximately to second order, as above.

The Green's function for flow external to a sphere is given by

$$G^S_{jk}(\mathbf{x},\mathbf{y}) = S_{jk}(\mathbf{x},\mathbf{y}) + S^*_{jk}(\mathbf{x},\mathbf{y}), \tag{5.7}$$

where S^*_{jk} represents the image system for the sphere. Using the same method as for

the fundamental singularities, we can now see that the velocity at any point $\mathbf{x}$ due to a point force $\mathbf{f}$ acting at a point $\mathbf{y}$ (situated on the flagellum) in the presence of a sphere (representing the cell body) is given by

$$u_j(\mathbf{x}) = G^S_{jk}(\mathbf{x}, \mathbf{y}) \frac{f_k}{8\pi\mu}. \tag{5.8}$$

The components of this equation have the same definition as those which are given after equation (5.4). The expression for S^*_{jk} is complicated and the details of the equation can be found in Appendix D (see also Higdon (1979*a*)). However, physically it is informative to consider how the expression is constructed with regard to the forces acting within the system. The image system involves considering singularities associated with the inverse point $\mathbf{y}^*$ defined as

$$\mathbf{y}^* = \frac{A^2}{|\mathbf{y}|^2}\mathbf{y} = \frac{A^2}{|\mathbf{y}|}\left(\frac{\mathbf{y}}{|\mathbf{y}|}\right).$$

We can interpret this point as the image in the sphere of the point $\mathbf{y}$ which is dependent on the ratio of the sphere's radius, A, to the distance of $\mathbf{y}$ from the origin or centre of the sphere, i.e. $|\mathbf{y}|$. In this problem, both the origin and the centre of the sphere are coincident. This is depicted diagrammatically in Figure 5.4 (a). Higdon (1979*a*) gives S^*_{jk} in terms of $\mathbf{y}^*$ as derived by Oseen (1927) along with a relatively simpler expression in terms of individual fundamental singularities. As an approximation to the Oseen expression for the image system, one can consider the first- and the second-order terms in an expansion of the expression for the image system about the origin, when the radius of the sphere is much smaller than the distance of the stokeslet from the origin (i.e. $A \ll |\mathbf{y}|$). The physical construction of this image system can be explained in terms of the radial and transverse components of the stokeslet. Radially, the images of a stokeslet are: a stokeslet, dipole and a stresslet all situated at the inverse point. Transversely, the images are: a line distribution of stokeslets, dipoles and Stokes-doublets which stretch from the origin to the inverse point. By neglecting terms $O\left(\frac{A^2}{|\mathbf{y}|^2}\right)$, which are very small, Higdon (1979*a*) gives an expression for S^*_{jk} which lends itself to numerical methods more so than Oseen's

complicated expression. The inclusion of the image system now means that we have approximately satisfied the boundary conditions on the sphere, i.e. no-slip on the sphere's surface to first order. Notice that the simpler expression stated within Appendix D does not explicitly depend on the inverse point, $\mathbf{y}^*$, whereas the Oseen expression was highly dependent on this term. This is why one chooses to use the alternative representation of these image systems, expressing them in terms of their symmetric and antisymmetric components.

Now we have an expression for the image of a stokeslet, $S^*_{jk}(\mathbf{x},\mathbf{y})$, we can use the following rule to enable one to find images of the higher-order singularities, such as the image of the Stokes-doublet and the dipole, which are also required to enable the boundary conditions to be satisfied. This rule specifies that if we have a solution of the Stokes equations defined by a certain differentiable operator, then the image system in the sphere for this solution (singularity) is defined by the same differential of the image of the solution (singularity).

The strength of the stokeslets' distribution along the flagellum which we will calculate (see section 5.3.5) and their interaction with the sphere, enable the calculation of the force and moment on the sphere as well giving the flow fields generated by the flagellum. The interaction of the singularities (doublets and dipoles) which we have introduced, need considering as they too will have image systems due to the interaction between the flagellum, plane and sphere. These image systems will therefore affect the calculation of the force and moment on the sphere as well as the flow fields. Hence, by using the rule defined above (omitting the details) the image of a Stokes-doublet in the sphere is given by

$$\frac{\partial}{\partial y_l}\left(S^*_{jk}\right) = S^{D*}_{jkl}(\mathbf{x},\mathbf{y}),$$

and the image system for a dipole in the sphere by

$$-\frac{1}{2}\nabla^2_y\left(S^*_{jk}\right) = D^*_{jk}(\mathbf{x},\mathbf{y}).$$

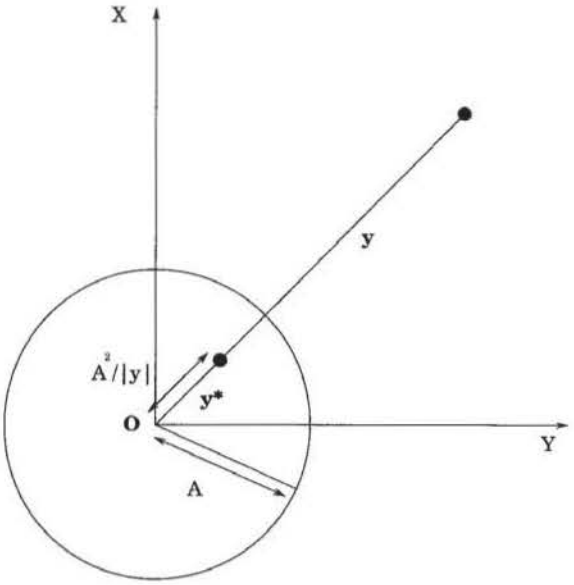

Fig. 5.4 (a) The figure shows how the point $\mathbf{y}$ and the radius of the sphere A determine the position of the inverse point, $\mathbf{y}^*$, inside the sphere.

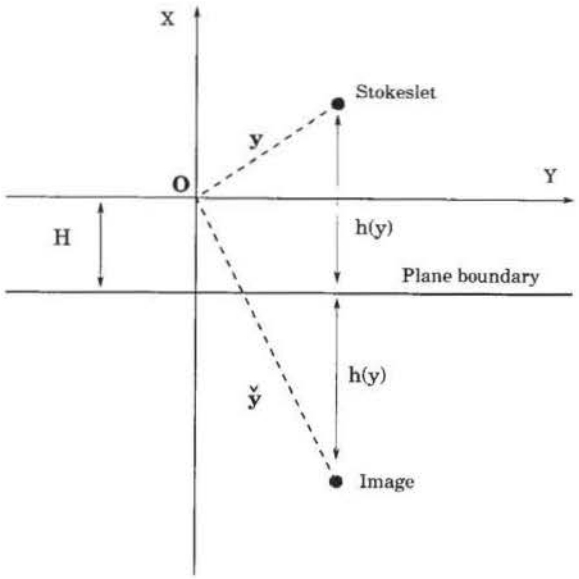

Fig. 5.4 (b) The figure shows how the image point $\check{\mathbf{y}}$ is defined and how it is dependent on the position of the stokeslet $\mathbf{y}$. The distance of the stokeslet at $\mathbf{y}$ from the plane is given by $h(\mathbf{y})$ and also gives the distance of the image point from the plane.

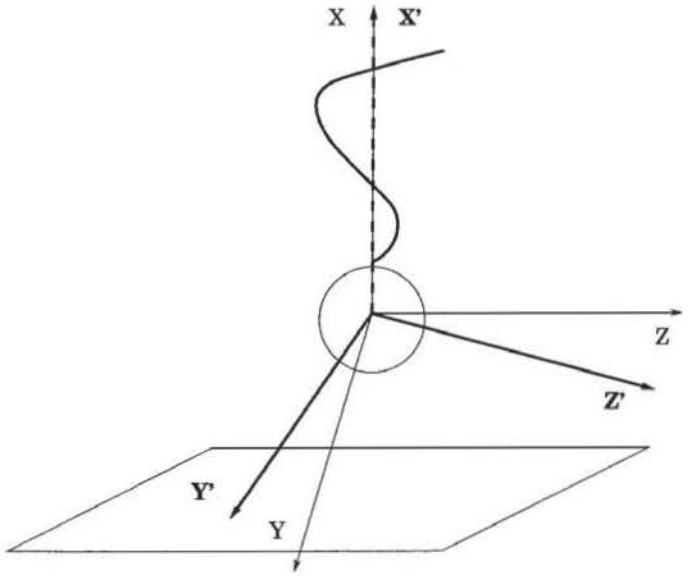

Fig. 5.4 (c) Representation of the three-dimensional rotating coordinate system, with the axis of the flagellum having a coincident axis with the fixed body frame (denoted by coordinates with no primes) and the rotating flagellum frame (denoted by coordinates with primes).

Figure 5.4: Figures showing features of the three-dimensional model including the inverse point and the image point.

A complete set of sphere images has now been stated in brief form. (Again the explicit versions can be found in both Appendix D and in Higdon (1979*a*) who composes each image system into its simpler first and second-order terms as previously explained for the image system of the stokeslet).

Notice that equation (5.8) allows us to satisfy the boundary conditions when we have a single force acting at a point $\mathbf{y}$ outside a sphere, i.e. the velocity at any point given by expression (5.8) on the boundary will be zero due to a force which acts at $\mathbf{y}$. Therefore, rather than considering a single force acting, we will consider a distribution of these forces according to the equation which defines the flagellum and then proceed to find the effect of all these forces on a tracer at any position $\mathbf{x}$ within the fluid. Hence, to find the effect on $\mathbf{x}$ over a period of time, i.e. to be able to follow a point over time, we need to find the forces along the flagellum for each time increment over this period. With each time step, the position of the flagellum with respect to a fixed frame will change and therefore the distribution of forces with respect to this fixed frame will also alter. In turn, this implies that a particle within the fluid at $\mathbf{x}$ will feel a different moment and hence a different velocity will be produced at each time step. This could become computationally expensive if one solves to find the force distribution at each time step in order to derive the velocity at position $\mathbf{x}$. However, by considering rotating axes, one can eliminate this problem by merely solving the equations for the boundary conditions only once to find the force distribution. Section 5.3.6 introduces the rotating coordinate system with relevance to finding the solution of this force distribution along the flagellum from the equations given in section 5.3.5 which enable the boundary conditions to be satisfied.

As mentioned above, we also need the image system for a plane, which is derived using a similar method to the case for the image system of a sphere. We use Green's functions to make sure the correct conditions are satisfied on the boundary, which in this case is the plane boundary or substrate to which the organism is attached. We need to set up the correct image point, $\check{\mathbf{y}}$, for a stokeslet at $\mathbf{y}$ in the boundary and Figure 5.4 (b) shows how this is achieved. If we define $\mathbf{p}$ to be a unit vector perpendicular to the plane (which

is the substrate in this case) and pointing in the direction of the fluid (upwards for an organism situated above the substrate) then we can define the image point $\check{\mathbf{y}}$ as

$$\check{\mathbf{y}} = \mathbf{y} - 2h(\mathbf{y})\mathbf{p}, \tag{5.9}$$

where $h(\mathbf{y})$ is the distance of the point, $\mathbf{y}$, from the plane or substrate.

The Green's function for the half space, G^P_{jk}, is given as

$$G^P_{jk}(\mathbf{x}, \mathbf{y}) = S_{jk}(\mathbf{x}, \mathbf{y}) + \check{S}_{jk}(\mathbf{x}, \mathbf{y}), \tag{5.10}$$

where $\check{S}_{jk}$ is the image system for the plane and consists of a stokeslet, Stokes-doublet and a dipole all situated at the image point $\check{\mathbf{y}}$. Again the details are omitted here, but a more explicit expression for $\check{S}_{jk}$ is given in Appendix E.

Notice that in the case of the image system for the plane, we have no difficulties in expressing the terms for the image system in the plane. However, in the case of the sphere we needed to distribute the singularities such that there were each of: a stokeslet, dipole and stresslet all situated at the inverse point as well as a line distribution of stokeslets, dipoles and Stokes-doublets from the origin to the inverse point. This ensured that both radial and transverse components of the boundary condition on the sphere were satisfied. In the case of the plane, there is no such distribution of singularities due to the simpler geometry of a plane compared to a sphere and so the resulting image system is more apparent.

Now we have the separate image systems defined for the sphere and the plane, it is necessary to consider the combined image system which will serve as an initial approximation to enable us to represent the physical system. Higdon (1979*a*) makes an initial conjecture (a first approximation) that the Green's function must be composed of the stokeslet along with both the image systems for the plane and the sphere, which gives

$$G_{jk}(\mathbf{x}, \mathbf{y}) \approx S_{jk}(\mathbf{x}, \mathbf{y}) + S^*_{jk}(\mathbf{x}, \mathbf{y}) + \check{S}_{jk}(\mathbf{x}, \mathbf{y}). \tag{5.11}$$

However, as we showed previously, we have the problem of considering the images of the other singularities which are present in equation (5.11), i.e. the contribution from the terms S^*_{jk} and $\check{S}_{jk}$, and the effects their combined force distributions induce on the boundary conditions. This means that although the individual image systems for the sphere and plane may satisfy the boundary conditions independently, the combined effect induced by their images may not. Therefore, we need to consider the image of the plane's image system ($\check{S}_{jk}$) in the sphere, which we denote by $\check{S}^*_{jk}$. This is another complicated expression, but the reasoning for its form is easily understood by examining a breakdown of the terms included in $\check{S}^*_{jk}$ (details can be found in Appendix E). Briefly, the image system for the plane consists of a stokeslet, Stokes-doublet and a dipole, and so by replacing all of these singularities by their images in the sphere, then we have found the images of the plane image system in the sphere. By appending equation (5.11) to include this term, we obtain an improved approximation for the combined Green's function as

$$G_{jk}(\mathbf{x},\mathbf{y}) \approx S_{jk}(\mathbf{x},\mathbf{y}) + S^*_{jk}(\mathbf{x},\mathbf{y}) + \check{S}_{jk}(\mathbf{x},\mathbf{y}) + \check{S}^*_{jk}(\mathbf{x},\mathbf{y}). \tag{5.12}$$

However, this expression still does not satisfy the boundary conditions to second order within our model. For an improved approximation we need to consider terms from both S^*_{jk} and $\check{S}_{jk}$ whose plane images have not been included in (5.12).

This process is broken into three stages to enable all the boundary conditions to be satisfied by determining which singularities are violating which specific boundary conditions. Firstly, the leading-order terms of the plane images for the terms S^*_{jk} and $\check{S}_{jk}$ are considered. We replace the stokeslets of these leading-order terms, which are given as

$$-\frac{3}{4}AS_{kl}(0,\mathbf{y})S_{jl}(\mathbf{x},0) - \frac{3}{4}A\check{S}_{kl}(0,\mathbf{y})S_{jl}(\mathbf{x},0),$$

by their plane images to give

$$-\frac{3}{4}AS_{kl}(0,\mathbf{y})\check{S}_{jl}(\mathbf{x},0) - \frac{3}{4}A\check{S}_{kl}(0,\mathbf{y})\check{S}_{jl}(\mathbf{x},0). \tag{5.13}$$

However, by adding equation (5.13) to equation (5.12) and correcting the velocity on the plane, we have now induced another velocity on the sphere's surface. We minimise this velocity in an attempt to satisfy the boundary conditions by adding the sphere image of the expression given in (5.13) to equation (5.12). The expression from (5.13) can be rewritten to satisfy this condition as

$$-\frac{3}{4}AS_{kl}(0,\mathbf{y})\check{S}^{*}_{jl}(\mathbf{x},0)-\frac{3}{4}A\check{S}_{kl}(0,\mathbf{y})\check{S}^{*}_{jl}(\mathbf{x},0). \tag{5.14}$$

Hence, by adding both expressions (5.13) and (5.14) to equation (5.12), we find that we have satisfied the boundary conditions on the plane and the sphere to second order.

The final expression that gives the approximate Green's function when one is considering the flow due to a force acting at $\mathbf{y}$ in the presence of a sphere within the half plane above a plane boundary is

$$\begin{aligned} G_{jk}(\mathbf{x},\mathbf{y}) = {} & S_{jk}(\mathbf{x},\mathbf{y})+S^{*}_{jk}(\mathbf{x},\mathbf{y})+\check{S}_{jk}(\mathbf{x},\mathbf{y})+\check{S}^{*}_{jk}(\mathbf{x},\mathbf{y}) \\ & -\frac{3}{4}A[S_{kl}(0,\mathbf{y})+\check{S}_{kl}(0,\mathbf{y})][\check{S}_{jl}(\mathbf{x},0)+\check{S}^{*}_{jl}(\mathbf{x},0)], \end{aligned} \tag{5.15}$$

where again the velocity created at $\mathbf{x}$ due to the system described is given by

$$u_j(\mathbf{x}) = G_{jk}(\mathbf{x},\mathbf{y})\frac{f_k}{8\pi\mu}.$$

This velocity is due to the contribution of only a single force at position $\mathbf{y}$ which we assume to lie at some location along the centre-line of the flagellum. The next section considers the effects of many of these forces distributed along a curve defining the centre-line of the flagellum. This enables the velocity at any position $\mathbf{x}$ to resemble velocities created within a flow field around any organism similar to that which we have chosen to model.

5.3.4 Flow fields associated with singularities representing the flagellum

Equation (5.15) gave the Green's function which allowed the definition of the velocity created at any point $\mathbf{x}$ within the fluid due to a stokeslet of strength $\mathbf{f}$ situated at a given position $\mathbf{y}$ in the physical system described in section 5.2. The fundamental singularities situated along the flagellum are both stokeslets and dipoles at prescribed intervals which allows a correct representation of the motion created as the flagellum beats. The reader is referred to the end of section 5.3.1 where previous work by Hancock (1953) was cited for reference. In a more recent review on fluid dynamics, Lighthill (1996) also gives details of this force distribution. This representation of force distribution along a flagellum allows one to express the velocity induced by the whole flagellum as

$$u_j(\mathbf{x}) = \int_0^L \left[G_{jk}(\mathbf{x}, \mathbf{X}(s)) \frac{f_k(s)}{8\pi\mu} + D_{jk}(\mathbf{x}, \mathbf{X}(s)) \frac{d_k(s)}{4\pi} \right] \mathrm{d}s. \tag{5.16}$$

The functions $f_k(s)$ and $d_k(s)$ give the elements of the force's magnitude in direction k ($k = 1, 2, 3$, corresponding to the direction of the axes) for the stokeslet and the free field dipole, situated at a distance s along the flagellum where the total flagellum length is L, as introduced previously.

Calculating the induced velocity.

The expression for the velocity on the left hand side of equation (5.16) can be determined from partially differentiating the position vector given by

$$\mathbf{X} = (X, Y(X,t), Z(X,t)),$$

with respect to time, t, to give

$$\mathbf{u} = \frac{\partial \mathbf{X}}{\partial t} = \left(\frac{\partial X}{\partial t}, \frac{\partial}{\partial t} Y(X,t) + \frac{\partial}{\partial X} Y(X,t) \frac{\partial X}{\partial t}, \frac{\partial}{\partial t} Z(X,t) + \frac{\partial}{\partial X} Z(X,t) \frac{\partial X}{\partial t} \right). \tag{5.17}$$

All of the terms $\frac{\partial Y}{\partial t}$, $\frac{\partial Y}{\partial X}$, $\frac{\partial Z}{\partial t}$ and $\frac{\partial Z}{\partial X}$ are calculated from equation (5.2) by simply differentiating the equation defining the flagellum centre-line. However, the term $\frac{\partial X}{\partial t}$ uses more involved calculations in most cases. For the case when one considers a fixed helix rotating with no net motion of the helix in the X direction, i.e. points on the helix rotate on a fixed circle, then we can state that $\frac{\partial X}{\partial t} = 0$ (implying no movement in the X direction).

An alternative case would be if we chose to introduce an equation for the flagellum where any point at a distance s along the flagellum is not rotating in a fixed circle. In this case we would see $\frac{\partial X}{\partial t}$ does not equal zero. For example, if we did not have the tip of the flagellum (or any other points along the flagellum) moving round in a fixed circle, but instead introduce an elliptical relation between the Y- and Z-coordinates, then we would see an upwards and downwards motion of the tip. In this case, it will not only be the flagellum tip which moves up and down, but also all the other points situated along the flagellum. This means that with time there would be a variation in the displacement in the X direction, hence giving an illustrative case where $\frac{\partial X}{\partial t}$ can be non-zero. Therefore we proceed with the derivation of the term $\frac{\partial X}{\partial t}$ for completeness. From equation (5.3), which specifies the arc length, we can partially differentiate both sides with respect to t which yields the equation

$$\frac{\partial X}{\partial t} = -\frac{1}{\left[1+\left(\frac{\partial Y}{\partial X}\right)^2+\left(\frac{\partial Z}{\partial X}\right)^2\right]} \int_{X_0}^{X} \frac{\frac{\partial Y}{\partial X}\frac{\partial^2 Y}{\partial X \partial t}+\frac{\partial Z}{\partial X}\frac{\partial^2 Z}{\partial X \partial t}}{\left[1+\left(\frac{\partial Y}{\partial X}\right)^2+\left(\frac{\partial Z}{\partial X}\right)^2\right]}\,\mathrm{d}X, \qquad (5.18)$$

where all the elements under the integral sign can be calculated. Hence, by using numerical integration we can obtain an expression for $\frac{\partial X}{\partial t}$ at any given point s along the flagellum and therefore the velocity of any point on the flagellum. This calculation is carried out in Higdon (1979*a*) for the planar wave but due to the above mentioned reason is not necessary in Higdon (1979*c*) where the study is concerned with the case of a fixed helix.

In equation (5.16), the terms which are unknown are those which give the force of

the stokeslets and dipoles, denoted by $\mathbf{f}$ and $\mathbf{d}$ respectively. Therefore, determining these forces at each time step by satisfying the boundary conditions (which are specified later in section 5.3.5), we can calculate the velocity induced at any point $\mathbf{x}$ within space due to the total force of the beating flagellum. This will allow any particle we choose to be followed in its progression through the fluid surrounding the typical model organism. This is important because it gives results which allow a comparison with the particle paths observed experimentally (presented in Pettitt (2000)).

Before looking at the final solution for $\mathbf{f}$ derived from satisfying the boundary conditions, there is a relation between the forces created by the stokeslets and the dipoles which we can utilise. In Higdon (1979*a*) it was stated that the dipole strength was determined by the component of the stokeslet normal to the centre-line. This gives the relation

$$d_k = \frac{-a^2}{4\mu}(\delta_{kl} - T_k T_l) f_l, \tag{5.19}$$

where $\mathbf{T}$ is defined as the unit tangent vector to the flagellum. Therefore, we can rewrite equation (5.16) so that it only contains one unknown which we have to find, that is $f_k(s_i)$ which gives the force on the s_i^{th} segment of the flagellum in the k^{th} direction (for $k = 1, 2, 3$). An excellent explanation is given in Lighthill (1996) into how this relationship is derived due to the distribution of stokeslets and dipoles along the centre-line of the flagellum, and the reader is referred there for more detail.

Since the boundary condition requires that the induced velocity created by the flagellum on its surface is equal to the velocity at which the flagellum beats, we can use equation (5.16) (in a rewritten format expressed by equation (5.21)) and the fact that $\dfrac{\partial X}{\partial t} = 0$ for this fixed helical beat pattern to find the unknown $\mathbf{f}$. We solve this set of equations numerically using integration methods and MatLab software.

5.3.5 Solving to find the force, f

Firstly, we rewrite equation (5.16) so that the right hand side (as well as being only in terms of $f_k(s)$) is now in terms of the known expressions for the singularities which were introduced at the beginning of section 5.3.2. This will allow us to numerically calculate the terms within equation (5.16) and then manipulate them to perform a numerical matrix inversion determining the unknown forces $f_k(s_i)$ (for $k = 1, 2, 3$) for each position s_i along the flagellum.

We use the boundary condition on the flagellum to allow the evaluation of the left hand side of equation (5.16), i.e. the velocity of the fluid on the flagellum surface equals the velocity of the flagellum surface. Because we are looking at a distribution of stokeslets and dipoles along the flagellum centre-line, it is appropriate to consider this boundary condition at points along the centre-line instead of at the surface. The boundary conditions on the flagellum centre-line define a set of values which we can use to enable the numerical calculation of the Green's functions. The various Green's functions require both the coordinates where the forces distributed along the flagellum are acting and the coordinates of the point at which we are interested in recording the effects of the force. This is achieved by breaking the flagellum into 'segments', typically linear with end points at s_i and s_{i+1}, and calculating the force on each of them. This has been explained in section 5.3.1 where we introduced the notation of s_i^m for the midpoint of the i^{th} segment.

By defining S_{jk}^{ϕ} as the sum of the image terms in equation (5.15), we can use the definition given in Higdon (1979*a*), to re-express the relation involving the Green's function as

$$S_{jk}^{\phi}(\mathbf{x}, \mathbf{y}) = G_{jk}(\mathbf{x}, \mathbf{y}) - S_{jk}(\mathbf{x}, \mathbf{y}). \tag{5.20}$$

Higdon's reason for this definition was to separate the image terms (included in equation (5.15)) into those which required numerical integration (the terms from expressions (D.1), (E.1) and (E.2)) and leave the remaining terms to be analytically integrated. In our case, this separation of the terms helps breakdown the numerical problem to be tackled because

for our current purpose we are not interested in the analytical evaluation of the terms under the integral. Each of the terms in equation (5.20) has been interpreted within the preceding sections and this makes it easier to evaluate them numerically for a large number of variables.

We will numerically integrate equation (5.16) which leads to some rewriting before the computer code can be fully assembled. The definition from equation (5.20) allows (5.16) to be rewritten as

$$u_j(\mathbf{x}) = \int_0^L \left\{ \left[S_{jk}(\mathbf{x}, \mathbf{X}(s)) + S^{\phi}_{jk}(\mathbf{x}, \mathbf{X}(s)) \right] \frac{f_k(s)}{8\pi\mu} + D_{jk}(\mathbf{x}, \mathbf{X}(s)) \frac{d_k(s)}{4\pi} \right\} \mathrm{d}s. \qquad (5.21)$$

Following Higdon (1979*a*), we then split the flagellum length into N equal segments and within each we assume the force of the stokeslet, $\mathbf{f}$, is constant. This force will give a fixed value for each specific time during the beat cycle, say $t = T$, and so it is necessary to consider an iteration process for each individual time step over which the flagellum beats. This is obviously due to the distribution of forces changing at each time step. If we can reduce the effort that it takes to estimate the force distribution due to the large number of calculations required, the computational time will be kept to a minimum.

One method by which we can determine the force distribution whilst minimising the amount of computational time, but not reducing the accuracy, is via an alternative representation of the physical system. Physically, we have presented the model to be one composed of a fixed plane and cell body in relation to a moving flagellum. Since it is 'expensive' to move the flagellum with every time step due to recalculating the forces that are associated with each beat, we can consider the analogous problem of rotating the plane and the cell body in synchrony whilst keeping the flagellum fixed. Because both a sphere (representing the cell body) and a plane (representing the substrate) are rotationally symmetric, then satisfying their boundary conditions will only involve a simple rotation for any given time. Hence one only needs to consider the velocity of their boundaries with respect to the fluid through which they move. When the sphere and plane

are both fixed, we require the velocity on the boundaries to equal zero. This is because we need the no-slip condition at both these surfaces to be satisfied. Once one begins to rotate the sphere and the plane together through the fluid, the velocity on their surfaces will no longer be zero. The flagellum, which we considered to be moving in the original representation of the problem, will have the velocity of its surface equal to the velocity of the fluid at the surface. Once the flagellum is fixed, then the analogous condition is zero velocity at the surface of the flagellum for every fixed time step. The conditions for the original problem are given below by equation (5.25) after a detailed explanation of how one evaluates the forces within the problem. In the second case where one fixes the flagellum and rotates the cell body and plane, these boundary conditions which are satisfied in equation (5.25) are altered so that in the frame rotating with the flagellum will see the plane and cell body moving with the rotational velocity of the flagellum. We define the angular velocity of the flagellum by $\boldsymbol{\omega} = (\omega, 0, 0)$.

We now proceed to explain how we solve to find the force for any given time and then incorporate the details of the rotating system later within section 5.3.6. As previously mentioned, we can relate the forces created due to the singularities (f_k) and those due to the dipoles (d_k) via the relation given in equation (5.19). Therefore, we only need to consider solving the equations which satisfy the boundary conditions for f_k.

Considering the term S^{ϕ}_{jk} given in equation (5.20), we look at any n^{th} interval and more specifically the integral over its small segment length which is given by

$$H_{jk}(\mathbf{x}, \mathbf{X}(s_n)) = \frac{1}{8\pi\mu} \int_{s_n^m - \delta s_n}^{s_n^m + \delta s_n} S^{\phi}_{jk}(\mathbf{x}, \mathbf{X}(s))\, \mathrm{d}s, \tag{5.22}$$

where Higdon states this integration needs to be evaluated numerically. The length of the segment is $2\delta s_n$, which is taken to be small. To evaluate the induced velocity when considering the N intervals requires a summation over all of the N segments along the total length of the flagellum for all the terms H_{jk}, plus the other terms which equation (5.21) can be decomposed into. For this reason we also choose to express the remainder of

equation (5.21) in terms of the n^{th} interval, to allow the summation over the N segments for all terms to give the value of the velocity. Equation (5.22) has dealt with the term S^{o}_{jk}, so we now examine an expression for the other terms in equation (5.21), S_{jk} and D_{jk}, which we require in a similar format. By using equation (5.19) to express d_k as a function of f_k, we reduce the problem to one where we are only required to solve for the force f_k. Notice it is important that the subscripts in this expression for f_k are kept in good order. If we define

$$K_{jk} = \frac{1}{8\pi\mu}\left(\int_{s_n^m-\delta s_n}^{s_n^m+\delta s_n} S_{jk}(\mathbf{x},\mathbf{X}(s))\,\mathrm{d}s - \frac{a^2}{2}(\delta_{kl}-T_lT_k) \int_{s_n^m-\delta s_n}^{s_n^m+\delta s_n} D_{jl}(\mathbf{x},\mathbf{X}(s))\,\mathrm{d}s \right), \quad (5.23)$$

then this allows us to write down a simple equation re-expressing equation (5.21) as the summation:

$$u_j(\mathbf{x}) = \sum_{n=1}^{N} \left\{ \left[K_{jk}(\mathbf{x},\mathbf{X}(s_n)) + H_{jk}(\mathbf{x},\mathbf{X}(s_n)) \right] f_k(s_n) \right\}, \quad (5.24)$$

with f_k the value of the unknown force which we will determine.

Notice that expression (5.19), given by Higdon (1979*a*), merely gives a simplified method with which to consider the force distribution. We are considering the force on a small interval whose effects become negligible compared to the rest of the forces along the flagellum, see Hancock (1953). Once we have reached this stage, we have an expression (which can be obtained numerically) to give the velocity induced by the singularity distributions along the flagellum, including the images in both the plane and the sphere. The final stage in the process of determining the values of f_k is to substitute in for the boundary conditions on the flagellum so that one can evaluate the Green's functions and the flagellum velocity. The numerical scheme can then be implemented once we have only one unknown set of variables, f_k. Using a matrix inversion technique, rather than the iteration method which Higdon pursued, we are able to calculate the values of f_k for each segment along the flagellum. Notice that we take values of forces to act at the midpoints of each segment, i.e. each s_i^m is defined for each $i = 1, .., N$, because the force is regarded

as constant over the length of a segment.

The boundary condition on the flagellum has been stated such that the induced velocity with which the flagellum centre-line moves equals the actual velocity of the fluid on the flagellum surface. Hence, equation (5.24) above can be re-expressed to satisfy the boundary conditions on the flagellum as

$$u_j(\mathbf{X}(s_q^m)) = \sum_{n=1}^{N} \left\{ \left[K_{jk}(\mathbf{X}(s_q^m), \mathbf{X}(s_n)) + H_{jk}(\mathbf{X}(s_q^m), \mathbf{X}(s_n)) \right] f_k(s_n) \right\}. \tag{5.25}$$

Because the length of each segment is not infinitely small in this instance, we take the midpoint of an interval to be the position at which the induced velocity is calculated. This midpoint, for any q^{th} interval, is denoted as $\mathbf{X}(s_q^m)$ within the cartesian coordinate system.

Since the velocity of the flagellum centre-line is given by equation (5.17) when $\mathbf{X} = \mathbf{X}(s_q^m)$, this must also give the left hand side of equation (5.25) by the definition of the no-slip boundary condition. The terms on the right hand side of equation (5.25) are easily calculated because we can express the Green's functions numerically for any coordinates $\mathbf{X}(s_q^m)$ from the singularities and image system expressions we have previously stated. It is helpful to express the elements within the summation term as

$$Q_{jk}(s_q^m, s_n) = K_{jk}(\mathbf{X}(s_q^m), \mathbf{X}(s_n)) + H_{jk}(\mathbf{X}(s_q^m), \mathbf{X}(s_n)), \tag{5.26}$$

which we later refer to when we investigate the solution via matrix inversion, see Appendix F for details.

The remaining work is involved in rearranging equation (5.25) so that we can determine the unknown values of the forces created by the flagellum. The main disadvantage with the method of rearranging equation (5.25) referred to in Higdon (1979*a*) was concerned with separating the forces from the other known values within the equation to achieve a convergent result. In our case, we chose to perform the method of matrix inversion on the system to eliminate the problem with convergence. Representing the force and the

velocity at the given points along the flagellum by two vectors, the summation term given in equation (5.25) can be represented as a matrix which can therefore be inverted. Hence for each time step, once we have calculated the known terms on the right hand side of equation (5.25) and then inverted the matrix which we call $\mathbf{Q}$, from equation (5.26), we can determine the value of $\mathbf{f}$ by simple matrix multiplication. As mentioned previously, because we need to know the value of the forces for each beat of the flagellum, this could be the area of numerics which could be most computationally expensive. Hence, performing this matrix evaluation only once would be beneficial.

The final step, once the value of the force is known, involves reverting back to equation (5.24), which we can solve for any given point within the system now all the terms on the right hand side are either defined or can be calculated. Once the velocity is known from (5.24), the particle position is calculated at each time step using an Eulerian scheme. Hence a simplistic representation can be given as

$$\mathbf{x}_{\text{new}} = \mathbf{x}_{\text{old}} + \mathbf{v}(\mathbf{x}_{\text{old}})\delta t, \tag{5.27}$$

where δt represents the small time step between each movement of the flagellum and $\mathbf{v}(\mathbf{x})$ is the velocity at position $\mathbf{x}$. The velocity used in equation (5.27) is the value which can be calculated from equation (5.24). This Eulerian formulation will require the calculation of the velocity at each specific time we are interested in. Therefore, once the forces have been derived for the flagellum centre-line at the particular time of interest, we are able to calculate the velocity acting on any given point at that particular time. The values for the initial point, $\mathbf{x}_{\text{old}}$, and the time step δt which are used within (5.27) are either stated in the initial conditions of the model, or in the case of $\mathbf{x}_{\text{old}}$, known from the preceding calculation. Repeating this process allows one to trace a particles position over many periods of the beat by storing the values of $\mathbf{x}_{\text{new}}$ over any length of time.

5.3.6 Particle paths - fixed and rotating coordinate frames

We now proceed to illustrate changing the coordinate systems (which is explained with the aid of diagrams) as a method to reduce the time taken to find the particle paths around the model organism we have presented.

We study two coordinate axes, a rotating frame and a body frame, whose origins and vertical axes are coincident. These are illustrated in Figure 5.4 (c). The rotating frame is taken to be fixed with respect to the flagellum and the coordinates of general points in this frame are given by $\mathbf{X}'$. The body frame, with coordinates labelled as $\mathbf{X}$, is fixed with respect to the cell body and the plane. Therefore, when we are situated within the body frame, the flagellum appears to be rotating about the vertical axis with an angular velocity $\boldsymbol{\omega}$. As noted above, the vertical axes are coincident for both the systems so we can regard this axis as fixed. This reduces the dimensions of the problem by one degree when we move between the rotating frame and the body frame. This transformation is required each time we move between the two reference frames. The transformation matrix is defined by

$$\mathbf{T}(\vartheta) = \begin{pmatrix} 1 & 0 & 0 \\ 0 & \cos\vartheta & -\sin\vartheta \\ 0 & \sin\vartheta & \cos\vartheta \end{pmatrix} \quad \text{with} \quad \mathbf{X}' = \mathbf{T}(\vartheta)\mathbf{X},$$

giving the coordinates in the rotating frame ($\mathbf{X}'$) from the coordinates of the body frame ($\mathbf{X}$). The rotation angle here is $\vartheta(= \omega t)$. The transformation back from the rotating to the body frame simply replaces ϑ with $-\vartheta$ in the matrix $\mathbf{T}$.

Equation (5.25) will give the solution for $\mathbf{f}$ along the flagellum by satisfying the boundary conditions along the centre-line by matrix inversion, as previously explained. Only one set of solutions is required within the rotating frame because, with respect to this frame the flagellum is always fixed. Hence, we can always find the velocity the flagellum will induce on a particle whose position is described by coordinates within the rotating frame, once we know the solution for the force distribution within the rotating frame.

To follow the global motion of the particle with respect to a fixed reference point such as the origin, it is necessary to know the position of the particle within the body frame which we have dubbed the fixed frame. One must calculate the particle positions within the rotating frame because this is where the force is evaluated. These points must be translated to the fixed frame of reference for the cell body to obtain a true picture of the trajectory as observed in the experimental studies of Pettitt (2000).

Translation from the fixed to rotating frame will take the form $\mathbf{X}' = \mathbf{T}(\vartheta)\mathbf{X}$, where $\mathbf{X}'$ gives the particle's position in the rotating frame which can then be acted upon by the velocity field due to the flagellum. We assume $\mathbf{X}'$ moves to $\mathbf{X}' + \delta\mathbf{X}'$ under the action of this force. This is the new position in the rotating system which we need to translate back to the body frame. If we have moved through an angle ωt since the start of the motion (equivalent to $\vartheta(t)$ in expression (5.2)), then we use

$$\mathbf{X}_{\text{NEW}} = \mathbf{T}(-\omega t)[\mathbf{X}' + \delta\mathbf{X}'],$$

to give the position of the particle in the body frame. From here, we use the particles position with respect to the body frame to begin to construct the particle's trajectory. We finally must find the position of the particle within the rotating frame which has moved through a further displacement of $\omega\,\delta t$. Hence repeating the translation into the rotating frame gives

$$\mathbf{X}'_{\text{NEW}} = \mathbf{T}(\omega(t + \delta t))\mathbf{X}_{\text{NEW}}.$$

This is explained further with reference to Figure 5.5 which looks at a two-dimensional section of the three-dimensional space. This final translation step is a subtle difference, but shows how one cannot simply consider the effect the force has on the points within the rotating frame alone.

As well as examining the translating axes, we will also need to look at the alterations required within the previously stated boundary conditions. It is important to notice that we must always be solving the same physical system, even if the relative geometry

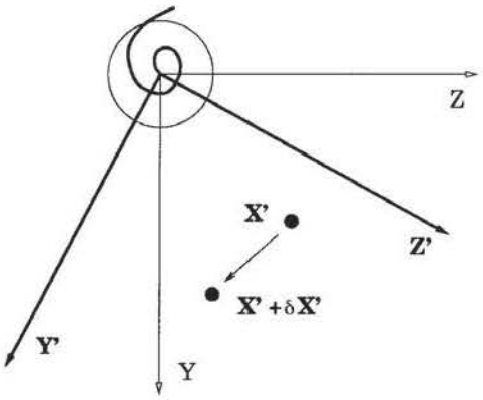

Fig. 5.5 (a) The action of the flagellum moves the point from $\mathbf{X}'$ to $\mathbf{X}' + \delta\mathbf{X}'$ in the rotating frame. This must be translated to the body frame before being plotted as part of the trajectory.

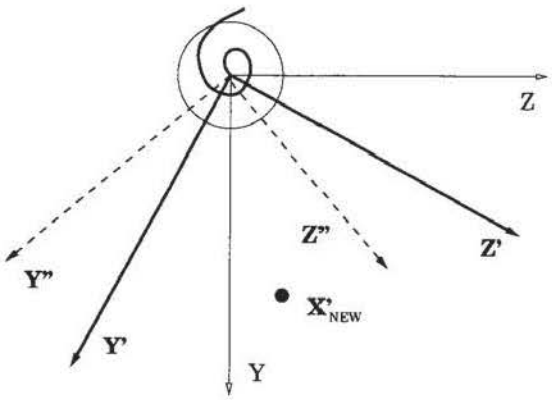

Fig. 5.5 (b) With a further rotation of the flagellum axes prior to the force acting, a translation of the point within the rotating frame is required.

Figure 5.5: A view down the flagellum axis onto a two-dimensional plane showing the cell body and the rotating coordinate frames.

one is using to describe it has changed. This is because approaching the problem using rotating coordinates gives an alternative view of the initial geometrical interpretation of the boundary conditions. Restating equation (5.25) for the velocity of the flagellum:

$$u_j(\mathbf{X}(s_q^m)) = \sum_{n=1}^{N} \left\{ \left[K_{jk}(\mathbf{X}(s_q^m), \mathbf{X}(s_n)) + H_{jk}(\mathbf{X}(s_q^m), \mathbf{X}(s_n)) \right] f_k(s_n) \right\},$$

we notice we are satisfying the boundary conditions where one regards the sphere and the plane to be stationary. We can consider a simplified representation of the velocities within the problem as

$$\mathbf{V}_F = \mathbf{V}_B - \boldsymbol{\omega} \times \mathbf{X},$$

where $\mathbf{V}_F$ is the velocity on the flagellum, and $\mathbf{V}_B$ is the velocity of the body frame. Hence since the body frame is fixed, we can simply alter equation (5.25) to satisfy the boundary conditions within the rotating frame giving:

$$u_j(\mathbf{X}(s_q^m)) = -\left(\boldsymbol{\omega} \times \mathbf{X}(s_q^m)\right)_j + \sum_{n=1}^{N} \left\{ \left[K_{jk}(\mathbf{X}(s_q^m), \mathbf{X}(s_n)) + H_{jk}(\mathbf{X}(s_q^m), \mathbf{X}(s_n)) \right] f_k(s_n) \right\},$$

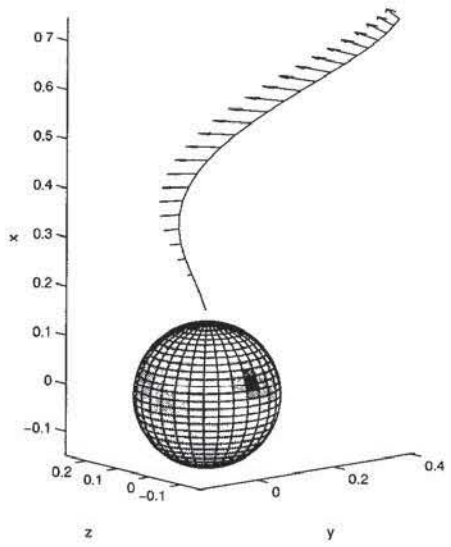

Figure 5.6: The graph illustrates the velocity components positioned along the centre-line of the flagellum with the sphere representing the position of the cell body. Within this non-dimensionalised representation, the sphere has diameter 0.2 units, the flagellum has length 1.0 unit whilst the substrate (not shown here) is parallel to the $y-z$ plane and cuts the x-axis at 0.9 units below the origin.

which can be solved by a simple matrix inversion to find the forces along the flagellum.

5.4 Results

This section will aim to illustrate some of the similarities between the numerical calculations of particle paths and experimental results found in Pettitt (2000). First, we present a few results concerning the action of the flagellum and then move on to look at a number of paths a tracer particle follows for a variety of different sets of parameters. Throughout this section we define the curve using the parameters: $\alpha^* = 0.4$, $k = -4$ and $\vartheta = 4$ in equation (5.2). Every five time steps the flagellum moves in the numerical code is equivalent to 0.02 seconds as recorded from experimental data, Pettitt (2000).

Figure 5.6 illustrates the velocity on the surface of the flagellum at a nominal time during a period of the beat. The forces created by the flagellum can be illustrated in a similar manner to this velocity graph as Figure 5.2 in section 5.3.1 has illustrated. We can see by comparing the two figures that the velocity arrows show the direction and speed

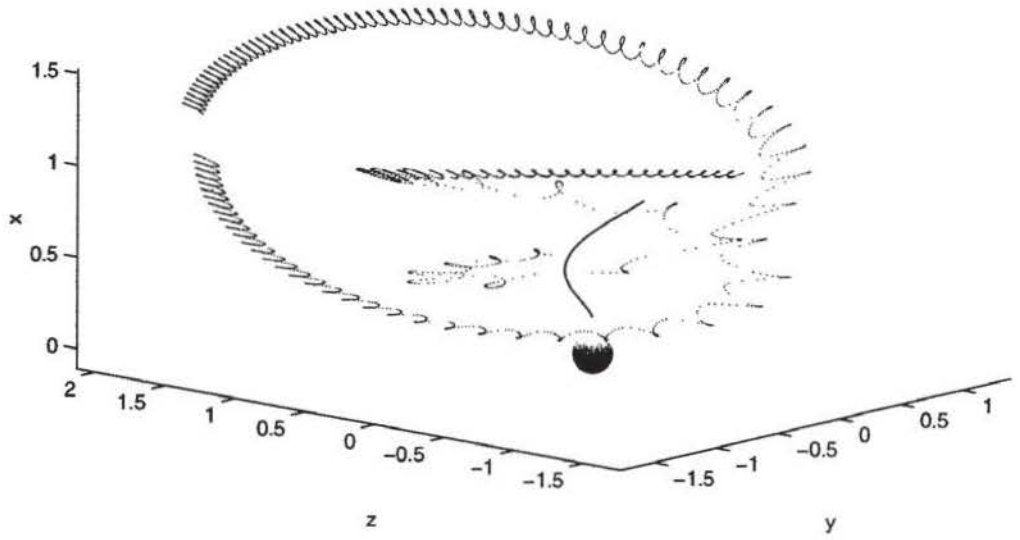

Fig. 5.7 (a) The particle paths taken by two particles around the cell body and the flagellum. Notice the eddies creating a continuous recirculation of particles and the larger velocities close to the flagellum.

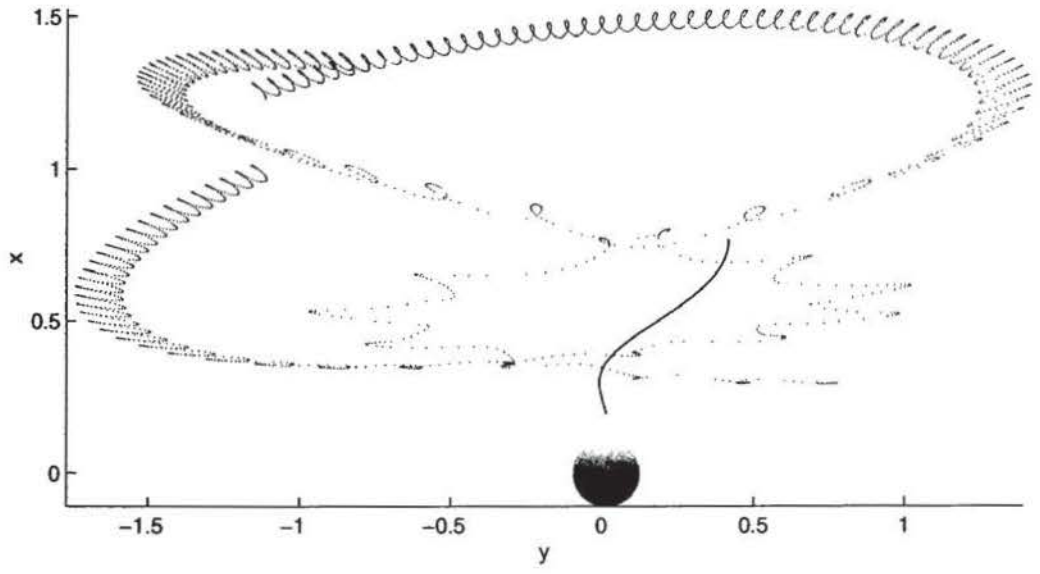

Fig. 5.7 (b) A view along the z-axis at a projection of the previous subfigure on to a two-dimensional plane. The eddies are now clearer. We see an elongation of the eddies horizontally and we should notice the axes are equal.

Figure 5.7: The graphics display the trajectory of particles over time and illustrate the recirculation of tracers seen within the fluid. Within each figure, a representation of a scaled sphere and flagellum is given for completeness. For this particular case, the parameters used are for the control organism in Table 5.1. The substrate would be situated 0.9 units below the origin for both figures. Figure 5.8 shows trajectories for another organism observed within an experimental situation.

with which the flagellum moves. It is the forces created along the flagellum which will ultimately affect any particle or tracer within the flow. As one can see from Figure 5.2, the relationship between the forces created by the flagellum and the particle will not be simple because of the effects of curvature and the velocity fields associated with stokeslets and dipoles. By studying figures similar to Figure 5.6 and examining the magnitude of the velocity at points along the flagellum, we know the magnitude will remain the same throughout the problem so that the velocity only changes in direction due to the translation of the flagellum. It will only be the particles position with respect to the body frame which feels both the effects of rotation and the change in direction of the flagellum velocity. This implies Figure 5.6 could illustrate any time during a period of the cycle if we are situated within the frame rotating with the flagellum.

We want to investigate a representation of particle paths which will allow constructive comparison of numerical results with experimental results. For both, there are a number of cases we choose to consider, each of which will be relevant to a different species or size of choanoflagellate (as represented in Tables 5.1 and 5.2). The main goal will be to illustrate the paths which tracers can take due to the flagellum beating in a viscous fluid in the presence of a sphere and a plane. We will be able to show how the numerics replicate the patterns one sees in experimental observations via a select number of figures. The comparisons of path lines will be dependent on the dimensions of the relevant organism and so we consider a various number of parameters. One should note that the effect of the collar is not present within these calculations, but one could consider its virtual situation within the fluid. This would enable us to obtain results about the interception of tracers with the collar along similar lines to the study of Berg & Purcell (1977). It could create an interesting extension to the model we have studied and would represent a significant advance on the work presented here.

We present illustrations taken from experimental recordings and numerical interpretations of particle paths. By comparing and contrasting these results, we will highlight the interesting features of the flow. Figure 5.8 is a sketch taken from a video of an experiment

which observed a number of SA feeding. It shows an experimental result corresponding to organism C whose dimensions are included within Table 5.1. The particle paths are traced by the polystyrene spheres which have been introduced into the flow. The position of the tracers are recorded at a given time increment. Within the figure, the position of the specific choanoflagellate which creates the flow we are observing is included. This type of recording gives a two-dimensional representation of what is truly a three-dimensional process. This will mean the loss of some accuracy from the results when we want to compare these video images with those generated from our numerical model which are obviously fully three dimensional. As a method of analysing the numerical results to obtain the most ideal comparison with experimental recordings, we can adopt a strategy which examines 'slices' of the flow field. We assume this to be similar to the limited depth of vision one can record when observing a three-dimensional flow under a microscope. Therefore, Figure 5.9 which illustrates the results of the numerically generated particle paths shows two different perspectives. First, it gives a fully three-dimensional representation so that the flagellum shape and cell body can be clearly seen. Also within the figure is a slice of the three-dimensional space. We take the depth of the slice to be approximately twice the cell body diameter. This is shown as a plane representation, similar to the view one would see down a microscope. We feel this gives a good interpretation and illustration of some of the path lines which are taken by a number of tracers.

We now look in more detail at the numerical representations of particle paths (Figures 5.7 and 5.9) for the specific dimensions of the organisms labelled 'control' and 'Org. C' in Table 5.1. Altogether there are three cases motivated by experimental results (columns two to seven in Table 5.1) and one set of control parameters which was used purely for numerical methods (column one in Table 5.1). Comparing the four columns all showing non-dimensionalised results for SA (given by the heading 'Non-dim.' in Table 5.1), one can see the first test set (called the control) is representative of the case where the cell body is positioned approximately one flagellum length from the substrate. The other three cases look at a range of parameters where the substrate distance from the flagellum

	Non-dim. control	Org. A (μm)	Non-dim. Org. A	Org. B (μm)	Non-dim. Org. B	Org. C (μm)	Non-dim. Org. C
Flagellum radius	0.01	0.4	0.02	0.4	0.03	0.4	0.01
Cell body radius	0.1	2.5	0.13	2.4	0.15	2.5	0.17
Flagellum length	1	19.2	1	15.8	1	11.4	1
Height above substrate	0.9	11.4	0.46	8.8	0.56	6.4	0.22

Table 5.1: Dimensions of SA as taken from experimental results by Pettitt (2000) for one control and three living organisms with a variety of physically different parameters. For each organism (A, B and C) we show the dimensions in micrometres (μm) and the non-dimensionalised lengths in the adjacent column.

	Control	Org. A	Org. B	Org. C
a/A	0.1	0.16	0.17	0.16
L/A	10	7.68	6.58	4.56
H/A	9	4.56	3.67	2.56

Table 5.2: Ratios of the organism's parameters as used by Higdon (1979*a*) with: a the flagellum radius, A the cell body radius, L the length of the flagellum and H the distance of the centre of the cell body above the substrate.

is smaller in comparison to the associated flagellum lengths. It is possible to compare the ratios of the physical dimensions in a manner which would enable comparison with work in Higdon (1979*a*). These dimensions are shown in Table 5.2 where the relative dimensions of the organisms are given. We could contrast our results with work from Higdon (1979*a*) which looked at these ratios in order to compute efficiency and power parameters of the organisms. This would allow experimentalists to investigate both the efficiency and the path lines taken by particles around *in vitro* organisms.

We have taken measurements from Figure 5.8 to be compared with the paths generated by numerical methods involving an organism modelled with the same dimensions, presented in Figure 5.9. It will be unrealistic to compare these results solely by observation to see whether the features from the numerical simulation of particle paths agree

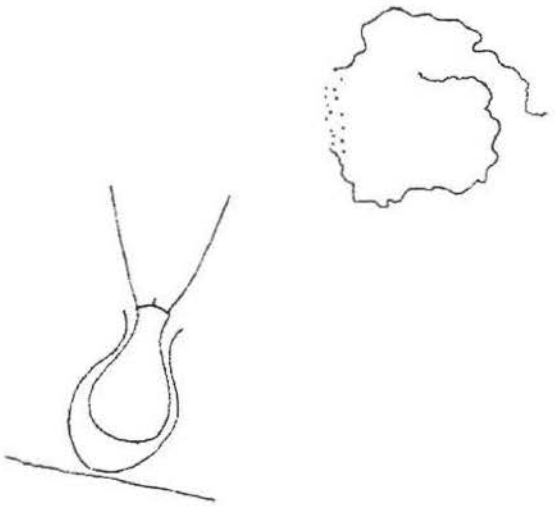

Figure 5.8: The outline of a specific SA (organism C in Table 5.1) and a trajectory of a specific particle path taken from experimental observations.

with those found in experimental results. Therefore, we take measurements of the size of the eddies created, their location and the behaviour of particles from a number of different regions around the organism. This requires investigating trajectories which are started in accordance with experimental results hence creating a basis for numerical procedures when we begin to generate realistic particle paths. The measurements given within Table 5.3 show how we start to look at comparisons between experimental and numerical results. We have included measurements for various organisms (as presented in Table 5.1) but only include figures for organism C. The measurements are in non-dimensionalised form with respect to the distance from the substrate to the base of the flagellum (H^*). We use H^* because this distance can be easily measured from the experimental records and is readily available from the numerics. We have found good agreement between size and position of eddies created by our numerical model compared to experimental observations. Referring to both Figure 5.9 and Table 5.3, notice how the eddies (the zig-zag patterns created as the particle moves) from the numerical results are all slightly larger than those found under experimental conditions. This could be due to the affects of a greater viscosity of fluid or the presence of the collar within the physical system which retards the motion of the particles. The experimental results are captured at time steps due to the type of

	Experimental		Numerical		
	Eddy width	Eddy length	Eddy width	Eddy length	Distance of eddy from flagellum base
Org.A	0.11	0.07	0.25	0.64	1.07
Org.B	0.15	0.11	0.21	0.21	2.17
Org.C	0.26	0.37	0.31	0.54	0.74

Table 5.3: Non-dimensionalised measurements of specific eddies created around three organisms whose flow patterns we investigate. The measurements have been non-dimensionalised with respect to H^* (the distance between the substrate and flagellum base) allowing comparison between experimental and numerical results. Width and length are interchangeable and merely suggest measurements taken in two mutually perpendicular directions. The distance of the eddy from flagellum base is the same for both sets of results to facilitate comparisons of the correct eddy measurements.

recording apparatus used. This shows fewer steps between each particle movement so that the tracer appears to jump between one line and another. With the numerics however, the smaller time steps used allow for a more complete picture in which the particles move in a continuous manner. For example, to recreate the experimental recordings close to the flagellum, we would only be required to sample the particle position every fifth time step from the numerical results.

We have also looked at larger eddies (mainly responsible for recirculating fluid) which consist of many of the smaller eddies whose typical dimensions are displayed in Table 5.3. Again, eddies created via numerical methods are of a similar size and dimension to those from the experimental observations. These large eddies create the mixing which is of most interested from a biological viewpoint. They show the manner with which these organisms circulate fluid to obtain a supply of nutrients from the otherwise stationary fluid. Referring to Figure 5.10 one can see a numerical representation of these larger eddies obtained after several periods of the flagellum beat. Notice how the eddies formed tend to be spread in the horizontal direction more so than the vertical. The smaller zig-zag eddies further away from the flagellum also tend to be elongated in the horizontal direction, whereas close to the flagellum we see a marked vertical progression.

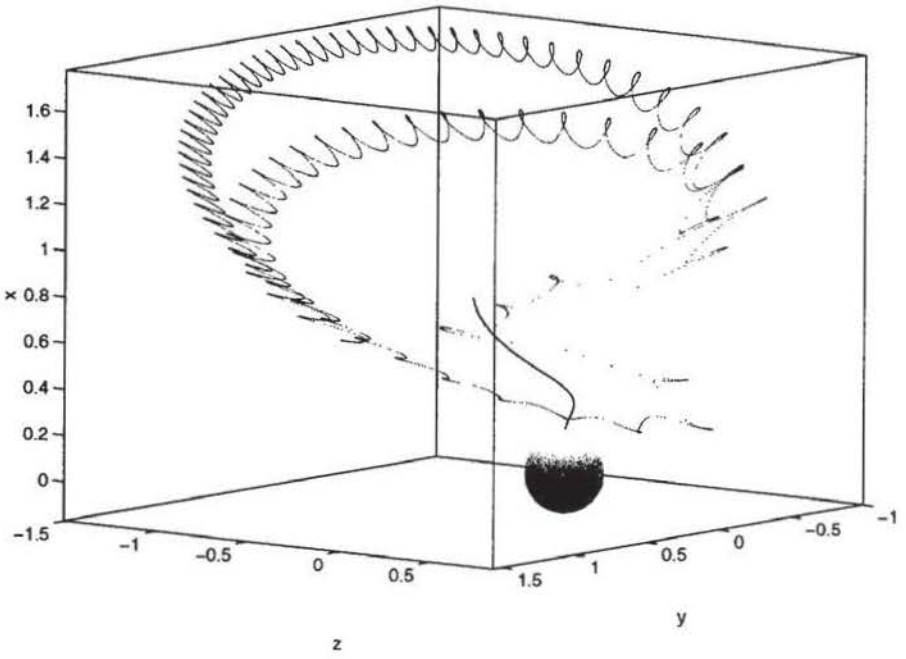

Fig. 5.9 (a) The particle paths taken by a particle around the cell body and the flagellum. This is over long time and shows the total three-dimensional representation including the eddies followed by the tracer.

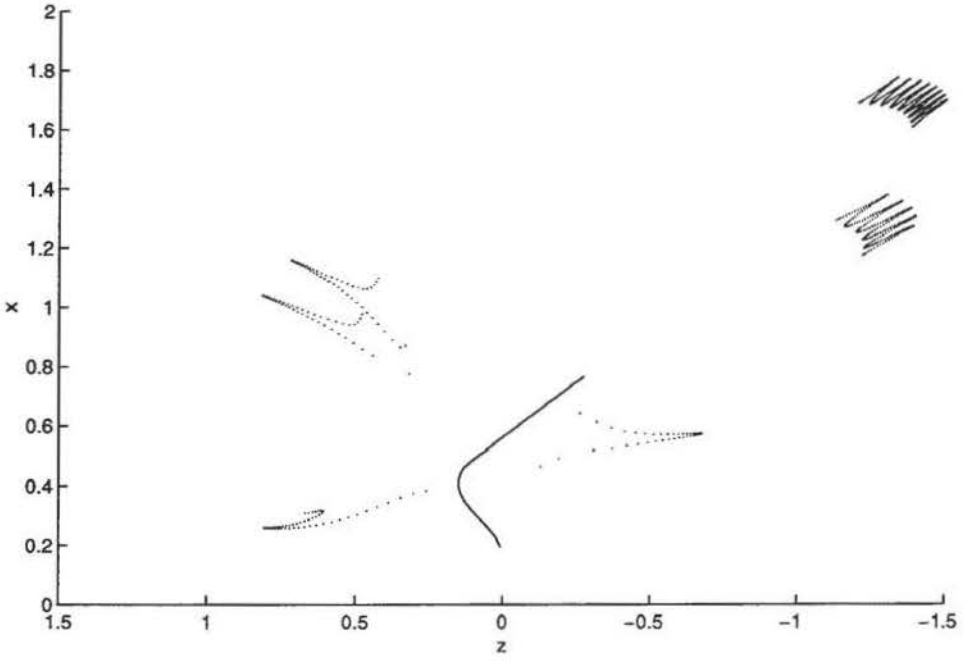

Fig. 5.9 (b) A graph showing the representation of a slice of the three-dimensional space. The slice is approximately twice as thick as the cell body diameter. The section of the flagellum seen within this slice is also represented at a particular time.

Figure 5.9: Graphics generated to show the recirculation of tracers seen within the fluid. This is for organism C whose dimensions are given in Table 5.1. The next figure gives the full two-dimensional projection rather than merely a slice of the results.

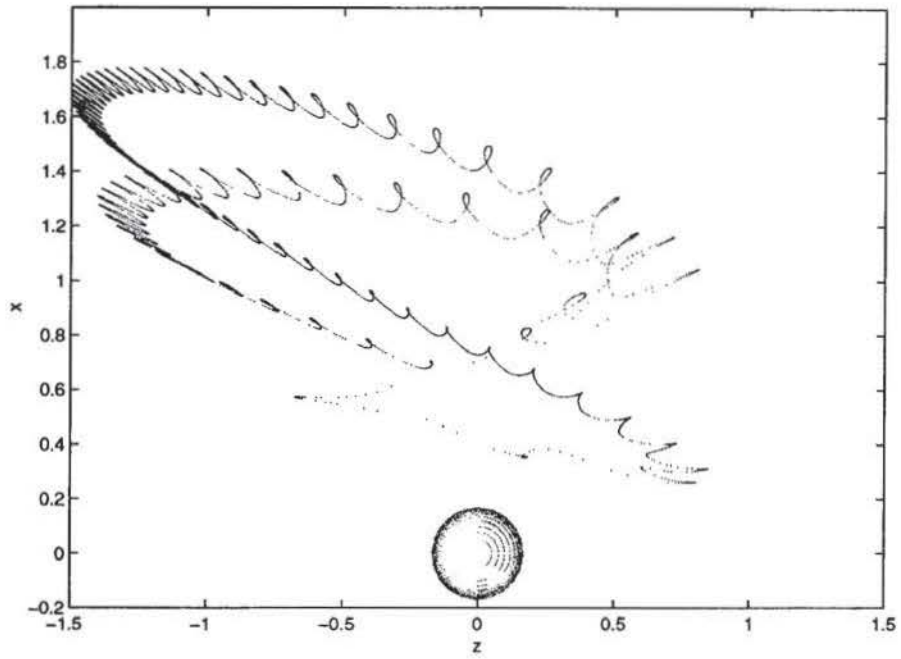

Figure 5.10: Graphics generated for organism C showing a two-dimensional projection of the three-dimensional numerics onto a plane. This creates an image similar to the representation recorded from experimental observations.

We investigate the amount of spreading from various regions by a method which looks at a number of points clustered a given distance from the flagellum and compare the divergence of the trajectories within each such region. We typically take two starting points separated by the distance of one flagellum radius (taken as small) in two of the three coordinate directions. The particles are allowed to move through ten periods of the flagellum beat cycle before we investigate their divergence from one another. The three regions we study around organism C occur at approximately the same vertical position as the flagellum tip and horizontally are positioned in the near, middle and far fields. Table 5.4 gives the average separation of these trajectories calculated by the general mean, along with details of their initial positions relating to the three regions described. The graph given in Figure 5.11 shows how the magnitude of the separation of trajectories changes over ten periods of the beat. This reinforces the data from Table 5.4 because we can see that particles typically situated within the midfield around the flagellum diverge to a greater extent horizontally than vertically. This suggests that particles from this region are most likely to experience more mixing than if they began in either the near or far

		X	Y	Z
Near	$y = 0.1$	0.0111	0.0133	0.0161
Mid.	$y = 0.35$	0.0074	0.0416	0.0325
Far	$y = 1.0$	0.0114	0.0159	0.0080

Table 5.4: The average displacement of the trajectories of two particles in the directions (X, Y, Z) with initial positions given by $(0.75\ ,\ y\ ,\ 0)$ and $(0.76\ ,\ y + 0.01\ ,\ 0)$ where y varies depending on the region, as given in the table. The trajectory is recorded over ten periods of the flagellar beat.

fields. This does not mean that particles in the near field will not experience significant motion. It merely shows that the trajectories for particles within the near field do not significantly diverge from one another. This could be due to the larger forces created near to the flagellum which do not allow the particles to deviate from a similar path line to their neighbours. In the opposite sense, the far field will not be significantly affected by the flagellum force. Therefore, particles here only move a small distance and will not have the ability to diverge from their neighbours. We refer to Blake (1971) where the image system for a stokeslet in a no-slip boundary was discussed. Results showed how the velocity and force fields are $O(r^{-2})$ for horizontal forces and $O(r^{-3})$ for forces in the vertical direction. Thus we would expect much stronger horizontal than vertical eddying motion which is evident from the particle paths, see Figure 5.10. Indeed, the 'loops' show features of a stresslet far field associated with the horizontal forces whereas the vertical forces are observed to have a weaker far field affect.

The reader should note the use of numerics within this section will allow further investigations to be undertaken by biologists or mathematicians alike. By using the numerical results in conjunction with biological experiments, it is possible for one to obtain a number of unknown variables from the physical organism or system as a whole. By generating particle paths found numerically for a certain set of length scales which describe the problem, one could compare these to experimental observations to find estimates of the unknown cell body radius, flagellum length or height above the substrate, once a

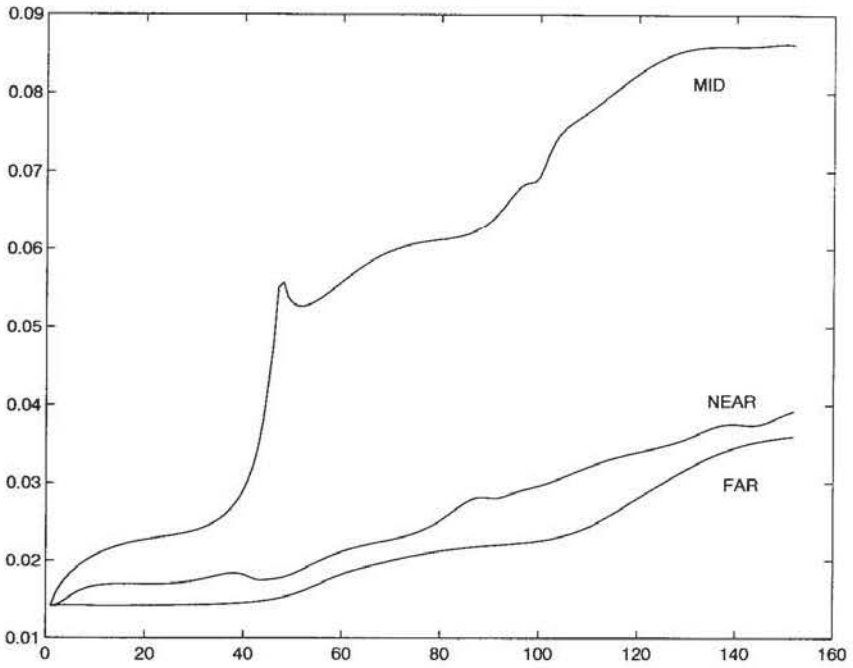

Figure 5.11: The distances two trajectories diverge for the three regions (near, middle and far) around the organism. The horizontal axis gives the non-dimensional time whilst the vertical axis shows the distance two particle paths diverge. Table 5.4 gives details of the initial location and separation of the particles.

variety of numerics have been developed. The work presented above also gives a basis for a mathematical model which could include the collar of the organism. This would increase the accuracy of the results and may enable the numerics to represent the experiments to an even greater degree of accuracy.

5.5 Discussion and conclusions

We have presented, after work by Higdon (1979*a*), a method using Green's functions to allow particle paths around a model organism to be generated. The model is a simplified representation of the substrate, cell body and flagellum by the use of a number of singularities along with their associated image systems. The collar is neglected (and the stalk is only present in a virtual sense) but this is believed to be a good model to represent the flow fields around such an organism.

We have shown our results compare favourably with experimental observations, there-

fore allowing the numerics to act as a tool for a variety of further investigations or studies. For example, the regions where the collar will be situated is seen to have a greater level of mixing than the far field. Influencing mixing of particles will be highly beneficial biologically. These results also compare well with theoretical work from Blake (1971) and Higdon (1979*a*).

Chapter 6

OVERALL SUMMARY AND FURTHER DEVELOPMENT

We aim to summarise this thesis by commenting on the results we have presented in primarily a mathematical and to a lesser extent biological context. We finish by indicating the directions we feel further work could take.

6.1 Summary

We began by investigating a model of the flow fields around the sessile choanoflagellate, *Salpingoeca Amphoridium* (SA), with a simple axisymmetric model, presented in Chapter 2. The low Reynolds' number of the flow, due to its viscous nature coupled with the microscopic nature of SA and its environment, allowed the use of the Stokes equations to model the flow. Extending the work of Otto et al. (2001), we considered an axisymmetric model which used stokeslets or point forces to replicate the flow fields. The novel planar case where the flow was created due to two horizontally displaced stokeslets acting perpendicular to an interface, was studied by the use of an implicit map. The problem allowed for the effects of the substrate to which the organism was attached via the consideration of a planar surface between two fluids, Aderogba & Blake (1978*a*). The construction of a map from a flow by the consideration of a delta function to replicate the pulsing of the force enabled the generation of results included in Chapter 3.

The planar case, considering the interaction of two stokeslets whose individual effects are axisymmetric, used both chaotic and statistical measures to study the degree of mixing of particles in the flow fields. Results from the study of Poincaré sections showed how changing the ratio of viscosities between the two fluids, θ, would determine how chaotic we found the motion of particles within the flow. Changing the value of α, which describes both the strength of the force and a time scale of the system, it was clear that the larger forces or greater the time between the pulses of the stokeslets, the more chaos could be seen. This was apparent from indicators on the Poincaré sections, such as hyperbolic or elliptic points determining how the particles were stretching or rotating. Eventually, for optimum values of the system, global chaos could be seen. These measures were explored for both horizontally and vertically displaced stokeslets, and the results compared using the Hénon index. The results showed the limiting value of $\alpha = 4.4$ as the bifurcation value above which we have chaotic mixing of the flow for any θ in the vertically displaced stokeslet case. For horizontally displaced stokeslets, we considered three different implicit maps and so found three values for the bifurcation value of α. The midpoint map produces the highest value while the map implicit in the z-direction (r and z being the usual polar coordinate directions) has the lowest and closest value of α to the vertically displaced stokeslet case. Dispersion of a group of particles was then examined and analysed using statistical methods. This gave an indication of the type of particle movement we would see if we had standard diffusion within the system. The addition of white noise has lead to realistic results showing how certain systems produce more or less mixing than we would expect without the affect of the flagellum. When θ was large, so that the results were comparable with experimental data, the addition of white noise (for large enough values of α) lead to superdiffusion indicating the promotion of mixing to a greater extent than when diffusion alone is present.

By introducing previous studies investigating the motion of both flagella and cilia, we build a platform from which to progress onto developing the fully three-dimensional model. First, presenting an extension to the planar study, the attracting properties of the

plane within which the stokeslets are situated is addressed. This confirms the results we have presented in Chapter 3, especially for the horizontally displaced stokeslets. Gleaning information on the flow fields around the two stokeslets we observe toroidal flow fields created around each stokeslet. This creates interesting interactions between the stokeslets dependent on their proximity to each other, due to the coalescing of their associated stream lines.

In the full three-dimensional model, we now introduce Green's functions and follow the method of Higdon (1979*a*) to satisfy of the boundary conditions around a three-dimensional representation of a typical sessile choanoflagellate. Representing the cell body as a sphere, the substrate of attachment as a plane and the flagellum as a slender body, we neglect the collar in our simple model to begin to generate a representation of particle paths around SA. By distributing singularities in the form of stokeslets and dipoles along the flagellum, an accurate configuration of the forces created due to a helical beat is found. Image systems within both the sphere and the plane allow one to build up a full picture of the force interactions which are affecting the flow field around SA leading to the numerical generation of particle paths. Using experimental data to give dimensions for 'realistic' organisms, the numerical particle paths generated show good agreement with experimental results, specifically with the studies of Pettitt (2000). By considering the length and time scale differences between the numerics and the experimental results, one can non-dimensionalise both problems allowing a fair comparison.

6.2 Further development

There are several areas where further development of this work could be undertaken.

The initial axisymmetric model could exploit a variety of other methods to give results about the degree of mixing and stirring of particles. The extent to which chaotic and statistical methods have been used within this thesis have by no means been exhausted. From this basis, investigations into capture and retention of tracers could be pursued to

enhance the information provided on feeding patterns by experimental data. Investigation of transport barriers as in Tang & Boozer (1996) would allow one to consider how particles diffuse within the system, giving another method to improve particle dispersion. These types of barriers to diffusion are discussed in Otto et al. (2001).

The three-dimensional model of SA has provided valuable results concerning particle paths, but the addition of a collar would enhance the model further. Modelling each of the tentacles composing the collar as a slender cylinder, an appropriate distribution of singularities and image systems could satisfy the boundary conditions across the collar. Such a model would enable the flux and flow patterns through and around the collar to be investigated. This would allow comparison with experimental results as well as giving a greater insight into particle motion.

Finally, investigating other areas where we may apply the model will give our study more breadth. There may be different biological systems which can be modelled by similar theories to those presented. The techniques used in the model involving blinking stokeslets is applicable to motion which is of a pulsatile nature. Yannacopoulos et al. (2001) have investigated peristaltic motion within the gut following their previous two-dimensional work with blinking stokeslets, see Otto et al. (2001). Similarly, the interaction between a number of SA (or similar organisms) could create an extension such that one could model the influence of a colony of organisms on particles within the flow.

Appendix A

FOURIER TRANSFORMS IN THREE DIMENSIONS

By taking Fourier transforms of the equations given in Aderogba & Blake (1978*a*) and repeated here as

$$\nabla p = \mu \nabla^2 \mathbf{u} + \mathbf{F}\delta(\mathbf{x} - \mathbf{y}) \quad \text{and} \quad \nabla.\mathbf{u} = 0 \tag{A.1}$$

we can gain the solution which defines the velocity and the pressure of the fluid due to the stokeslet as on page 24. A stokeslet is a singularity of the Stokes flow equations and here we regard it as a point force. The work by Blake (1971) is used as a basis for this appendix. Blake (1971) described the force and its image system using diagrams. He describes how the stokeslets are positioned, their direction and the effect they have on the near and far field.

First, we define the Green's function, $\mathbf{f}$, as the solution to (A.1) in the form

$$u_i(\mathbf{x}) = \mathrm{f}_{ij}(\mathbf{x}, \mathbf{y}) \frac{F_j}{8\pi\mu}.$$

If we write equation (A.1) in summation notation using partial derivatives as

$$\frac{\partial p}{\partial x_j} = \mu \frac{\partial^2 u_j}{\partial x_k^2} + F_j \delta(\mathbf{x} - \mathbf{y}) \quad \text{and} \quad \frac{\partial u_j}{\partial x_j} = 0,$$

then we can take Fourier transforms as a method of deriving the solution.

After taking Fourier transforms of equations (A.1), we find

$$\tilde{f}_{ij} = \frac{4}{(2\pi)^{\frac{3}{2}}k^2}\left(\delta_{ij} - \frac{k_i k_j}{k^2}\right) \quad \text{and} \quad \tilde{p}_j = -\frac{4ik_j}{(2\pi)^{\frac{1}{2}}k^2}. \tag{A.2}$$

The tilde above a function indicates the Fourier transform has been taken while $k^2 = k_j k_j$, where k is the variable due to performing the Fourier transform. As we can see from (A.2), to solve these expressions we need to know the inverse three-dimensional Fourier transform. The Fourier transform and its inverse are given by

$$g(\mathbf{x}) = \frac{1}{(2\pi)^{\frac{3}{2}}}\int_{\text{space}} \tilde{g}(\mathbf{k})e^{\mathrm{i}\mathbf{k}.\mathbf{x}}\,\mathrm{d}\mathbf{k} \quad \text{and} \quad \tilde{g}(\mathbf{k}) = \frac{1}{(2\pi)^{\frac{3}{2}}}\int_{\text{space}} g(\mathbf{x})e^{-\mathrm{i}\mathbf{k}.\mathbf{x}}\,\mathrm{d}\mathbf{x},$$

where $\mathbf{k}.\mathbf{x}$ is defined as the usual scalar product, Pozrikidis (1991).

Once we know p from equation (A.2) we can also find the solution for $\mathbf{u}$. There are a couple of formulae which are helpful in performing the transform which are not obvious and are given by

$$\int \frac{e^{\mathrm{i}\mathbf{k}.\mathbf{x}}}{k^2}\,\mathrm{d}\mathbf{k} = \int \frac{\mathrm{i}k_l x_l}{k^2}\,\mathrm{d}k_j = \frac{\pi^2}{x^2} \quad \text{and} \quad \int \frac{e^{\mathrm{i}\mathbf{k}.\mathbf{x}}}{k^4}\,\mathrm{d}\mathbf{k} = \int \frac{\mathrm{i}k_l x_l}{k^4}\,\mathrm{d}k_j = \pi^2\mathbf{x},$$

where $x = |\mathbf{x}|$. Both of these formula are given by Ladyzheskaya (1969) and Pozrikidis (1991).

Solving (A.2) by taking inverse Fourier transforms, we have expressions for p and $\mathbf{u}$ given by

$$u_i = \frac{F_j}{8\pi\mu}\left(\frac{\delta_{ij}}{x} + \frac{x_i x_j}{x^3}\right) \quad \text{and} \quad p = \frac{F_j x_j}{4\pi x^3}.$$

The velocity is given by $\mathbf{u}$ and from this we can now use stream functions to determine where particles in the flow are advected to under the influence of the point force.

Appendix B

THE JACOBIAN OF THE MAP

To calculate the Jacobian for the midpoint map we need to find the corresponding elements of the matrix which is given by

$$\mathbf{J} = \begin{pmatrix} \dfrac{\partial \eta_{n+1}}{\partial \eta_n} & \dfrac{\partial \eta_{n+1}}{\partial z_n} \\ \dfrac{\partial z_{n+1}}{\partial \eta_n} & \dfrac{\partial z_{n+1}}{\partial z_n} \end{pmatrix}.$$

For the midpoint map there are two equations which we differentiate to give the elements of the matrix. These are the $(n+1)^{\text{st}}$ position of the particle and are given as

$$\eta_{n+1} = \eta_n + \frac{\partial \psi}{\partial z}(\eta_m, z_m) \quad \text{and} \quad z_{n+1} = z_n - \frac{\partial \psi}{\partial \eta}(\eta_m, z_m), \tag{B.1}$$

where the derivatives of ψ are determined at the mid points $(\eta_m, z_m) = \left(\dfrac{\eta_n + \eta_{n+1}}{2}, \dfrac{z_n + z_{n+1}}{2} \right)$.

The matrix above shows that we need to differentiate the coordinates of the location of the particle (given in equation (B.1)) with respect to both η_n and z_n. Hence, an intermediate step to calculating the final Jacobian we will require the terms

$$\frac{\partial \eta_m}{\partial \eta_n} = \frac{1}{2}\left(1 + \frac{\partial \eta_{n+1}}{\partial \eta_n}\right) \quad , \quad \frac{\partial z_m}{\partial \eta_n} = \frac{1}{2}\frac{\partial z_{n+1}}{\partial \eta_n}, \tag{B.2}$$

$$\frac{\partial \eta_m}{\partial z_n} = \frac{1}{2}\frac{\partial \eta_{n+1}}{\partial z_n} \quad \text{and} \quad \frac{\partial z_m}{\partial z_n} = \frac{1}{2}\left(1 + \frac{\partial z_{n+1}}{\partial z_n}\right). \tag{B.3}$$

We proceed with differentiating both terms in equation (B.1) to find each of the terms

in the Jacobian. The differentiation of the η_{n+1} term first gives:

$$\frac{\partial \eta_{n+1}}{\partial \eta_n} = \frac{1 + \frac{1}{2}\psi_{\eta z} + \frac{1}{2}\psi_{zz}\frac{\partial z_{n+1}}{\partial \eta_n}}{1 - \frac{1}{2}\psi_{\eta z}} \quad \text{and} \quad \frac{\partial \eta_{n+1}}{\partial z_n} = \frac{\frac{1}{2}\psi_{zz}\left(1 + \frac{\partial z_{n+1}}{\partial z_n}\right)}{1 - \frac{1}{2}\psi_{\eta z}}, \tag{B.4}$$

whilst the z_{n+1} term give

$$\frac{\partial z_{n+1}}{\partial \eta_n} = -\frac{\frac{1}{2}\psi_{\eta\eta}\left(1 + \frac{\partial \eta_{n+1}}{\partial \eta_n}\right)}{1 + \frac{1}{2}\psi_{\eta z}} \quad \text{and} \quad \frac{\partial z_{n+1}}{\partial z_n} = \frac{1 - \frac{1}{2}\psi_{\eta z} - \frac{1}{2}\psi_{\eta\eta}\frac{\partial \eta_{n+1}}{\partial z_n}}{1 + \frac{1}{2}\psi_{\eta z}}. \tag{B.5}$$

All of these terms are dependent on the derivatives of the midpoints given above in equation (B.1) and by substituting these in during the intermediate stages we have obtained the equations (B.4) and (B.5).

Eliminating terms between the equations, we can arrive at the four terms needed to explicitly define the Jacobian in terms of the derivatives. Initially, eliminating $\frac{\partial \eta_{n+1}}{\partial z_n}$ from equation (B.5 b) using equation (B.4 b), we can determine both the terms from the second column of $\mathbf{J}$. Similarly, eliminating $\frac{\partial z_{n+1}}{\partial \eta_n}$ from (B.4 a) using equation (B.5 a), we obtain both the terms in the first column of $\mathbf{J}$. Hence, assembling the Jacobian in its entirety we have

$$\mathbf{J} = \begin{pmatrix} \frac{4(1 + \psi_{\eta z}) + \Phi}{4 - \Phi} & \frac{4\psi_{zz}}{4 - \Phi} \\ -\frac{4\psi_{\eta\eta}}{4 - \Phi} & \frac{4(1 - \psi_{\eta z}) + \Phi}{4 - \Phi} \end{pmatrix},$$

where we have defined $\Phi = \psi_{\eta z}^2 - \psi_{\eta\eta}\psi_{zz}$. All the terms are evaluated at the midpoint given by (η_m, z_m).

Appendix C

A CONTINUOUS FORCE DISTRIBUTION ALONG A FLAGELLUM; THE GRAY & HANCOCK METHOD

The Gray & Hancock method studies flagellar propulsion through a fluid and concentrates on determining the forces exerted by small elements of the flagellum. Dividing the flagellum into elements over which forces can be determined is a method employed in many studies of flagella mechanics. The theory is based on the undulating motion of the flagellum which develops the thrust to propel an organism forward (balancing the drag). The organism on which the theory was initially based was the spermatozoa of a sea urchin. This organisms movement was chosen as it had undulatory characteristics occurring in each cycle of movement. By looking at such an organism one can generalise the results over one complete wave length.

The type of wave form considered will be important, especially because it is not uniform along the whole flagellum length in many biological entities. Gray & Hancock regarded there to be a centre-line along which the wave acted, and this enabled them to set up a coordinate grid to describe how all the elements of the flagellum were interacting with one another. These elements of the flagellum are sections of small length, δs, allowing them to generalise the theory they introduce.

The results of Gray & Hancock theory are used to relate the speed of the organism to

the form and speed of the actual wave. Obviously, in their investigation of spermatozoa, they considered how an organism propelled itself to swim through a fluid. The sessile choanoflagellate, SA, is a fixed organism and so the propulsion created is not important to the same degree. However, the similarities in the theory to model the flow created by the beating flagellum can still be used. The wave type which was introduced was sinusoidal but this can still be used to allow us to gain a good interpretation of the force interaction.

As Figure C.1 shows, the theory is interested in the normal and the tangential forces, δN and δL, created by the flagellum and their effect on the fluid. The normal component has a propulsive force if orientated towards the translation axis of the whole cell. As well as the propulsive force, there is also the tangential drag force which the elements of the flagellum will experience.

A small element of the tail, δs, has several forces acting on it and these forces will depend on where the element is situated relative to the other elements of the flagellum. This is due to the force created varying as a function of φ, where φ is defined as the angle of orientation of a small element of the tail from the axis of propulsion. By using the axis defined as **0x** and **0y** (see Figure C.1), Gray & Hancock describe the elements of both the transverse and propulsive velocity in terms of the normal and tangential directions. As a variable, φ will be dependent on the form of the wave and in particular, its amplitude and wavelength. The two major components of forces that act on the tail arise from the motion of the tail. We know the flagellum moves in a transverse (side-to-side) motion as well as in the actual direction of motion in motile organisms. We should note that in the sessile case, although the organism cannot actually move perpendicular to the boundary of attachment, we will still see the wave form moving in this sense, i.e. away from the fixed body. This is because the flagellum propagates the wave in this direction. By considering the components of these forces in the tangential and normal directions to the surface of the cell body, Gray & Hancock found forces which retard or propel the flagellum when it is motile. In an analogy to the sessile case, such forces would push the fluid away from

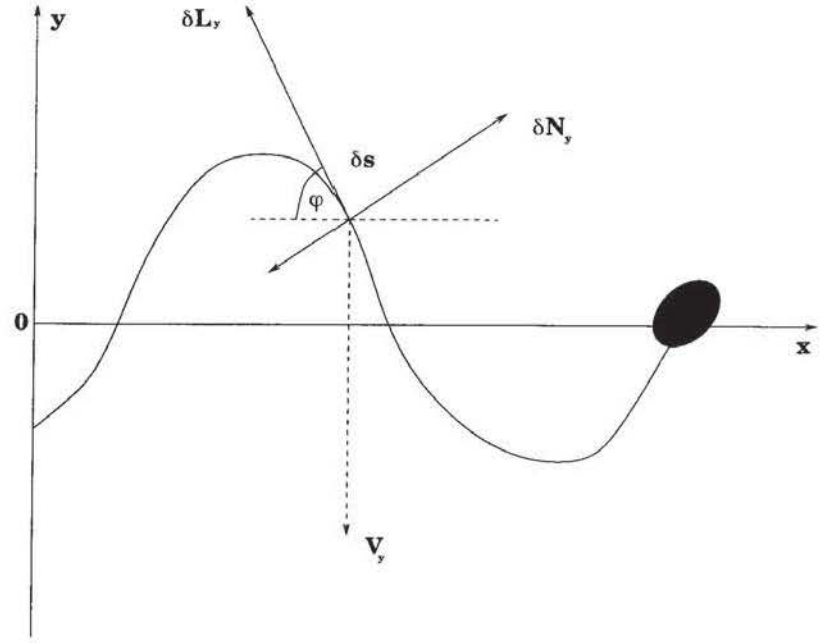

Fig. C.1 (a) Forces due to displacement along the **Oy** axis.

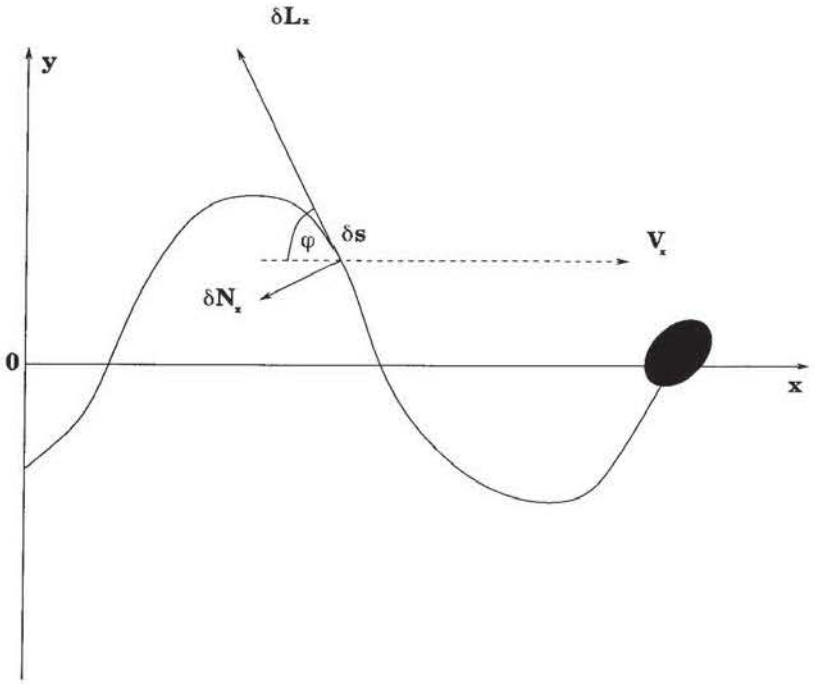

Fig. C.1 (b) Forces due to displacement along the **Ox** axis.

Figure C.1: A diagram to show the forces on a swimming spermatozoon.

the boundary in the sessile case.

Referring to Figure C.1. we see the transverse velocity, V_y, occurs as the wave passes and the propulsive velocity, V_x, occurs in the direction of motion. To calculate the actual thrust and drag components which act on the body one needs to consider the forces these velocities place on small elements of the tail. These can be calculated once the resistance coefficients for the organism under consideration are known. The resistance coefficients are C_N and C_T for the normal and tangential directions respectively. They indicate how much resistance the surface of the cell is going to provide to motion in the normal and tangential directions. There is some debate at present to what these coefficients should be as they are constantly being refined. An example of those given by Gray & Hancock are

$$C_N = \frac{4\pi\mu}{\ln(kr) - \frac{1}{2}} \quad \text{and} \quad C_T = \frac{2\pi\mu}{\ln(kr) - \frac{1}{2}}.$$

In these coefficients, μ represents the dynamic viscosity of the fluid, r represents the flagellum radius and $2\pi/k$ is the wave length of the beat. This method of resistance coefficients has been used with some success in predicting the forces created by certain organisms observed under experimental conditions. There are other recent methods which also show varying degrees of agreement with this method.

The resultant forward thrust, i.e. the force in the direction **Ox** that provides the propulsion, is determined by considering the elements of the translational and forward components of the velocities. We only have forward thrust when the resistance coefficient normal to the surface is greater than resistance tangential to the surface. This is a simple relation defined from deriving δF, a small element of the forward thrust.

By summing components of force due to both types of motion (translational and forward) one can determine the normal and tangential forces which act overall. By combining these to find the normal force it is possible to find the threshold value needed to overcome the tangential resistance to give a positive net propulsion.

Figure C.1 summarises the important components of the forces which act on the tail. The tangential velocity of the tail is V_y which has a component in the normal direction

to the tail, given by δN_y, and tangential to the body, given by δL_y. Similarly, the component of velocity which is in the direction of propulsion is V_x and provides normal and tangential components of the force to the body, which are given by δN_x and δL_x respectively. Notice that the normal forces act in opposing directions which need to be considered when summing over all the components to find the total force.

The force which acts in the direction of the normal is given by

$$\delta N = \delta N_y - \delta N_x,$$

and the force acting tangentially is

$$\delta L = \delta L_y - \delta L_x.$$

Hence the forward thrust is given by the component of the normal and tangential forces in the direction of propulsion, i.e. the **Ox** axis. If one defines the element of the thrust as δF then

$$\delta F = \delta N \sin\varphi - \delta L \cos\varphi.$$

Conditions on propulsion can be derived from this because we know the rearward drag component of the force must be less than the forward facing component to overcome the resistance to the motion of the cell. We can also see from the equation for the element of the total force, δF, that the magnitude of propulsion varies depending on which element we are considering. Therefore, at the apex of the bend where φ is zero, due to entirely tangential motion there will only be drag forces acting on the tail.

The types of wave form one uses to describe the flagellum beat can be varied because the general formula will consider different arguments. The total force, F, over one wave length is given as the integral of δF over the length of the wave, i.e.

$$F = \int_0^L \delta F \, \mathrm{d}s.$$

Consideration of an organism with no head is advantageous in our model because by having no external forces created by a rotating flagellum is more realistic to the flagellum model we choose to investigate. Hence, one does not have to consider balancing the force with the drag on the head. There are a number of types of wave which can be considered, such as the sine wave or a combination of a sine and exponential function. We can amend Gray & Hancock theory of a usual sine wave to take into account a wave of varying amplitudes. Usually this involves studying a steadily decreasing amplitude for increasing values of x, i.e. as we move further away from the cell body.

Appendix D

SINGULARITY EXPRESSIONS AS COMPONENTS OF THE IMAGE SYSTEMS

The image systems are composed of a complicated set of singularities which were stated in Higdon (1979*a*). The expression given in Oseen (1927) for the image system of a stokeslet is difficult to manipulate due to its dependence on the coordinate $\mathbf{y}$, but by considering an expansion of the expression about the origin for $A \ll |\mathbf{y}|$ one begins to find simpler expressions. Since we can find the images of the Stokes-doublet and dipole by differentiating the expression for the image of a stokeslet (by the rule stated in section 5.3.3), it is sensible to look for an easily differentiable form of the image system for the stokeslet, S^*_{jk}. Therefore, we need a simpler expression in terms of the differentiation variable, $\mathbf{y}$.

The expansion given in Higdon (1979*a*) for the image system of a stokeslet is composed of the first-order and the second-order terms of the expansion about the origin. These second-order terms are divided into symmetric and antisymmetric components which are denoted by the superscripts S and A respectively within this appendix. Denoting the first-order terms by W and the second order symmetric and antisymmetric terms by W^S and W^A, we write the expansion for the image of the stokeslet as

$$S^*_{jk}(\mathbf{x},\mathbf{y}) = \left(\frac{\delta_{km}}{|\mathbf{y}|} + \frac{y_k y_m}{|\mathbf{y}|^3}\right) W_{jm}(\mathbf{x}) + \left(\frac{y_k y_m y_n}{|\mathbf{y}|^5}\right) W^S_{jmn}(\mathbf{x}) + \left(\frac{y_m}{|\mathbf{y}|^3}\right) W^A_{jkm}(\mathbf{x}), \quad \text{(D.1)}$$

where

$$W_{jk}(\mathbf{x}) = -\frac{3}{4}A\left(\frac{\delta_{jk}}{|\mathbf{x}|} + \frac{x_j x_k}{|\mathbf{x}|^3}\right) + \frac{1}{4}A^3\left(-\frac{\delta_{jk}}{|\mathbf{x}|^3} + \frac{3x_j x_k}{|\mathbf{x}|^5}\right),$$

$$W^S_{jkl}(\mathbf{x}) = -\frac{5}{2}A^3\left(-\frac{x_j\delta_{kl}}{|\mathbf{x}|^3} + \frac{3x_j x_k x_l}{|\mathbf{x}|^5}\right) + \frac{3}{2}A^5\left(-\frac{x_j\delta_{kl} + x_k\delta_{jl} + x_l\delta_{jk}}{|\mathbf{x}|^5} + \frac{5x_j x_k x_l}{|\mathbf{x}|^7}\right),$$

and

$$W^A_{jkl}(\mathbf{x}) = A^3\left(\frac{-\delta_{jk}x_l + \delta_{jl}x_k}{|\mathbf{x}|^3}\right).$$

We can differentiate equation (D.1) to obtain the images of the higher order singularities. Because a Stokes-doublet can be derived from differentiating the stokeslet with respect to y_l, then the image of a Stokes-doublet is derived from differentiating equation (D.1) with respect to y_l. This gives

$$\begin{aligned} S^{D*}_{jk}(\mathbf{x},\mathbf{y}) = &-\left[\left(-\frac{y_m\delta_{kl}}{|\mathbf{y}|^3} + \frac{3y_k y_l y_m}{|\mathbf{y}|^5}\right) + \left(\frac{y_l\delta_{km} - y_k\delta_{lm}}{|\mathbf{y}|^3}\right)\right] W_{jm}(\mathbf{x}) \\ &- \left[-\frac{\delta_{kl}y_m y_n + \delta_{lm}y_k y_n + \delta_{ln}y_k y_m}{|\mathbf{y}|^5} + \frac{5y_k y_l y_m y_n}{|\mathbf{y}|^7}\right] W^S_{jmn}(\mathbf{x}) \\ &- \left[\frac{\delta_{lm}}{|\mathbf{y}|^3} + \frac{3y_l y_m}{|\mathbf{y}|^5}\right] W^A_{jkm}(\mathbf{x}). \end{aligned} \tag{D.2}$$

Similarly, the image system for the dipole is found by differentiating once again the image system for the stokeslet (as described in section 5.3.3), to give

$$\begin{aligned} D^*_{jk}(\mathbf{x},\mathbf{y}) = &\left[-\frac{\delta_{km}}{|\mathbf{y}|^3} + \frac{3y_k y_m}{|\mathbf{y}|^5}\right] W_{jm}(\mathbf{x}) \\ &+ \left[-\frac{\delta_{km}y_n + \delta_{kn}y_m + \delta_{mn}y_k}{|\mathbf{y}|^5} + \frac{5y_k y_m y_n}{|\mathbf{y}|^7}\right] W^S_{jmn}(\mathbf{x}). \end{aligned} \tag{D.3}$$

Equations (D.1), (D.2) and (D.3) explicitly give the sphere images needed throughout the problem and referred to in section 5.3.3.

Appendix E

SINGULARITY EXPRESSIONS FROM THE COMBINED IMAGE SYSTEM

The combined image system will consist of a number of previously defined expressions which include the image system for the plane ($\check{S}_{jk}$) and the image system which is developed from the image of the plane in the sphere ($\check{S}^*_{jk}$). Both these expressions are now explicitly stated below in equations (E.1) and (E.2) respectively.

The image system for the plane is constructed from a stokeslet, a Stokes-doublet and a dipole, all considered at the image point in the plane, $\check{\mathbf{y}}$, defined in equation (5.9). The total image system for the plane is given by

$$\check{S}_{jk} = -S_{jk}(\mathbf{x}, \check{\mathbf{y}}) + 2h(\mathbf{y})p_l[\delta_{km} - p_k p_m]S^D_{jlm}(\mathbf{x}, \check{\mathbf{y}}) - 2h^2(\mathbf{y})[\delta_{km} - p_k p_m]D_{jm}(\mathbf{x}, \check{\mathbf{y}}). \quad \text{(E.1)}$$

Finally, the most complicated expression which we need to state is for the sphere images of the plane image system, the latter given as $\check{S}_{jk}$ in equation (E.1). We are required to use this in equation (5.11) as a constituent of the first approximation to the Green's function for the whole system. We need to consider evaluation of the stokeslet, Stokes doublet and dipole terms within the plane image system at the image point, $\check{\mathbf{y}}$. Hence, we take the image system for the plane ($\check{S}_{jk}$), and evaluate it at the image point

in the sphere. We define the sphere image of the plane image system as

$$\check{S}^{*}_{jk} = -S^{*}_{jk}(\mathbf{x}, \check{\mathbf{y}}) + 2h(\check{\mathbf{y}})p_l[\delta_{km} - p_k p_m]S^{D*}_{jlm}(\mathbf{x}, \check{\mathbf{y}}) - 2h^2(\mathbf{y})[\delta_{km} - p_k p_m]D^{*}_{jm}(\mathbf{x}, \check{\mathbf{y}}), \quad \text{(E.2)}$$

which contains the same terms as equation (E.1), i.e. the stokeslet, Stokes-doublet and dipole respectively, all evaluated at the image point in the sphere (denoted by *).

Appendix F

MATRIX INVERSION TO DETERMINE THE FLAGELLAR FORCES

To establish the matrix for inversion requires the summation of terms from expression (5.26). We can think of equation (5.25) re-interpreted in terms of expression (5.26) to give the equation

$$u_j(\mathbf{X}(s_q^m)) = \sum_{n=1}^{N} \left\{ Q_{jk}(s_q^m, s_n) f_k(s_n) \right\},$$

for each of $q = 1, ..., N$. If we define the matrix $\mathbf{Q} = \sum_{n=1}^{N} Q_{jk}(s_q^m, s_n)$, this is the matrix we are required to invert to solve for $\mathbf{f}$.

The structure of each of the vectors or matrices we require is presented within the subsequent paragraphs. The vector $\mathbf{f}$ is a $3N \times 1$ vector constructed from N vectors, each with size 3×1 and taking the form

$$\begin{pmatrix} f_1(s_q^m) \\ f_2(s_q^m) \\ f_3(s_q^m) \end{pmatrix},$$

for each segment with midpoint s_q^m $(q = 1, ..., N)$. The vector $\mathbf{u}$ is also a $3N \times 1$ vector

which is constructed from N vectors which can be represented similarly to above by

$$\begin{pmatrix} u_1(s_q^m) \\ u_2(s_q^m) \\ u_3(s_q^m) \end{pmatrix},$$

for each midpoint s_q^m, as previously defined.

We can also explicitly define the matrix $\mathbf{Q}$ which has dimensions $3N \times 3N$ as

$$\mathbf{Q} = \begin{pmatrix} ..... & & \\ Q_{jk}(s_{q-1}^m, s_1) & ..... & ..... \\ Q_{jk}(s_q^m, s_1) & ..... & Q_{jk}(s_q^m, s_N) \\ Q_{jk}(s_{q+1}^m, s_1) & ..... & ..... \\ ..... & & \end{pmatrix}.$$

Notice that the dimensions are correct because each of the terms $Q_{jk}(s_q^m, s_r)$ is itself a 3×3 matrix due to the subscript notation of $j, k = 1, 2$ and 3, where as before $q, r = 1, ..., N$.

As a check to confirm the validity of this method, we can look at a simpler breakdown by examining the calculation of the velocity given by $\mathbf{u}(s_q^m)$. The matrix equation for this term is given by

$$\mathbf{u}(s_q^m) = \begin{pmatrix} u_1(s_q^m) \\ u_2(s_q^m) \\ u_3(s_q^m) \end{pmatrix} = \mathbf{Q}(s_q^m)\,\mathbf{f}(s),$$

where we notice that the value of $\mathbf{f}$ will only be dependent on its position along the flagellum and not the midpoint of the q^{th} segment, from which the other terms take their

values. Proceeding in longhand with the matrix multiplication we have

$$\begin{pmatrix} u_1(s_q^m) \\ u_2(s_q^m) \\ u_3(s_q^m) \end{pmatrix} = \begin{pmatrix} Q_{1k}(s_{q-1}^m, s_1) & ..... & ..... \\ Q_{2k}(s_q^m, s_1) & ..... & Q_{2k}(s_q^m, s_N) \\ Q_{3k}(s_{q+1}^m, s_1) & ... & ..... \end{pmatrix} \begin{pmatrix} f_k(s_1) \\ f_k(s_2) \\ ..... \\ ..... \\ f_k(s_N) \end{pmatrix}.$$

The multiplication of the matrices on the right hand side gives a 3×1 array which conforms to the dimension conventions we have seen in equation (5.25). Writing the multiplication out in full gives expressions for each term as

$$\begin{pmatrix} u_1(s_q^m) \\ u_2(s_q^m) \\ u_3(s_q^m) \end{pmatrix} = \begin{pmatrix} ..... \\ Q_{2k}(s_q^m, s_1)f_k(s_1) + Q_{2k}(s_q^m, s_2)f_k(s_2) + ... + Q_{2k}(s_q^m, s_N)f_k(s_N) \\ ..... \end{pmatrix}.$$

Each term within each row has indices which can be summed over n (for $n = 1, ..., N$) allowing one to write the vector for $\mathbf{u}(s_q^m)$ as

$$\begin{pmatrix} u_1(s_q^m) \\ u_2(s_q^m) \\ u_3(s_q^m) \end{pmatrix} = \begin{pmatrix} ..... \\ \sum_{n=1}^{N} Q_{2k}(s_q^m, s_n)f_k(s_n) \\ ..... \end{pmatrix},$$

which is the same as the terms found in (5.25). Since the terms for each s_q^m (with $q = 1, ..., N$) within matrix $\mathbf{Q}$ will multiply with a corresponding term within the vector $\mathbf{f}$, then we merely need to set up the numerical computation such that one defines a square

matrix to be inverted. Therefore, we can finally write

$$\begin{pmatrix} \mathbf{u}(s_1) \\ \mathbf{u}(s_2) \\ \dots \\ \dots \\ \mathbf{u}(s_N) \end{pmatrix} = \begin{pmatrix} \mathbf{Q}(s_1) \\ \mathbf{Q}(s_2) \\ \dots \\ \dots \\ \mathbf{Q}(s_N) \end{pmatrix} \begin{pmatrix} f_k(s_1) \\ f_k(s_2) \\ \dots \\ \dots \\ f_k(s_N) \end{pmatrix},$$

where the first matrix on the right hand side is the $3N \times 3N$ square matrix we are required to invert to find $\mathbf{f}$.

References

Aderogba, K. & Blake, J. R. (1978*a*), 'Action of a force near the planar surface between two semi-infinite immiscible liquids at very low Reynolds numbers', *Bull. Aust. Math. Soc.* **18**, 345–356.

Aderogba, K. & Blake, J. R. (1978*b*), 'Addendum to: Action of a force near the planar surface between two semi-infinite immiscible liquids at very low Reynolds numbers', *Bull. Aust. Math. Soc.* **19**, 309–318.

Aref, H. (1984), 'Stirring by chaotic advection', *J. Fluid Mech.* **143**, 1–21.

Aref, H. & Balachandar, S. (1986), 'Chaotic advection in a Stokes flow', *Phys. Fluids* **29**, 3515–3521.

Berg, H. C. & Purcell, E. M. (1977), 'Physics of chemoreception', *Biophysical Journal* **20**, 193–219.

Blake, J. R. (1971), 'A note on the image system for a stokeslet in a no-slip boundary', *Proc. Camb. Phil. Soc.* **70**, 303–310.

Blake, J. R. (2001), Fluid mechanics of ciliary propulsion, *in* 'Computational Modeling in Biological Fluid Dynamics', Proceedings of IMA 1999.

Blake, J. R. & Otto, S. R. (1996), 'Ciliary propulsion, chaotic filtration and a 'blinking' stokeslet', *Journal of Engineering Mathematics* **30**, 151–168.

Blake, J. R., Otto, S. R. & Blake, D. A. (1998), 'Filter feeding, chaotic filtration, and a blinking stokeslet', *Theoret. Comput. Fluid Dynamics* **10**, 23–36.

Brennen, C. & Winet, H. (1977), 'Fluid mechanics of propulsion by cilia and flagella', *Ann. Rev. Fluid Mech.* **9**, 339–398.

Cartwright, J. H. E., Feingold, M. & Piro, O. (1996), 'Chaotic advection in three-dimensional unsteady incompressible laminar flow', *J. Fluid Mech.* **316**, 259–284.

Eckhardt, B. & Yao, D. (1993), 'Local Lyapunov exponents in chaotic systems', *Physica D* **65**, 100–108.

Fenchel, T. (1986), 'Protozoan filter feeding', *Progress in Protistology* **1**, 65–113.

Fulford, G. R. & Blake, J. R. (1995), Hydrodynamics of filter feeding, *in* C. P. Ellington & T. J. Pedley, eds, 'Biological Fluid Dynamics', Society for Experimental Biology, pp. 183–197.

Gray, J. & Hancock, G. J. (1955), 'The propulsion of sea-urchin spermatozoa', *J. Exp. Biol.* **32**, 803–814.

Guckenheimer, J. & Holmes, P. (1983), *Nonlinear Oscillations, Dynamical Systems and Bifurcations of Vector Fields*, Springer-Verlag.

Hancock, G. J. (1953), 'The self propulsion of microorganisms through liquids', *Proc. Roy. Soc. A* **217**, 96 121.

Hénon, M. (1969), 'Numerical study of quadratic area-preserving mappings', *Quarterly of Applied Mathematics* **27**, 291–312.

Higdon, J. J. L. (1979*a*), 'The generation of feeding currents by flagellar motions', *J. Fluid Mech* **94**, 305–330.

Higdon, J. J. L. (1979*b*), 'A hydrodynamic analysis of flagellar propulsion', *J. Fluid Mech* **90**, 685–711.

Higdon, J. J. L. (1979*c*), 'The hydrodynamics of flagellar propulsion: helical waves', *J. Fluid Mech* **94**, 331–351.

Johnson, R. E. (1980), 'An improved slender-body theory for Stokes flows', *J. Fluid Mech* **99**, 411–431.

Ladyzheskaya, O. A. (1969), *The Mathematical Theory of Viscous Incompressible Flow*, Gordon and Breach Science Publishers.

Lichtenberg, A. J. & Lieberman, M. A. (1983), *Regular and Stochastic Motion*, Springer-Verlag.

Lighthill, J. (1976), 'Flagellar hydrodynamics', *SIAM Review* **18**, 161–230.

Lighthill, J. (1996), 'Helical distributions of stokeslets', *Journal of Engineering Mathematics* **30**, 35–78.

Liron, N. & Blake, J. R. (1981), 'Existence of viscous eddies near boundaries', *J. Fluid Mech.* **75**, 593–607.

Orme, B. A. A., Otto, S. R. & Blake, J. R. (2001*a*), 'Chaos and mixing in biological fluid dynamics: Blinking Stokeslets', *Mathematical Methods in the Applied Sciences.* In press.

Orme, B. A. A., Otto, S. R. & Blake, J. R. (2001*b*), 'Enhanced efficiency of feeding and mixing due to chaotic flow patterns around choanoflagellates', *J. Math Applied in Medicine and Biology.* In press.

Orme, B. A. A., Otto, S. R. & Blake, J. R. (2001*c*), 'Helical beat patterns around choanoflagellates', *Proc. Roy. Soc. A.* In preparation.

Oseen, C. W. (1927), *Neuere Methoden und Ergbnisse in der Hydrodynamik*, Leipzig: Akad.-Verlag.

Ottino, J. M. (1989), *The kinematics of mixing: stretching, chaos and transport*, CUP.

Otto, S. R., Yannacopoulos, A. N. & Blake, J. R. (2001), 'Transport and mixing in Stokes flow: the effect of chaotic dynamics on the blinking stokeslet', *J. Fluid Mech.* **430**, 1–26.

Pettitt, M. (2000), Prey capture and ingestion in choanoflagellates, PhD, The University of Birmingham.

Pettitt, M., Orme, B. A. A., Leadbeater, B. & Blake, J. R. (2001), 'Experimental investigations and results of filter feeding in choanoflagellates'. In preparation.

Pozrikidis, C. (1991), *Boundary integral and singularuty methods for linearized viscous flow*, CUP.

Ramia, M., Tullock, D. L. & Phan-Thien, N. (1993), 'The role of hydrodynamic interaction in the locomotion of microorganisms', *Biophysical Journal* **65**, 755–778.

Rubenstein, D. I. & Koehl, M. A. R. (1977), 'The mechanisms of filter feeding : Some theoretical considerations', *The American Naturalist* **111**, 981–994.

Shimeta, J. & Jumars, P. A. (1991), 'Physical mechanisms and rates of particle capture by suspension feeders', *Oceanogr. Mar. Biol. Annu. Rev.* **29**, 191–257.

Sleigh, M. A. (1973), *The Biology of Protozoa*, Edward Arnold.

Sleigh, M. A. (1991), 'Mechanisms of flagellar propulsion', *Protoplasma* **164**, 45–53.

Sleigh, M. A., ed. (1974), *Cilia and Flagella*, Academic Press.

Tang, X. Z. & Boozer, A. H. (1996), 'Finite time Lyapunov exponent and advection-diffusion equation', *Physica D* **95**, 283–305.

Taylor, G. I. (1951), 'Analysis of the swimming of microscopic organisms.', *Proc. Roy. Soc.* **A209**, 447–461.

Thomsen, H. A., Buck, K. R., Coale, S. L., Garrison, D. I. & Gowing, M. M. (1990), 'Loricate choanoflagellates (Acanthoecidae Choanoflagellida) from the Weddell Sea, Antarctica', *Zoologica Scripta* **19**, 367–387.

Yannacopoulos, A. N., Otto, S. R. & Blake, J. R. (2001), 'Effects of chaos in peristaltic flows.'. In preparation.